ABSTRACT

IMPORTANCE OF VEGETATION IN TSUNAMI MITIGATION: EVIDENCE FROM LARGE EDDY SIMULATIONS WITH FLUID-STRUCTURE INTERACTIONS

by
Abhishek Mukherjee

Communities worldwide are increasingly interested in nature-based solutions like coastal forests for the mitigation of coastal risks. Still, it remains unclear how much protective benefit vegetation provides, particularly in the limit of highly energetic flows after tsunami impact. The present thesis, using a three-dimensional incompressible computational fluid dynamics model with a fluid-structure interaction approach, aims to quantify how energy reflection and dissipation vary with different degrees of rigidity and vegetation density of a coastal forest.

In this study, tree trunks are represented as cylinders, and the elastic modulus of hardwood trees such as pine or oak is used to characterize the rigidity of these cylinders. To capture tsunami bore propagation in onshore, dam break flow is used over the wet surface in the numerical studies. After validating numerical code against experimental studies, multi-cylinder configurations are incorporated and Froude Number is used to scale the flow parameters and vegetation flow parameter (VFP) to scale the tree parameters such as elastic modulus, the diameter of the trunk, etc. Numerical tests are conducted for different cylinder diameters, densities, and elastic moduli.

The numerical results show that energy reflection increases with rigidity only for a single cylinder. In the presence of multiple cylinders, the difference in energy reflection created by varying rigidity diminishes as the number of cylinders increases. Instead of rigidity, the blockage area created by the presence of multiple tree trunks is found to dominate energy reflection.

As tree trunks are deformed by the hydrodynamic forces, they alter the flow field around them, causing turbulent kinetic energy generation in the wake region. As a consequence, trees dissipate flow energy, highlighting the importance of coastal forests in reducing the onshore energy flux of tsunamis by means of both reflection and dissipation.

IMPORTANCE OF VEGETATION IN TSUNAMI MITIGATION: EVIDENCE FROM LARGE EDDY SIMULATIONS WITH FLUID-STRUCTURE INTERACTIONS

by
Abhishek Mukherjee

A Dissertation
Submitted to the Faculty of
New Jersey Institute of Technology
in Partial Fulfillment of the Requirements for the Degree of
Doctor of Philosophy in Mechanical Engineering

Department of Mechanical and Industrial Engineering

May 2023

APPROVAL PAGE

IMPORTANCE OF VEGETATION IN TSUNAMI MITIGATION: EVIDENCE FROM LARGE EDDY SIMULATIONS WITH FLUID-STRUCTURE INTERACTIONS

Abhishek Mukherjee

Dr. Simone Marras, Dissertation Advisor — Date
Assistant Professor, Mechanical and Industrial Engineering, NJIT

Dr. Juan Carlos Cajas, Dissertation Co-Advisor — Date
Associate Professor, National Autonomous University of Mexico,
Mexico City, Mexico

Dr. Chao Zhu, Committee Member — Date
Professor, Mechanical and Industrial Engineering, NJIT

Dr. Samaneh Farokhirad, Committee Member — Date
Assistant Professor, Mechanical and Industrial Engineering, NJIT

Dr. Kyle Mandli, Committee Member — Date
Associate Professor, Applied Physics and Applied Mathematics,
Columbia University, New York City, USA

BIOGRAPHICAL SKETCH

Author: Abhishek Mukherjee

Degree: Doctor of Philosophy

Date: May 2023

Undergraduate and Graduate Education:

- Doctor of Philosophy in Mechanical Engineering,
  New Jersey Institute of Technology, 2023
- Master of Engineering in Mechanical Engineering,
  Jadavpur University, India, 2014
- Bachelor of Technology in Mechanical Engineering,
  Kalyani Govt. Engineering College, West Bengal, India, 2011

Major: Mechanical Engineering

Publications:

Flammang B., Marras S., Anderson E., Lehmkuhl O., Mukherjee A. *et al.*, "Remoras pick where they stick on blue whales," *Journal of Experimental Biology*, vol. 223(20), 2020.

Watanabe M., Arikawa T., Kihara N., Tsurudome C., Hosaka K., Kimura T., Hashimoto T., Ishihara F., Shikata T., Morikawa D. S., Makino T., Asai M., Chida Y., Ohnishi Y., Marras S., Mukherjee A. *et al.*, "Validation of tsunami numerical simulation models for an idealized coastal industrial site," *Coastal Engineering Journal*, vol. 64(20), 2022.

Mukherjee A., Cajas, J. C., Houzeaux G., Lehmkuhl O., Suckale J., Marras S., "Forest density is more effective than tree rigidity at reducing the onshore energy flux of tsunamis," *Coastal Engineering Journal*, vol. 182(104286), 2023.

Liu R., Daskiran C., Mukherjee A., Xin Q., Cui F., Marras S., Farooqi H., Dettman H., Boufadel M., "Characterization and modelling of water mixing energies and particle behavior during wave generation in CanmetENERGY Devon spill test tank," *Coastal Engineering Journal*, vol. 278(114237), 2023.

Presentations:

Mukherjee A., Cajas, J. C., Houzeaux G., Lehmkuhl O., Vazquez M., Suckale J., Marras S., "Using fluid-structure interaction to evaluate the energy dissipation of a tsunami run-up through idealized flexible trees," *Parallel Computational Fluid Dynamics*, France, 2020.

Mukherjee A., Cajas J. C., Houzeaux G., Lehmkuhl O., Marras S., Vazquez M., "A large eddy simulation study of the effect of flexible vegetation on the energy reduction of a tsunami during coastal inundation," *Society for Industrial and Applied Mathematics: Conference on Mathematical & Computational Issues in the Geosciences*, Italy, 2021.

Posters:

Mukherjee A. and Marras S., "First steps towards direct aeroacoustics via higher order spectral elements," *Poster Presentation, NJIT*, NJ, 2018.

Mukherjee A., Cajas J. C., Houzeaux G., Lehmkuhl O., Marras S., Vazquez M., "Tsunami wave interaction with rigid and flexible vegetation: A 3D large eddy simulation study," *American Geophysical Union Fall Meeting*, 2021.

I dedicate my dissertation work to my wife, son, parents, friends, and teachers

ACKNOWLEDGMENT

I would like to express my sincere gratitude and appreciation to my adviser, Dr. Simone Marras, for his continuous encouragement, support, motivation, and valuable contribution during my PhD research. He kept faith in me when I was struggling to work on my coding. He always motivated me and shared his stories from his PhD journey so that I would never feel let down during my struggling period. We spent a lot of time on how to improve my writing skills and manage time between different research projects. I am extremely grateful to have him as an advisor.

I would like to thank my coadvisor Dr. Juan Carlos Cajas, for his guidance in writing and research. He always guided me in finding the solution whenever I am stuck in my research. I also would like to thank Dr. Jenny Suckale because, without her continuous suggestions, guidance, support, and discussion, the research paper derived from the thesis work would not have been possible.

I am grateful to my dissertation committee members: Dr. Chao Zhu, Dr. Samaneh Farokhirad, and Dr. Kyle Mandli, for providing helpful suggestions.

I would like to thank my present and past colleagues in the Mechanical Engineering department: Dr. Jatin Kashyap, Dr. Subhajit Rakshit, Dr. Nikola Bosnjak, Dr. Suchandra Das, Dr. Vidushi Sharma, Allen Prasad Varghese, Keven Alkhoury, and Yassine Tissaoui for sharing their experiences and knowledge and discussing different research topics.

Finally, I would like to thank my parents Shovana and Bikash, and my sister Kankana for their valuable support and encouragement throughout my PhD. Special thanks to my lovely wife Souranjita because she is always supportive and encouraging during my hardest time in PhD. Without her sacrifice, my dream of becoming a successful researcher would not come true.

TABLE OF CONTENTS

TABLE OF CONTENTS
(Continued)

Chapter **Page**

LIST OF TABLES

Table **Page**

LIST OF FIGURES

Figure **Page**

LIST OF FIGURES
(Continued)

Figure **Page**

LIST OF FIGURES
(Continued)

Figure **Page**

CHAPTER 1

INTRODUCTION

1.1 Motivation

A tsunami is a catastrophic disaster in which a series of waves are formed due to earthquakes, volcanic eruptions, or landslides under the sea. The term "tsunami" originated in Japan, and it means "great wave in harbor" [41]. Tsunamis have caused massive damage to coastal areas, loss of lives, and shattered economies. One of the deadliest disasters in recent history, the 2004 boxing day Indian Ocean tsunami, triggered massive tsunami waves that reached up to 50 m in height [201], resulting in massive destruction to coastal areas, especially near the coasts of Somalia, and the coast of Indonesia. A study by Leone et al. [118] shows that Banda Aceh, a city located on the island of Sumatra, was completely destroyed, and several buildings were damaged from the shore to 2.7 km inland. Several tsunamis have occurred after this event; one of the major tsunami events after the Indian Ocean tsunami was the Tōhoku tsunami in Japan in 2011, where around 20,000 were killed [201]. In that incident, the multi-billion dollar concrete sea wall, which was built to protect the coastal region from tsunamis, was partially destroyed.

Clearly, tsunamis pose a considerable challenge to coastal communities. Scientists, therefore, attempt to mitigate or reduce tsunami threats in order to protect critical infrastructures and communities. The reason why we need to build an efficient coastal defense system is that tsunami waves, once generated, reach the shore quickly. Since tsunami waves travel at a speed proportional to the square root of the water depth when propagating on the open ocean, the speed of the wave is equivalent to the speed of a jet. For example, the 2004 Indian Ocean tsunami reached the coastal region within 2 hours of its generation [15]. Therefore, it is crucial to understand the

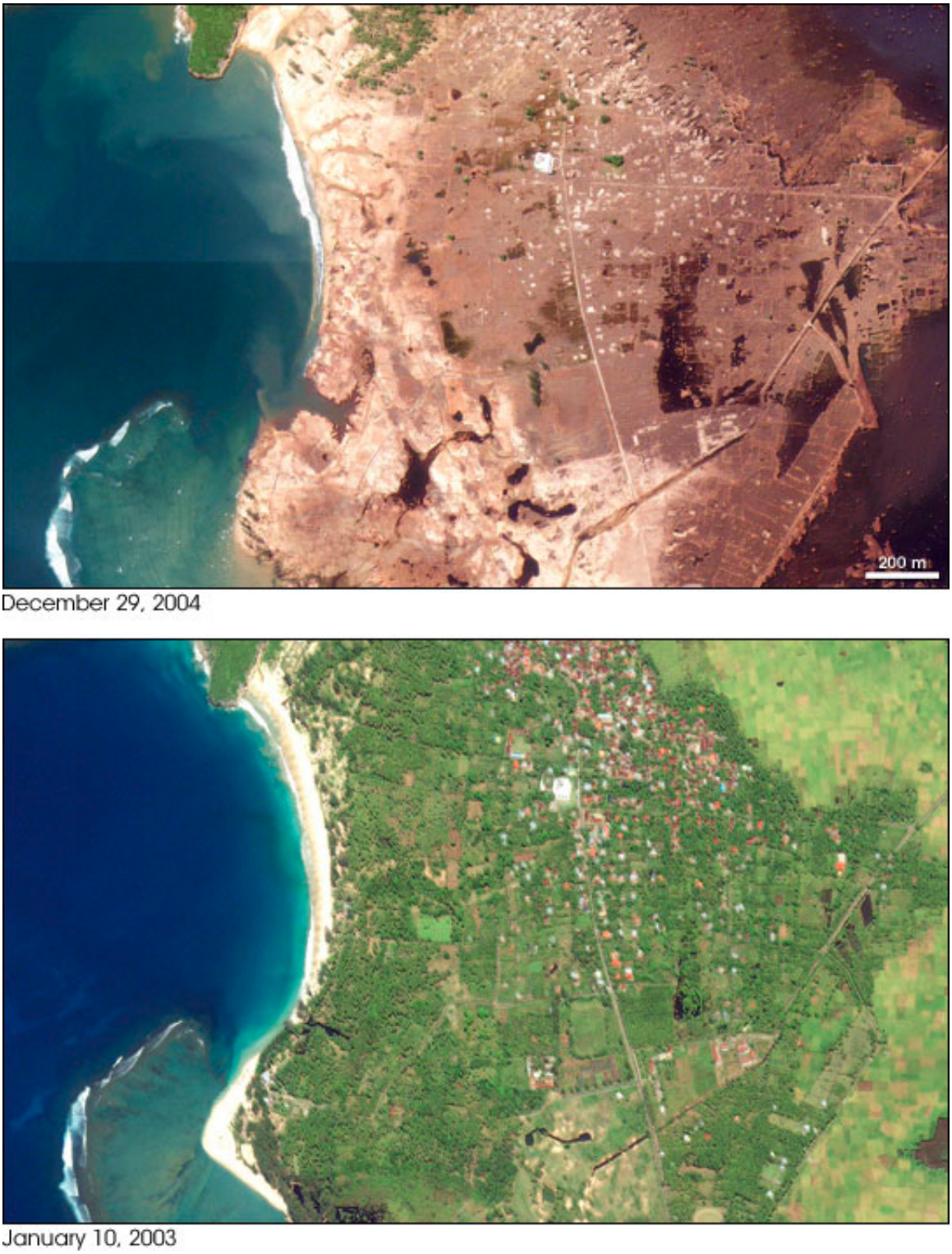

Figure 1.1 Satellite images of Lhoknga, Indonesia. Before (bottom) and after (top) the Indian Ocean tsunami.
Image is taken from *NASA [164].*

nature of tsunami waves in the onshore region and how these interact with onshore structures. A tsunami warning system (TWS) has been used and improved over the years to warn coastal communities about the tsunami impact once generated. TWS is used to gather real-time data from earthquake events and predict the damage and warn the coastal communities so that possible affected regions can be evacuated. For details on the tsunami warning system, please see different forecasting models developed by NOAA (National Oceanic and Atmospheric Administration) Center for Tsunami Research [e.g., 53, 57, 230]. Even if these forecasting models are proven efficient in the context of predicting tsunami impact on the onshore region, it is quite impossible to evacuate the whole coastal area within a short period of time. Therefore, a proper coastal defense system is necessary for saving critical infrastructures and lives during tsunami propagation. The partial failure of a multi-billion dollar concrete sea wall upon the impact of the Tōhoku tsunami in 2011 invigorated the debate about possible nature-based approaches to mitigating tsunami risk [e.g., 11, 32, 179]. Nature-based coastal features such as mangroves, marshes, etc., are popular as a tsunami mitigation design because, apart from providing important services like wave attenuation, reducing shoreline erosion, and increasing shoreline protection, these can also help to promote ecotourism. After the Indian Ocean tsunami event, damage assessments were conducted, and the importance of the role of natural features was highlighted in reducing the wave impact [e.g., 7, 30, 34, 35, 86, 91, 165, 208, 209], but the casual contribution of vegetation in reducing damage to coastal regions has remained contentious [e.g., 96–98]. Adding to the challenge of clearly identifying the potential protective benefit of vegetation are field observations from other contexts. For example, as illustrated in Figure 1.1, the 2004 Indian Ocean tsunami annihilated coastal vegetation in Lhoknga, Indonesia, highlighting that there are no fail-safe approaches to countering a tsunami's destructive power. A similar phenomenon was observed in Rikuzentakata, Japan, where almost 70,000 pine trees were destroyed and

washed away due to the 2011 Tōhoku tsunami. However, while the Rikuzentakata coastal forest was not able to withstand the 2011 event, it might have mitigated the impacts of the 1933 Showa Sanriku tsunami and the Chilean tsunami in 1960 [e.g., 124, 157].

In spite of ongoing debate about the importance of coastal forests in tsunami-risk mitigation, coastal forests are preferred due to three main reasons.

1. Trees can reduce the energy of tsunamis by reflection and dissipation.

2. Trees with large trunk diameters can prevent objects from being washed by the undertow and prevent debris from damaging coastal structures like buildings.

3. Long-rooted trees can hold the soil together, which may prevent tsunami-induced scouring.

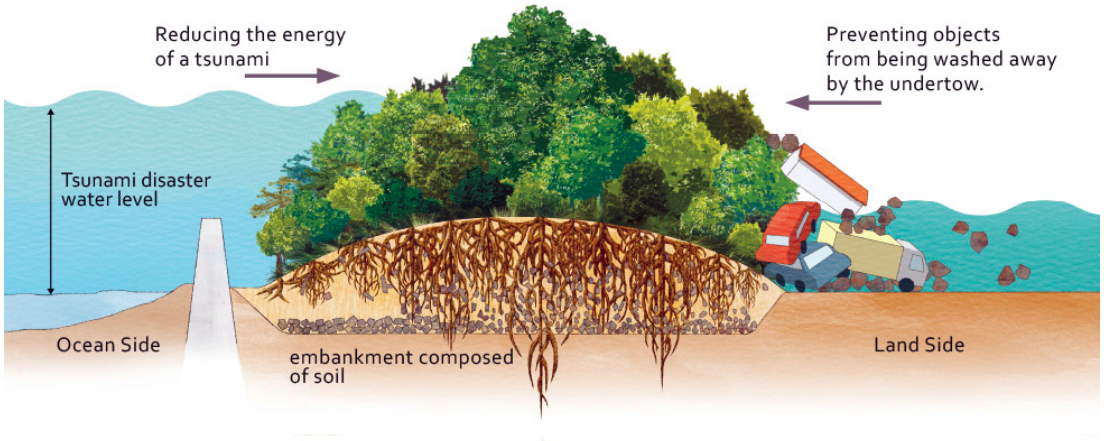

Figure 1.2 Representation of the potential benefits offered by vegetated coastal hills on a large tsunami.
Image from *Morino Project [176].*

The potential benefits of vegetation in the context of protecting the shoreline are graphically presented in Figure 1.2. As nature-based elements become an important component of tsunami risk mitigation, vegetation is often combined with sea walls or hillscapes in order to provide maximum protection against tsunamis. One example of this approach is the coastal mitigation park or green belts in which vegetation

is combined with designed hillscapes. Tsunami mitigation parks are employed in Indonesia, Japan, and Chile (see Figure 1.3) to strategically protect coastal infrastructures and communities. However, we still lack the fundamental knowledge of tsunami vegetation interaction and how different vegetation parameters can affect tsunami wave attenuation, hence inspiring the current dissertation.

1.2 Objectives

The present dissertation aims to understand the importance of different tree parameters in tsunami energy attenuation by analyzing the effect of trees on tsunamis. The goal of this present dissertation is to quantify how the energy dissipation and partial wave reflection from coastal trees vary with different degrees of rigidity, the gap between trees, and the number of trees. We approach this problem numerically by solving the Navier-Stokes equations for turbulent flow with a free surface and fluid-structure interactions (FSI) using the multi-physics software package *Alya*, described by Houzeaux et al. [71, 72]. The FSI module allows to capture the two-way coupling between the fluid flow and the mechanical bending of the trees due to wave forcing. While the present work is motivated by prior field studies, we study the interactions between fluid flow and tree rigidity in an idealized laboratory-like setting that is not intended to mimic any specific tree species or location. To enable the transferability of our results, we consider a non-dimensional parameter range that is representative of tsunami flows and realistic hardwood properties [59]. In this dissertation, we implement a two-way coupling fluid-structure interaction model to investigate tsunami flow energy damping performance for different vegetation parameters. We use circular base cylinders as an idealized approximation for tree trunks following previous work by Nepf [160] on emergent, flexible plants in flow.

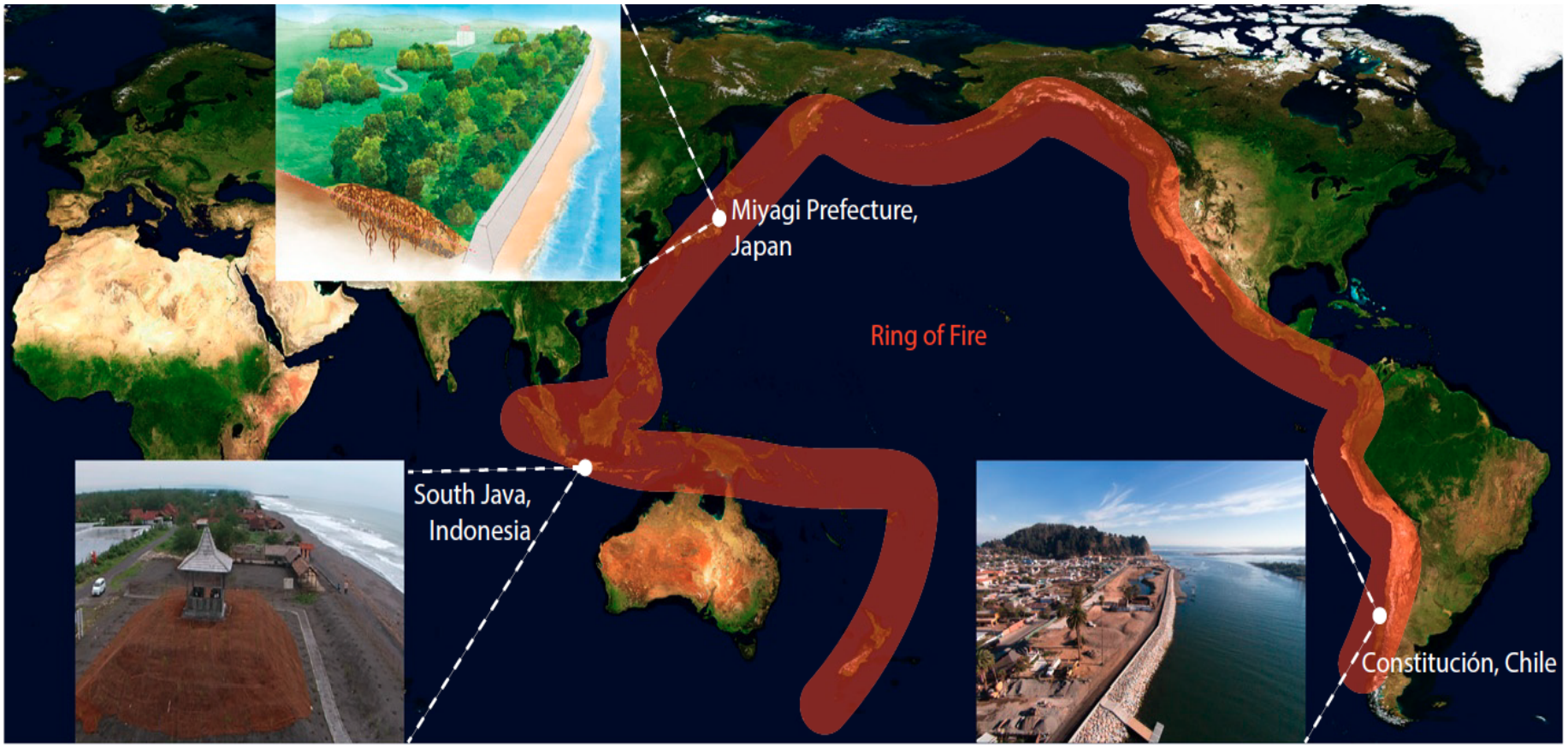

Figure 1.3 Coastal defense system constructed along the different regions in the ring of fire, for example in Indonesia, Japan, and Chile.
Source [128].

In our study, wave energy attenuation is quantified via energy flux instead of inundation distance which remains relatively unchanged, as discussed by Lunghino et al. [128] because the damaging power of tsunami is dependent on the flow energy.

1.3 Outline of the Dissertation

The remainder of this dissertation is organized as follows: Chapter 2 introduces a brief discussion on tsunami generation, propagation, and tsunami wave vegetation interactions. It is followed by a general description of different numerical schemes employed in the tsunami research field. Chapter 3 describes the methodology where the numerical model adopted in our study is discussed. Chapter 4 shows the validation of the numerical model employed in our study against the experimental studies, followed by details of numerical setup, scaling parameters, and energy flux definitions. In Chapter 5, we present the energy budget comparisons for different vegetation parameters, including velocity and turbulent kinetic energy distribution and wave profile evolution. In Chapter 6, we discuss how our results could inform the ongoing debate on nature-based approaches to tsunami-risk reduction, and finally, conclusions are presented in Chapter 7.

CHAPTER 2

ADVANCES IN TSUNAMI RESEARCH

2.1 Tsunami Generation and Propagation

Tsunamis are long waves that propagate in deep water, and the long wave is followed by a series of short trailing waves. The leading wave is very long in the deep water, with a wavelength in the order of hundreds of kilometers. In contrast, the amplitude of the wave is relatively small (around 1 m). But the scenario changes when a tsunami wave propagates from deep water to shallow water. In shallow water, the tsunami waves amplitude increases and can reach around 50 m, known as shoaling.

Shoaling happens when the water waves experience resisting force from the seabed in the shallow region. As a result, waves slow down and start to cluster together, thus resulting in a decrease in the wavelength. During shoaling, having shorter wavelength results in the increment of the amplitude of the wave. This can be explained by the energy conservation theory. When the tsunami wave propagates from the deep water, the energy is mostly in the form of kinetic energy. During shoaling, since the wave velocity decreases, the energy is converted into potential energy, thus increasing the potential height and wave amplitude. Figure 2.1 shows the concepts of the tsunami shoaling process.

The main reason tsunamis are dangerous in terms of damaging effects is shoaling. Since tsunamis have a very high wavelength in the deep ocean and in each wavelength, a high volume of water is involved during shoaling; this can get as high as the water gets into the shallower region. So even when tsunami wavelength decreases during shoaling, tsunamis still can have a relatively long wavelength, which is why they keep flowing inland over longer periods. The amount of shoaling by a tsunami is described by the term 'run-up,' which is marked by the vertical height

of the wave crest above sea level at the furthest point of the inland region before it dissipates. The inundation distance is a measurement of the furthest horizontal point reached by the tsunami.

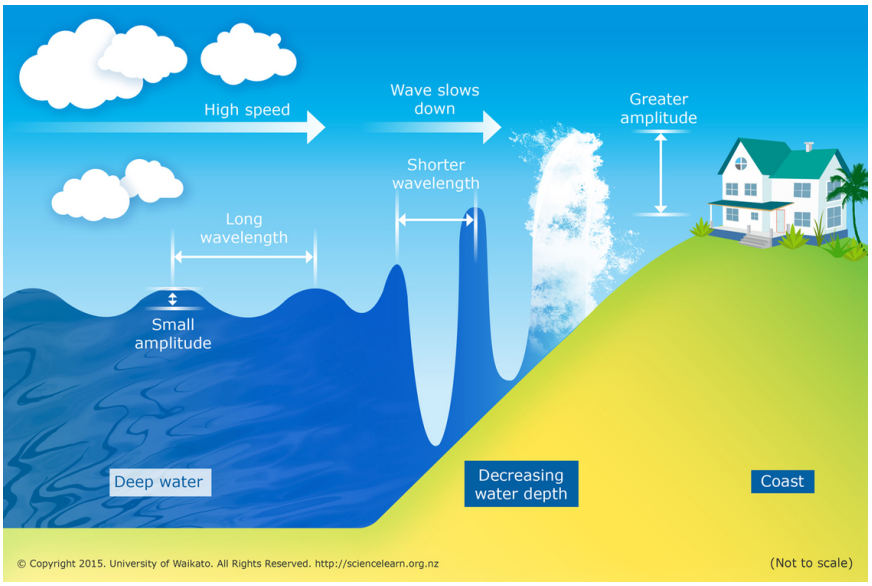

Figure 2.1 Tsunami shoaling and propagating from deep ocean to the shore. *Source [75].*

The run-up stage is the most destructive, but to understand the tsunami run-up process, it is very important to understand the tsunami generation and propagation first. That is why initial tsunami research was mainly focused on tsunami generation [e.g., 13, 20, 49, 64, 65, 90]. These studies are important to provide valuable insight into tsunami research. Initial studies on tsunami generation considered tsunamis as solitary waves because the studies by Hammack and Segur [64, 65] show that solitary waves are formed due to positive initial disturbance. Later other studies have been conducted by assuming earthquake-generated tsunamis as a representation of solitary waves [119–121]. Madsen et al. [138] first contradicted the claims made by earlier studies, and they concluded that real tsunamis could not be represented in terms of solitary waves. The main drawback is that the wavelength in the solitary waves cannot be expressed independently of wave height, and the real tsunami wavelength is

much longer than solitary waves. They also explained that in the solitary waves, the propagation distance required to generate tsunami-like phenomena would be higher than the circumference of the earth. Hence real tsunamis can't turn into solitary waves. Later, Madsen and Schaeffer [135] suggested that tsunami events can be represented in terms of single, sinusoidal, and N waves. Single waves are similar to solitary waves in shape, but unlike solitary waves, the wave duration and height can be expressed independently. The N waves are composed of positive and negative single waves. Therefore, they can be expressed as leading elevation or depression tsunami waves. Even if the solitary wave can not be represented as a real tsunami, the solitary waves have been used mainly for model validation. They also satisfy the Korteweg de Vries equation [69], thus having a strong theoretical background which is helpful for model validation and benchmarking.

The propagation of tsunamis can be accurately modeled by shallow water equations, which are derived by depth-integrating the Navier-Stokes equations, where the horizontal length scale is much higher than the vertical length scale. Since a tsunami wavelength is much higher than its wave amplitude, shallow water equations are an excellent choice for tsunami propagation in the deep-sea region [183, 214]. The linear shallow-water model, nevertheless, has no dispersion. Closer to the shore region, as a tsunami wavelength compresses, its amplitude grows due to shoaling, making a linear approximation no longer valid. In nonlinear shallow water (NLSW) equations, nonlinear advective terms, which are retained, become important when the free surface height is of the same order of magnitude as the water depth. The NLSW model is the preferred choice over the linear shallow-water model, as the NLSW model can be reformulated to handle wave dispersion. However, it may still lead to erroneous results for long-term propagation, even if the wavelength of the wave is longer than the depth. As Khakimzyanov et al. [99] argued, the NLSW model predicts only the first significant wave hitting the shore. This indicates that the formation of an undular

bore can not be predicted by NLSW [62]. Kim and Lynett [102] furthered this work by examining undular bores with both Boussinesq and NLSW models, concluding that the NLSW model under-predicted the surface elevations and velocities of the wavefront, whereas the Boussinesq model correctly predicted undular bores.

The Boussinesq approximation is based on the approximation of neglecting the vertical coordinate from the flow equations like the NLSW model. Unlike the NLSW model, the Boussinesq model still retains some vertical variations of the flow. Long wave equations are obtained through perturbation expansions in $\mu = d/L$, where the water depth and the wavelengths are d and L, respectively. In the NLSW equations, all μ terms are neglected, whereas, in the Boussinesq approximation, the second order in μ is retained. According to the NLSW theory, the horizontal velocity is uniform in a vertical direction, and the pressure is hydrostatic. Therefore, the vertical coordinate, z, vanishes from the equations. In Boussinesq approximation, the continuity and momentum equations are depth-integrated to remove the variability of parameters along z. The dispersion characteristics are dependent on the order of the wave equation. Over the years, fully nonlinear Boussinesq type equations have been improved by modeling dispersion properties. Madsen et al. [139] used linear shallow water and linear Boussinesq method to generate a transient wave with a highly dispersive tail and found that a non-dispersive shallow water model can only capture the leading wave, which is generally overestimated. When tsunamis propagate over a long distance on the open ocean, the dispersive wave may evolve. Moreover, dispersion becomes more important when undular bores will form at the leading tsunami wave front due to shoaling. Therefore, Hsiao et al. [73] formulated highly accurate, fully nonlinear Boussinesq equations in which the term $O(\epsilon^0\mu^2)$ (ϵ is dimensionless amplitude $= A/d$ where A is amplitude, d is water depth) is responsible for leading dispersion of the wave. By modifying or omitting higher-order terms in the equation proposed by [73], we can get different types of Boussinesq equations

which were used in [95, 163]. Extensions of higher-order long-wave equations have been implemented in the literature [136, 137], where progress has primarily been made with respect to higher-order nonlinearity and dispersion during propagation in mildly varying bathymetries. Fuhrman and Madsen [49] used a higher-order Boussinesq model to simulate both landslide and underwater earthquake-generated tsunamis and showed that it was capable of capturing the full cycle of tsunami evolution, subsequent propagation, and run-up.

Apart from analytical and numerical studies, experimental studies are also conducted to generate tsunamis. The main drawback of the experimental studies is that they suffer from large-scale problems. Because a full-scale tsunami has a wavelength in the order of hundreds of kilometers with a time period lasting hours, it is impossible to capture tsunami phenomena in the experimental lab unless problems have been scaled down. Schimmels et al. [191] and Sriram et al. [199] successfully generated a properly scaled tsunami with the help of a wave paddle. In spite of ongoing debates on whether experimental models can capture the tsunami phenomenon correctly, these studies show promise in the context of generating tsunami waves in laboratory settings. One of the other concerns about scaling tsunamis is the generation of long tsunami waves in the scaled model. Jiang et al. [89] argued that both the time and length scale could not be down-scaled in the experiment using Froude similarity laws. Since tsunami waves have time periods in the order of hours, it is a considerable challenge to generate long-period waves by the wavemaker devices in experimental work. Despite new proposals made by Rossetto et al. [187] and Goseberg et al. [58] to generate long-period waves, there is still an open challenge to generate a properly stable and scaled wave experimentally.

2.2 Tsunami Run-up and Inundation

Plenty of field surveys are conducted where tsunami run-up height and inundation distance are provided after tsunami events [e.g., 5, 18, 132, 156, 196, 205]. These studies provide useful information on propagation for different types of tsunamis, which are required for benchmarking by numerical simulations. Apart from field surveys, analytical studies are also conducted to provide an insightful understanding of tsunami run-ups. The analytical study on run-up was first conducted by Green et al. [60], who provided a solution for the propagation of long-wave. Later, the analytical models are further extended to study the nonlinear wave propagation [e.g., 25, 94, 134, 203].

Experimental studies on tsunami run-ups, where solitary waves are not used, are limited. These studies use either long waves or bores to capture run-ups. Matsuyama et al. [148] conducted an experimental study in 200 m long flume where tsunami wave run-up and propagation on a flatbed and varying slopes are studied. This study mainly focused on studying wave transformation and breaking instead of analyzing run-up height and inundation distance. A similar study was conducted by Kihara et al. [101], where two different tsunami-like waves are generated in 205 m long flume. Apart from studying wave breaking, wave inundation and velocity profiles are also compared for different waves. Most of the experiments mainly focus on the long wave propagation and wave reflection from the different slopes. [e.g., 29, 40, 58, 191, 199].

Numerical studies offer an attractive supplement to experimental work because, unlike experimental studies, they do not suffer from large-scale problems. There have been numerous numerical studies conducted, initially based on shallow water (SW) and Boussinesq theory (B) approximation. But later, due to the increase in high-performance computing, three-dimensional studies (NS) have also been conducted. Table 2.1 lists all the numerical codes that have been developed and used to simulate tsunami propagation. Lynett [130] used both nonlinear shallow

Table 2.1 List of Different Numerical Codes Developed and Implemented in the Tsunami Research Field, from Marras and Mandli [140]. Acronyms in this Table: SW: Shallow Water, B: Boussinesq, $N-S$: Navier–Stokes, SPH: Smoothed Particle Hydrodynamics, LES: Large Eddy Simulation, WM: Wall Modeled LES, $RANS$: Reynolds Averaged NS Equations, FSI: Fluid-Structure Interaction, and MP: Multi-Phase Flows

Model	*Space Dimensions*	*Eqn.*	*Turbulence*	*Wave Break.*	FSI	MP
GeoCLAW [14]	1D/2D/2D$\frac{1}{2}$	SW	No	No	No	No
NUMA2D [56, 141, 143]	1D/2D	SW	No	No	No	No
MOST [218]	1D/2D	SW	No	No	No	No
TUNAMI [84]	1D/2D	SW	No	No	No	No
NAMI-DANCE[84]	1D/2D	SW	No	No	No	No
COMCOT [233]	1D/2D	SW	No	No	No	No
CEA [50, 184]	1D/2D	SW	No	No	No	No
SELFE [243]	1D/2D	SW	No	No	No	No
TsunAWI [66]	1D/2D	SW	No	No	No	No
VOLNA [43]	1D/2D	SW	No	No	No	No
TsunaFlash [175]	1D/2D	SW	No	No	No	No
Delft3D [186]	1D/2D	SW	No	No	No	Yes
FUNWAVE [95, 195]	1D/2D	B	No	No	No	No
COULWAVE [103, 131]	2D	B	No	No	No	No
NEOWAVE [239]	2D	B	No	No	No	No
GPUSPH [235]	3D SPH	$N-S$	No	Yes	No	No
SCHISM [242]	1D/2D/3D	$N-S$	$RANS$	Yes	No	No
COBRAS [122, 123]	2D/3D	$N-S$	$RANS$	Yes	No	No
TSUNAMI3D [70]	2D/3D	$N-S$	$RANS$	Yes	No	No
waves2FOAM [88, 111, 112]	2D	$N-S$	$RANS$	Yes	No	No
Alya [158, 232]	1D/2D/3D	$N-S$	$LES/WM/RANS$	Yes	Yes	Yes

water and the Boussinesq model to understand the effect of a shallow shelf obstacle on the nonlinear long-wave run-up. He used the dissipation term to capture the wave breaking [129] and showed that both models were able to capture the breaking of waves. Lunghino et al. [128] studies tsunami run-up over planer beach with a tsunami mitigation park (a combination of hillscape and vegetation) on-shore to quantify how much tsunami energy can be reflected to understand the degree of mitigation. The study was made with the help of the NLSW model with a dynamic dissipation coefficient to handle the dispersion. The main limiting factor of the shallow water model is that it is incapable of evaluating the multi-scale, multi-phase, turbulent flow features as a tsunami runs inland and interacts with the coastal structures such as vegetation or hillscapes.

While a tsunami propagates through the open water, the flow can be manifested as quasi two-dimensional. Once the flow reaches shore and moves inland, it becomes inherently three-dimensional and heavily multi-phased as a large number of sediments (sand, dirt, debris) has been scoured off the sea bed and entrained. Even if the depth-averaged shallow-water, Boussinesq approximation in 1D or 2D are powerful in capturing regional-scale inundation but are more limited in estimating forces on individual structures [140]. By comparing a 2D against a 3D flow, Qin et al. [177] demonstrated that the solution of the 3D Navier–Stokes equations is required to quantify impact with due precision. With increased computing power, three-dimensional computational fluid dynamics (CFD) models are the best choice to capture the full-scale tsunami phenomenon because to be able to provide the optimal design for the tsunami mitigation system; it is imperative to understand the underlying physics of tsunami turbulent flow and flow-obstacles interactions. Direct numerical simulation (DNS) can be used to capture both the large and smallest turbulent (Kolmogorov) length scales. However, very fine spatial and temporal resolutions are required because the size of the smallest turbulent scales decreases

with increasing Reynolds numbers. That is why the computational cost of DNS is directly dependent on the Reynolds number (Re). Most DNS applications [e.g., 104, 161, 168, 190] are, therefore, limited to relatively low Reynolds number flows within a small computational domain.

The alternatives to the DNS to capture the turbulent flow characteristics are the Reynolds Averaged Navier-Stokes (RANS) and the Large Eddy Simulation (LES) method. Horrillo et al. [70] implemented the RANS model and validated the TSUNAMI3D code using a standard tsunami benchmark problem. The numerical results presented in their study matched well with the experimental benchmark problem. Yet, small discrepancies between the experimental and numerical results were reported, which were caused due to the incapability of resolving energy loss at the small scale of the transient turbulence process. Recently, Larsen et al. [111, 112] performed a full-scale RANS tsunami simulation, which focused not only on tsunami run-up, propagation, and shoaling but also on the boundary layer dynamics and bed shear stress. This study provided fundamental new insights into the local scour process and sediment transport phenomenon. The main limitation of this study is that the simulation is limited to the two-dimensional problem, leading to an over-prediction of local turbulence during wave breaking. Even if it was claimed that the numerical artifacts generated due to the two-dimensional problem would not affect the run-up and draw-down process, nothing could be concluded unless a three-dimensional analysis was done. Yang et al. [240] studied tsunami-induced force on structures for different protecting barrier configurations and estimated the tsunami mitigation effect by implementing the RANS model. Even if RANS is a better choice than depth-averaged shallow water equations, RANS is incapable of capturing instantaneous flow statistics. RANS also performs poorly when used to calculate separating or free shear flows.

LES, on the other hand, is capable of modeling small scales via sub-grid scale (SGS) modeling. In terms of computational cost, LES is more costly than RANS but cheaper than DNS. At the boundary layer region near the wall, LES is almost as costly as DNS [113, 188]. Therefore, the implementation of LES in tsunami research is limited. Christensen [31] used LES for simulating turbulence in wave breaking. Later, Wu and Liu [238] conducted LES for landslide-generated tsunamis and shoreline movements using a set of near-wall damping functions to approximate the eddy viscosity at the first cell adjacent to the wall for near-wall treatment. But this study was mainly limited to velocity fields and free surface profiles in landslide-generated breaking wave run-up and run-down on a sloping beach. Recently Kim et al. [105] implemented LES to understand turbulent flow characteristics in dam-break swash flows on a rough-planar beach. The model successfully predicted span-averaged velocity profiles and bed shear stress and analyzed the turbulence production and turbulent coherent structures during uprush and backwash. These analyses were crucial to understand the sediment transport phenomenon and tsunami-induced boundary layer dynamics. Sarjamee et al. [189] studied tsunami mitigation by measuring the hydrodynamic forces on vertical structures with and without the presence of mitigation walls using a large eddy simulation model. They also compared the performance of the RANS and LES turbulence models and found that the LES approach performed better than the employed RANS models, such as $k-\varepsilon$ and $k-\omega$ in terms of properly capturing the turbulence at the wake region.

Even if Navier-Stokes-based models provide a better aspect of understanding tsunami wave impacts, these models (either RANS or LES) come with their own challenges, such as the need for careful validation [111] and sufficient resolution in boundary layers [e.g., 112, 236]. Fortunately, there is an increasing number of laboratory experiments that are essential for the validation of numerical simulations [7, 85, 110, 181, 220]. Similarly, increasing computational power and data storage

have solved some issues, particularly those related to insufficient resolution, making scientific computing for large-scale tsunami simulations increasingly accepted [e.g., 10, 204]. This increased interest in high-performance computing for tsunami run-up has led to several inter-comparison efforts that add valuable transparency to high-fidelity computational approaches [54, 81, 107, 149, 150, 229, 234, 241].

2.3 Tsunami Mitigation

Numerous research studies have been conducted on tsunami wave run-up and inundation, yet there has been considerably less research on tsunami mitigation. Due to higher computational cost, studies on tsunami mitigation using three-dimensional Navier-Stokes-based models are limited. However, a few studies were conducted based on depth average models to investigate the tsunami hydrodynamic interactions with coastal structures. Lynett [130] studied the effect of obstacles on the nonlinear long-wave run-up by implementing the Boussinesq model and varying the nonlinearity (ϵ = wave height/water depth) of the wave, finding that obstacles are useful in terms of reducing the run-up height mainly for high nonlinear waves. This study was limited to 2D numerical simulations. Venayagamoorthy and Fringer [229] analyzed the interaction of internal gravity waves with a shelf break to quantify the percentage of reflected and dissipated energy fluxes and found that the reflected energy flux is strongly dependent on the bathymetry slope. Even if this study was two-dimensional, it offered the idea of quantifying the tsunami mitigation effect for different configurations. Lunghino et al. [128] conducted energy flux analysis in different hillscape configurations to quantify tsunami energy reflection to understand the degree of mitigation. They found that a tsunami wave amplitude smaller than the hill height would lead to a significant amount of energy reflection, a key mechanism to reducing tsunami risk. One of the important findings of this study is choosing a proper metric that is indicative of protective benefit. In much of the literature about coastal risk

reduction, this metric is inundation distance, defined as the horizontal distance that a tsunami reaches inland. The authors show that even if the inundation distance remains almost unchanged, tsunami flow energy can be greatly reduced in the presence of hills (see Figure 2.2). However, this study mainly considered energy reflection as a metric of coastal mitigation and did not take into account the energy dissipation and tsunami-induced scouring, which can affect the potential benefits provided by hills.

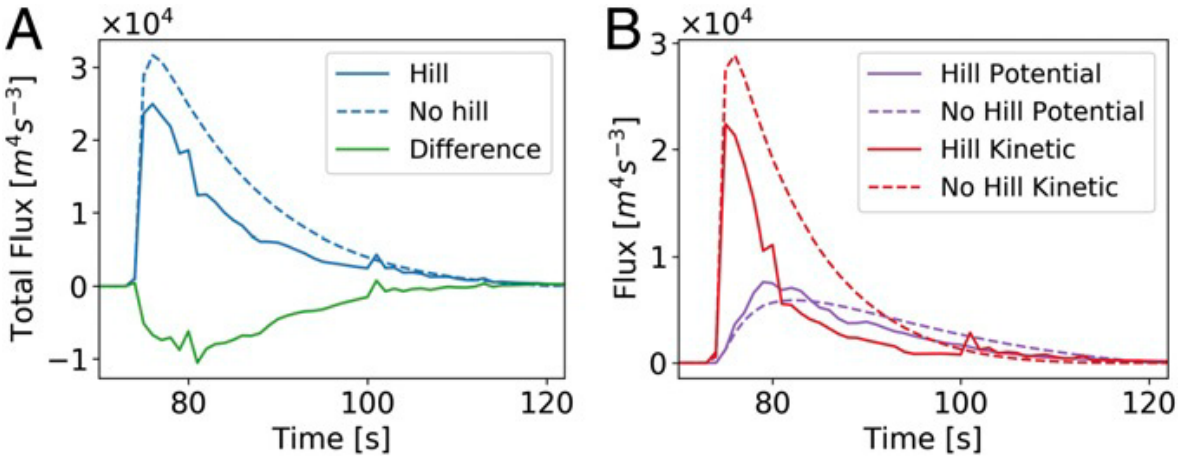

Figure 2.2 Energy flux reduction with presence of hills [128]. Left (A): Evolution of total energy flux with and without hills, and right (B): Comparison of the kinetic and potential components of energy flux in the presence and absence of hills.

One of the alternate ways to quantify the protective benefit is by measuring hydrodynamic forces on coastal structures. Forces on coastal structures can be greatly reduced if a proper coastal defense system is implemented to dampen the tsunami energy. A number of studies have examined how tsunami mitigation is quantified by measuring the tsunami-induced hydrodynamic loading exerted in various structures. Arnason et al. [2] calculated hydrodynamic forces by generating tsunami bore in the dam-break wave on the wet surface for different wave conditions. Later, Yang et al. [240] studied a tsunami-induced hydrodynamic force exerted on structures for configurations of different protecting barriers. They found that if a dummy house is placed at an optimum distance before residential houses, the hydrodynamic forces hitting residential areas could be significantly reduced. The degree of force reduction depends

primarily on the distance between the barrier and the houses and the width of the barrier. Still, it is doubtful whether building-shaped barriers can mitigate tsunami waves, as the study claims that the degree of mitigation depends on the width of the barrier. Once the barrier width is increased indefinitely, it would become nothing but a thick wall, and a wall designed to protect the Tohoku coasts in Japan failed to mitigate the 2011 tsunami, showing that a wall is not a viable option for tsunami mitigation. However, this study does not examine the effect of multiple barriers on tsunami mitigation. Sarjamee et al. [189] conducted a numerical analysis to assess the influence of mitigation walls with various cross-sections on the tsunami-induced hydrodynamic force exerted on freestanding structures. The analysis was limited to examining curved and inclined walls and concluded that the distance between the mitigating walls and structures could play a crucial role in force reduction. Curved mitigating walls also appear to be more effective in mitigation as compared to inclined walls. These studies are useful in understanding the importance of optimum configurations of barriers in mitigation.

2.3.1 Importance of vegetation in mitigation

The idea of using vegetation as bioshields stems from the damage assessment conducted after the 2004 Indian Ocean tsunami, where the reduction of tsunami wave impact near the coastal vegetation was pointed out [e.g., 30, 34, 86, 91, 208, 209]. One of the key challenges of using vegetation as a coastal defense system is to identify proper vegetation parameters which will affect the tsunami energy reduction. For example, during the 2011 Japan tsunami, almost 70,000 pine trees were uprooted in Rikuzentakata, indicating that there are no straightforward approaches to attenuating the tsunami wave energy.

One step towards adding clarity to the ongoing debate about the role of vegetation in tsunami-risk mitigation is to distinguish between different ecosystems and the differing effect they have on tsunami run-up. Vegetation cannot fully stop

a tsunami as compared to sea walls, and the effectiveness of coastal forests depends both on the magnitude of the tsunami and on the structure and response of the trees. To leverage vegetation in tsunami-risk mitigation, we need to quantitatively understand the mechanism through which the vegetation interacts with the wave, the limits of this mechanism, and the degree to which it leads to a reduction in the energy of the tsunami [206]. The differences can appear quite subtle: for example, a detailed field assessment after the 1998 tsunami in Papua New Guinea found that Casuarina trees were able to withstand wave impact better than palm trees. Some palm trees were uprooted or snapped off at mid trunk level, transforming into projectiles and increasing rather than decreasing damage [37].

The lessons learned from both the Japan and the Papua New Guinea tsunami indicate that advancing our understanding of the protective benefit of coastal forests requires not only quantifying the effect that the trees have on the tsunami but also an analysis of the effect that the tsunami has on the trees. As tsunamis propagate and interact with trees, the structural deformation of trees also changes the flow structures around them. This can vary based on the different species of trees. For example, Casuarina trees and palm trees differ in the context of the bendability of their trunks, with Casuarina trees having more flexible trunks. More bendability, nevertheless, is not necessarily better. In fact, field surveys in Sri Lanka and Thailand after the Indian Ocean tsunami suggested that older and relatively sparse belts of *Casuarina equisetifolia* withstood the tsunami but did not appear to provide much protection [206], emphasizing the potential importance of forest density in addition to individual tree properties. The effect of coastal forest density is further investigated experimentally and numerically by Iimura and Tanaka [81], Pasha and Tanaka [169] where the supercritical flow is observed near the downstream of vegetation, which causes hydraulic jump and hence results in energy loss.

Apart from forest density, the diameters of the vegetation can also play an important role since the higher diameter of trees can withstand tsunami wave force and, therefore, are less prone to breakage. As reported by Tanaka et al. [209], trees (for e.g., *Bauhinia*, *Zizyphus*) with small trunk diameters ($0.05 - 0.1\,\mathrm{m}$) were completely destroyed by the Indian Ocean tsunami in Sri Lanka, whereas trees with larger trunk diameters ($> 0.3\,\mathrm{m}$) can effectively withstand the tsunami wave forcing and trap the debris of broken trunks. Moreover, the forest density can simultaneously affect the protection because due to a larger gap between debris, the floating debris can easily pass through the gap between tree trunks and cause serious damage to coastal structures. In order to leverage Navier-Stokes-based simulations to improve understanding of tsunami impacts on vegetation, Kundu et al. [107] conducted LES and RANS simulations to analyze the flow hydrodynamics for a different arrangement of circular vegetation and studied how the characteristics of unsteady wakes generated behind the cylinders can be affected by multi-cylinder arrangements. Maza et al. [152] solved the Unsteady Reynolds Averaged Navier-Stokes (URANS) equations to study the interaction of a solitary wave with vegetation, where vegetation was modeled by rigid cylinders after the experiments by Huang et al. [74]. The same authors [151] built a 2D linear model for vegetation motion and simulated the swaying dynamics of submerged vegetation. An extension to 3D cylinders is presented by Tsai et al. [224] where a rigid motion of the cylinders is allowed around a fixed point on the ground. Nevertheless, the above-cited study does not account for cylinder bendability and elasticity along its length; instead, the swaying motion is captured by fixing the cylinder with a torsional connector.

While high-fidelity simulations provide a high level of detail regarding the flow field around submerged vegetation, post-processing is necessary to distill these details into a simple metric that is indicative of protective benefit. In much of the literature about the role of vegetation in coastal risk reduction, this metric is inundation

distance, defined as the horizontal distance that a tsunami reached inland. In fact, Kerr and Baird [96] criticized field studies focused on associations between vegetation and damage from satellite data [30, 35] because vegetation did not appear to have a mitigating effect on inundation distance. However, inundation distance as a metric of protective benefit might be more valuable in the storm-surge context for which it was originally introduced by Fosberg and Chapman [47], USACE [227] than for tsunamis because the main destructive potential of a tsunami is related to the energy transported, not to the presence of water per se.

CHAPTER 3

METHODOLOGY

In this section, we present the numerical model adopted in our study. Since we aim to solve the 3D Navier-Stokes equations of multiphase flow with fluid-structure interaction (FSI), we rely on the flow solver *Alya*, a massively parallel multi-physics finite element solver which is developed at Barcelona Supercomputing Center (BSC). *Alya* is built in such a way that each module corresponds to a single set of Partial Differential Equations. To couple the multi-physics problems, the required modules should be active and have well-defined interfaces and connection points [232]. *Alya* has been tested and used for many years on the leading supercomputers worldwide, showing nearly-linear scalability of up to 100k CPUs. Also, *Alya* has the capability to solve FSI (fluid-structure interaction) problems, which is crucial to the understanding of the role of flexible vegetation in tsunami wave attenuation. The present chapter consists of three sections. Section 3.1 describes the two-fluid Navier-Stokes equation, numerical challenges, and strategy to tackle these challenges. Section 3.2 provides a brief discussion of different methods of free surface tracking and more discussion on the model adopted by *Alya*. In Section 3.3, different schemes to capture solid-fluid interface and the model employed in the current numerical method are described. Finally, we describe the different turbulence modeling and wall functions used to capture turbulence near the wall in Section 3.4.

3.1 Two-fluid Navier-Stokes Equations

The interaction of a two-phase fluid flow (water and air) in the moving domain $\Omega = \Omega_1 \cup \Omega_2$ can be characterized by the following incompressible mass and momentum conservation equations [27]

$$\begin{aligned} \rho\left[\frac{\partial \mathbf{u}}{\partial t} + (\mathbf{u}\cdot\nabla)\mathbf{u}\right] - \nabla\cdot\boldsymbol{\sigma} &= -\rho g\mathbf{k}, \\ \nabla\cdot\mathbf{u} &= 0, \end{aligned} \tag{3.1}$$

where ρ is the density, $\mathbf{u}$ velocity vector, p the pressure, μ dynamic viscosity, $\boldsymbol{\sigma} = -p\mathbf{I} + 2\mu\mathbf{S}(\mathbf{u})$ is the stress tensor, $\mathbf{S} = \frac{1}{2}(\nabla\mathbf{u} + \nabla\mathbf{u}^T)$ rate of strain, and g is the magnitude of the acceleration of gravity which points downwards in the direction of $\mathbf{k} = [0, 0, 1]$. By replacing the definition of $\boldsymbol{\sigma}$ in Equation 3.1 we obtain

$$\begin{aligned} \rho\left[\frac{\partial \mathbf{u}}{\partial t} + (\mathbf{u}\cdot\nabla)\mathbf{u}\right] - \mu\nabla^2\mathbf{u} + \nabla p &= -\rho g\mathbf{k}, \\ \nabla\cdot\mathbf{u} &= 0. \end{aligned} \tag{3.2}$$

The density, velocity, pressure, and dynamic viscosity are defined as:

$$\mathbf{u}, p, \rho, \mu = \begin{cases} \mathbf{u}_1, p_1, \rho_1, \mu_1 & \mathbf{x} \in \Omega_1, \\ \mathbf{u}_2, p_2, \rho_2, \mu_2 & \mathbf{x} \in \Omega_2, \end{cases} \tag{3.3}$$

where Ω_1 is the subdomain of Ω occupied by the fluid number 1 and Ω_2 corresponds to the subdomain occupied by the fluid number 2. In this problem, fluid 1 and fluid 2 refer to water and air, respectively. The interface between the two phases is tracked via the level set function ψ. The details of the level set method are explained in Section 3.2.

At the two fluids interface Γ_{int}, the velocity and the stresses must be continuous. Thus, defining $\mathbf{n}$ as the unit outward normal to the two-fluid interface, the following conditions have to be fulfilled:

$$\begin{aligned} \mathbf{u_1} &= \mathbf{u_2} \quad at\ \Gamma_{int}, \\ (\boldsymbol{\sigma}_1 - \boldsymbol{\sigma}_2) \cdot \mathbf{n} &= 0 \quad at\ \Gamma_{int}. \end{aligned} \tag{3.4}$$

The Equation 3.2 is discretized using the finite element method with the Algebraic Sub-grid scale (ASGS) stabilization scheme [33]. Details on the implementation can be found in [71, 72].

For large scale problems, the discretized Navier-Stokes equations can be solved using iterative schemes taking advantage of their relatively low memory requirements and good parallelization properties. The most common approach is to split the velocity and pressure equations using fractional steps techniques [171, 178]. However, these methods can lead to errors due to the splitting, and therefore, artificial boundary conditions are required for the pressure to achieve pressure stabilization. In the implementation used in *Alya*, the pressure Schur complement [225, 226] is used as a pressure segregation method, which allows to uncouple velocity and pressure in an efficient way. As described in [71, 72], an Orthomin(1) solver is used to converge to the monolithic scheme via pressure Schur complement and minimize the Schur complement residual at each solver iteration, resulting in a well-conditioned system. This method has proven to be efficient since it uses simple algebraic solvers without the need for additional complex preconditioners with the capability of scaling up to thousands of processors.

3.2 Free Surface Tracking in Two-fluid Flows

Interface tracking of two-fluid flows is numerically challenging. The details of different schemes and the comparisons between them can be found in [173, 216, 223]. In general,

the methods are broadly classified into two main categories, fixed grid, and moving grid method. In the fixed grid method, a fixed computational mesh is used where the free surface is captured via an interface function. In the moving grid method, [180], the mesh is updated at each time step, and the interface tracking technique is employed to track the moving interface as the flow evolves. As described by Sethian and Smereka [193], the overview of these methods is described below.

The moving grid technique

This technique relies on an interface tracking method where the mesh is updated. In this method, if the interface is parameterized in the way, i.e., $\Gamma(t) = (x(s,t), y(s,t))$, equations for individual components are written ($\mathbf{x} = (x, y)$) as

$$\frac{\partial x}{\partial t} = u,$$
$$\frac{\partial y}{\partial t} = v.$$

Instead of using a fixed coordinate system, Navier–Stokes equations are solved based on a moving grid based on an Arbitrary Lagrangian Eulerian (ALE) formulation, which will be described in Section 3.3. The motion is approximated by differentiating with respect to s. The moving grid technique is robust and efficient. Nevertheless, remeshing of geometry can be required often, which can incur high computational costs, particularly in 3D complex flow problems.

The fixed grid technique

In the fixed computational domain, the interface capturing method is employed to approximate the position of a free surface. The interface function can be broadly defined in two ways which are described below.

(a) The volume of fluid method (VOF): In this method, the free surface is defined by a characteristic function $\chi(x, y, t)$, where χ is 1 at the fluid domain inside the interface Γ and zero outside of it. The motion of the characteristic function can be described by the transport equation as follows

$$\frac{\partial \chi}{\partial t} + \mathbf{u} \cdot \nabla \chi = 0.$$

In this method, all points inside the interface are advected via the velocity field. This method discretizes the underlying domain and assigns cells with values that represent the function χ in those cells. These values are typically zero in the cells occupied by the fluid 1 and one in the cells occupied by fluid two except in those cells cut by fluid front, which have $\chi \in [0, 1]$.

(b) The level set method: This method is similar to the VOF method where a smooth scalar function is defined, say $\psi(\mathbf{x}, t)$ ($\psi : R^2 \times [0, \infty) \rightarrow R$). However, in this method, at the interface, ψ is zero, and the motion of the smooth scalar function is approximated by:

$$\frac{\partial \psi}{\partial t} + \mathbf{u} \cdot \nabla \psi = 0. \tag{3.5}$$

In *Alya*, the level set has been implemented based on defining a smooth scalar function as described above. Here, the scalar function $\psi(\mathbf{x}, t)$ is defined over the computational domain Ω that is divided into subdomains Ω_1 and Ω_2 and allows to represent the interface implicitly. The positive values are assigned in the subdomain Ω_1, and negative values are assigned to the points belonging to subdomain Ω_2. The initial condition of $\psi(\mathbf{x}, t)$ is defined as

$$\psi_0 = \psi(\mathbf{x}, t = 0).$$

The initial condition ψ_0 is required to define the initial fluid front position. The free surface position is characterized by the iso-value contour $\psi(x, t) = 0$.

In the numerical solution of the level set equation, since the main idea is to have the function $\psi = 0$ at the interface between two fluids, a signed distance function ($|\nabla\psi| = 1$) is used to avoid having a function with large gradients. As the flow evolves, ψ changes and needs to be reinitialized in order to remain a signed distance function. This reinitialization can be achieved via redefining ψ for each node of the finite element mesh with the equation given below:

$$\psi = \text{sgn}(\psi^0)d,$$

where ψ^0 is the non-smoothed value of ψ, d is the distance from the node belonging to the fluid front, and sgn() stands for the signum of the parameter. The distance d is calculated via a geometrical method based on skd-tree, which is described in detail by Khamayseh and Kuprat [100]. This method involves searching a minimum distance between the node and the surface mesh during the reinitialization of the level set. However, this search can increase the computational cost significantly for a high grid density. Therefore, parallelized bounding volume hierarchy is used to speed up the search, which splits the bounding volume based on the number of cores and reduces computational costs.

In Equation 3.3, material properties are defined for two-fluids Navier-Stokes equations. Nevertheless, the material properties need to be smooth in the interface between two fluids; hence these parameters (μ , ρ) need to be approximated. To avoid the sharp changes of these parameters across the fluid interface, a Heaviside function is used [202] for smearing:

$$H_\epsilon(\psi) = \begin{cases} 0 & if \quad \psi < -\epsilon \\ \frac{1}{2} + \frac{\psi}{2\epsilon} + \frac{1}{2\pi} sin(\frac{\pi\psi}{\epsilon}) & if \quad -\epsilon \leq \psi \leq \epsilon \\ 1 & if \quad \psi > \epsilon \end{cases} \tag{3.6}$$

where ϵ is a tunable parameter that is proportional to the spatial-mesh size. In *Alya*, ϵ is set as three times the grid spacing along the normal direction with respect to the free surface ($\epsilon = 3\Delta x$).

3.3 Fluid-Structure Interaction

Over the years, the fluid-structure interaction (FSI) problem has drawn significant attention because of its presence in many physical, biological, and industrial systems [e.g., 3, 6, 24, 61, 125, 213]. When a solid body is deformed by the action of fluid flowing around it, the structure displaces this same fluid and modifies the flow itself. In order to take this into account, a two-way coupling is used to capture both the effect that the flow has on the solid body and the effect that the solid body has on the flow. As the solid body deforms, we update the solid-fluid interface at every time step as sketched in Figure 3.1. More details on how to formulate two-way-coupled fluid-structure interaction can be found in Bungartz et al. [22] and Bazilevs et al. [8].

One of the main challenges in the numerical simulation of FSI problems is the treatment of the solid-fluid interface, where the physical coupling conditions need to be implemented. There are mainly two ways to achieve the correct modeling of the physical situation. The first one is the monolithic approach, in which the flow and structural equation are discretized simultaneously and combined to form a global system. The advantage of this method is that it is robust and produces very accurate results. But, the monolithic approach does not allow the use of independent preexisting solvers for the fluid and the solid component of the problem. Examples of the use of the monolithic approach can be found in the works in [67, 76].

The second method is the partitioned or staggered approach, where the problem is solved separately. The solution to the full problem is achieved by implementing a suitable coupling algorithm between the solid and fluid problems. This approach allows the use of each solver independently [44, 45]. As in the free surface tracking problem described before, the tracking of the solid-fluid interface is a challenging task,

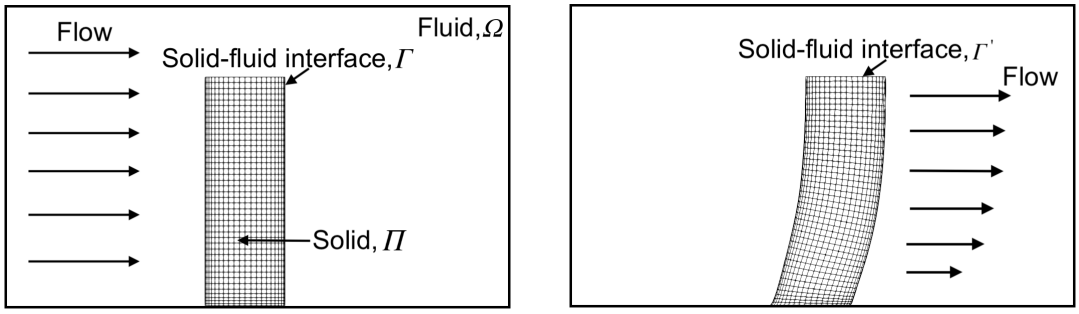

(a) Fluid domain Ω and solid domain Π separated by interface Γ.

(b) Solid deformed by fluid flow resulting in moving interface.

Figure 3.1 Two-way FSI: Fluid domain Ω is separated from the solid domain Π by an interface Γ, which is updated at every time step once the solid body is deformed. The new position of interface Γ' is tracked via Arbitrary Lagrangian Eulerian (ALE) formulation.

and different means can be used to achieve it. One possible approach is the interface capturing technique, in which fluid and solid equations are solved in a fixed grid, and an interface function has to be calculated to mark the position of the interface. Another approach is the interface-tracking technique, where the grid moves to track the interface position. In *Alya*, the staggered approach has been implemented along with the interface tracking technique to track the solid-fluid interface. One of the most common methods to treat the moving boundary problem is the Arbitrary Lagrangian Eulerian (ALE) formulation, in which fluid equations are written in a moving Eulerian reference system and cast into a moving grid that captures the moving interface. The movement of the interior grid points is characterized through a partial differential equation. For details, see the examples of the ALE formulation in [108, 146].

For an incompressible fluid, the Navier-stokes equations (see Equation 3.2) are coupled with Euler equations for solid dynamics, which are given below:

$$\rho_s \frac{\partial^2 \mathbf{d}_s}{\partial t^2} = \nabla \cdot \mathbf{P} + \mathbf{b}, \tag{3.7}$$

where ρ_s is the density of solid, $\mathbf{d}_s$ represents the displacement field of the solid, $\mathbf{P}$ indicates the first Piola-Kirchhoff stress tensor, and $\mathbf{b}$ is the body forces vector.

All the parameters and derivatives are defined using the Lagrangian formulation. This system of equations has to be solved with appropriate boundaries and initial conditions. At the fluid-solid interface, dynamic coupling conditions are imposed to maintain continuity in kinematic and dynamic quantities, which means that:

$$\begin{aligned} \mathbf{d}_f &= \mathbf{d}_s, \\ \mathbf{t}_f &= -\mathbf{t}_s, \\ \mathbf{u}_f &= \frac{\partial \mathbf{d}_f}{\partial t}, \end{aligned} \tag{3.8}$$

where $\mathbf{d}_f$ is the displacement of the solid interface inside the fluid domain and $\mathbf{t}_f$ and $\mathbf{t}_s$ are the traction vectors on the fluid-solid interface by the fluid and the solid respectively, $\mathbf{u}_f$ corresponds to the velocity of the fluid.

The fluid equations (Equation (3.2)) casted in the ALE formulation are

$$\begin{aligned} \rho_f \frac{\partial \mathbf{u}_f}{\partial t} + \rho_f[(\mathbf{u}_f - \mathbf{u}_m) \cdot \nabla]\mathbf{u}_f - \mu_f \nabla^2 \mathbf{u}_f + \nabla p_f &= -\rho_f g \mathbf{k}, \\ \nabla \cdot \mathbf{u}_f &= 0, \end{aligned} \tag{3.9}$$

where $\mathbf{u}_f$ represents the fluid velocity, ρ_f is the fluid density, and $\mathbf{u}_m$ corresponds to the domain velocity, which is obtained from the domain displacement $\mathbf{d}_m$, computed as the solution of a diffusion equation as stated below

$$\nabla \cdot [c_m \nabla \mathbf{d}_m] = 0, \tag{3.10}$$

where c_m is a diffusion coefficient that is computed element-wise in order to control the stiffness of the elements. In this equation, c_m is a discontinuous function that is computed as

$$c_m = AR/V,$$

where AR is the aspect ratio, and V is the volume of the element. For the solid dynamics problem, we discretize the Euler equation (see Equation (3.7)) using a

standard Galerkin method for large deformations with a Newmark time integration scheme, details of the numerical strategy can be found in [12] and [26]. The FSI problem in *Alya* is solved with an iterative staggered multi-code approach. As mentioned earlier, the staggered approach requires the proper use of a coupling approach between fluid and solid mechanics problems. There are two coupling algorithms proposed by Cajas et al. [23]: Gauss-Seidel and Jacobi algorithms. Both algorithms are tested, and the Gauss-Seidel algorithm is found to converge faster than the Jacobi algorithm. Hence we use a strong Gauss-Seidel coupling algorithm with an Aitken under-relaxation factor [38]. In each time step, we solve the fluid flow first to calculate the loads on the deformable structure required in the solid mechanics solver. We then solve the solid mechanics problem, and the new position of the body is sent back to the fluid mechanics solver. Convergence is reached when the residual of successive coupling iterations is less than the residual of coupling parameters.

For the detailed implementation of the FSI algorithm in *Alya*, see the works by Cajas et al. [23], who assess the parallel performance of the coupled code by conducting scalability tests for 30 million elements using 1280 MPI processes.

3.4 Turbulence Modeling

In the current study, we implement large eddy simulation (LES) to capture turbulence, and the small-scale eddies near the walls are treated via wall-modeled large eddy simulation (WMLES). Both methods are described below.

3.4.1 LES

In LES, large scales are computed explicitly, whereas the small scales are modeled via sub-grid scale (SGS) modeling [e.g., 117, 174, 188]. The small-scale motion from the main velocity field is extracted by spatial filtering using a grid filter kernel G with filter width Δ. When a filtering operation is applied for any vector or scalar quantity $\gamma(x)$

$$\gamma(x) = \overline{\gamma}(x) + \gamma'(x),$$

where the barred values are the filtered, resolved values that are separated from the un-resolved primed quantities at the sub-grid scale. If we apply the filtering operation to Equation 3.9, the filtering operation introduces a new unknown term, which is known as the SGS stress tensor [188]. After filtering, the modified equation becomes

$$\rho_f \frac{\partial \overline{\mathbf{u}}_\mathbf{f}}{\partial t} + \rho_f[(\overline{\mathbf{u}}_f - \mathbf{u}_m) \cdot \nabla]\overline{\mathbf{u}}_f - \mu_f \nabla^2 \overline{\mathbf{u}}_f + \nabla \tau_i^{sgs} + \nabla \overline{p}_f = -\rho_f g \mathbf{k}, \tag{3.11}$$

Here, $\tau_f^{sgs} = (\overline{\mathbf{u}\mathbf{u}})_f - (\overline{\mathbf{u}}\ \overline{\mathbf{u}})_f$ is the subgrid-scale stress tensor. SGS stress term needs to be modeled using a subgrid-scale model, and for modeling the SGS stress tensor, different methodologies can be adopted. The most popular method is based on the Smagorinsky model [198]. The main disadvantage of this model is that it suffers from over-prediction of sub-grid viscosity as the wall-normal distance approaches zero. Another approach is the WALE model (Wall Adapting Local Eddy Viscosity) [162], which is based on the square of the velocity gradient tensor and exhibits a proper near-wall behavior. There are other models available such as the Vreman turbulence model [231] and dynamic SGS model [52, 142] etc. In the current study, the Vreman turbulence model with a model constant $c_{\text{vr}} = 0.1$ is used in all of the simulations.

Classical LES incurs a high computational cost when modeling a turbulent boundary layer near the wall. Since a higher grid density is required as the size of the smallest turbulent eddies is dependent on the viscous length scale [113], higher

computational resources are needed, particularly in the near-wall region. Therefore, to reduce the dependency on higher grid density near the wall, WMLES is adopted, which is described in the next section.

3.4.2 Wall modeled large eddy simulation (WMLES)

To reduce the dependency on friction Reynolds number near the wall, Wall Modeled Large Eddy Simulation (WMLES) is adopted by many researchers [e.g., 4, 19, 46, 87, 126]. In WMLES, the grid used in the LES solver covers the whole domain and satisfies the standard LES resolution requirements at the outer boundary layer. In order to resolve the inner boundary layer, two main approaches have been developed: RANS/LES hybrid approach and the wall stress modeling approach. For details in RANS/LES hybrid approach, please see the works in [9, 55, 113, 197, 215]. In this study, the wall-stress modeling approach is used, in which an auxiliary wall-stress model is applied to resolve the inner boundary layer (viscous layer and log layer). This wall stress model requires the instantaneous LES velocity to produce the instantaneous wall stress as the output, which is then again parsed to the LES solver as a boundary condition. Even if the researchers applied the wall model to solve the turbulent boundary layer near the wall, there are a number of issues in WMLES. One critical issue is that the LES is under-resolved at first off the wall grid points. Kawai and Larsson [92] proposed a solution that the sampling height should be chosen in such a way that spatial (grid) resolution should be below the value of the sampling height, improving the prediction of wall shear stress. The main advantage of using WMLES is that grid spacing is directly proportional to the friction Reynolds number, drastically reducing the computational cost compared to classical LES.

In the classical finite element approach, the grids near the wall are ignored, which means it is assumed that a very thin region exists close to the wall, which is excluded from the mesh. In Figure 3.2, it can be seen that the mesh starts at a distance, d, from the wall. The thin region between the wall and the mesh is modeled

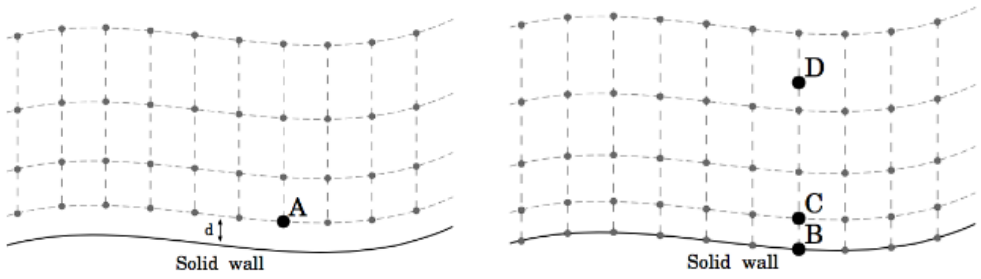

(a) (b)

Figure 3.2 Wall modeling approach (left) classical FE approach and (right) adapted approach extracted from Owen et al. [167].

using Reichardt's extended law of the wall. The velocity measured at a distance d from the wall is used to calculate the wall shear stress. According to Larsson et al. [113], this classical FE approach is equivalent to the hybrid LES/RANS model since the LES grid does not extend to the wall, as shown in Figure 3.2 (a). Owen et al. [167] showed that the classical finite element approach for resolving the turbulent boundary near the wall gives poor results and is not recommended. Lehmkuhl et al. [115] improved the classical FE approach by adapting the implementation of the classical finite volume and finite difference method where the LES mesh extends to the wall. This adapted method can be equivalent to the wall-stress model, which shows better results. Figure 3.2 shows the difference between classical FE and the adopted method.

In the present study, we use the method adopted by Owen et al. [167] and Reichardt's extended law of the wall [182] as a wall function.

$$u^+ = \frac{1}{\kappa}\ln(1+\kappa y^+) + 7.8(1 - e^{-\frac{y^+}{11}} - \frac{y^+}{11}e^{-0.33y^+}), \tag{3.12}$$

where $u^+ = \frac{\overline{u}}{u_\tau}$ is the dimensionless velocity, $y^+ = \frac{yu_\tau}{\nu}$ is the dimensionless wall distance, $u_\tau = \sqrt{\frac{\tau_w}{\rho}}$ is the friction velocity, τ_w is the wall shear stress, ν is the kinematic viscosity and $\kappa = 0.41$ is the von Kárman constant.

CHAPTER 4
NUMERICAL SETUP

In this chapter, the setup of numerical experiments is described. We validate numerical code against two experimental studies in Section 4.1. Next, we modify our setup in order to accommodate multiple cylinders, which are modeled as trees representing emergent plants with rounded stems. To reduce the computational cost, we scale down the tsunami and tree parameters using non-dimensional parameters, which are described in Section 4.2. Since our study relies on the investigation of tsunami flow energy damping performance, we adopt a reduction in energy flux as a metric of tsunami energy attenuation. Therefore, we calculate energy flux reflection and dissipation, which is described in Section 4.3.

4.1 Model Validation

We select two experimental analyses to validate the numerical model. We use Benchmark I mainly to validate our simple dam break computation without any obstacles. We choose Benchmark II to assess our model in the presence of obstacles. We also use Benchmark II to justify the grid size employed in other simulations since we use the same setup from the experimental analysis in Benchmark II and conduct our numerical studies for multi-cylinder configurations.

4.1.1 Benchmark I

Martin and Moyce [144] executed a comprehensive set of measurements to characterize the dynamics of a collapsing liquid column on a rigid horizontal plane. We use the experimental data to validate our flow solver in the absence of obstacles. The choice of Benchmark I is well suited to validate a numerical model because, as observed by Martin and Moyce [144], the measurements were not influenced by either viscosity

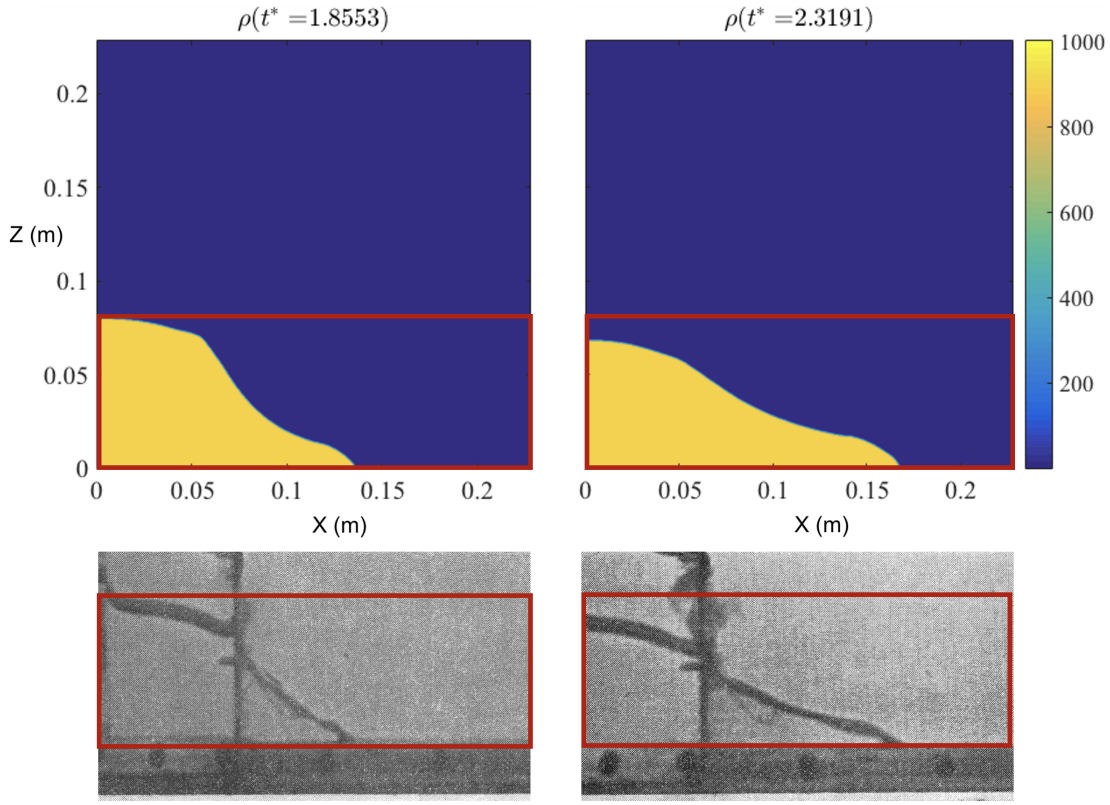

Figure 4.1 Benchmark I: Qualitative comparison of the numerical results of the collapsing column against the lab photographs of Martin and Moyce [144].

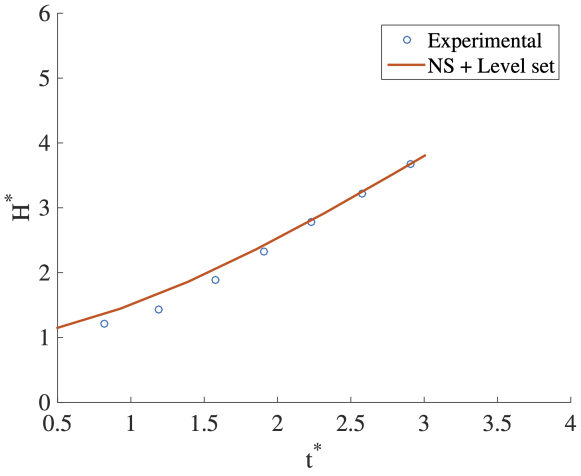

Figure 4.2 Benchmark I: Computed front position against the measurements by Martin and Moyce [144].

or surface tension. As a consequence, they can be generalized across scales for both viscous and inviscid flows. The experimental setup consists of a water column, where a is the initial depth of the water column and the initial horizontal distance of the water column from the upstream wall. To compare the numerical results against the measurements, we define the following non-dimensional quantities:

$$\begin{aligned} H^* &= z/a, \\ t^* &= t\sqrt{g/a}, \end{aligned} \tag{4.1}$$

where z is the distance of the bore front from the upstream wall. In the current configuration, $a = 0.05715\,\text{m}$. We compare the time evolution of the collapsing column at $t^* = 1.8553$ and $t^* = 2.3191$ in Figure 4.1 against the experiments by Martin and Moyce [144]. Figure 4.2 shows the quantitative comparison of the front position versus the non-dimensional time. In Figure 4.2, the time axis starts at $t^* = 0.5$ because the experimental data is available only from $t^* = 0.5$. As per Equation 4.1, the dimensional time t is 0.038 s at $t^* = 0.5$, which is the time gap between dam column collapse and recording data caused due to limitation of the experimental setup.

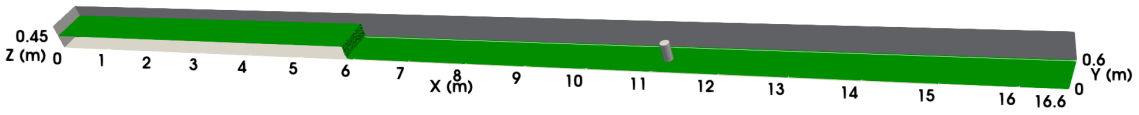

Figure 4.3 Benchmark II: Schematic illustration of numerical testing flume with a cylinder for model validation used in the physical experiment by Arnason et al. [2]

4.1.2 Benchmark II

For Benchmark II, we compare the output of our code against the experimental data of Arnason et al. [2]. As sketched in Figure 4.3, flow is generated by the opening of a gate that releases a column of water with an initial depth of 0.25 m. The collapsing water column forms a bore that flows downstream over a uniform, thin water layer

with a depth of 0.02 m and around a cylinder located at $X = 11.1$ m. The diameter of the cylinder is 0.14 m. The initial water column in the upstream region is separated from the downstream water by the gate, which is situated at 5.9 m from the upstream wall. The domain used in the experiment is 16.6 m long, 0.6 m wide, and 0.45 m deep.

We conduct our tests for two different grid resolutions. Table 4.1 shows how the grid setups differ for fine as compared to coarse resolution. We compare the evolution of the water depth for the fine and coarse grid along the streamwise direction from the cylinder leading edge in Figure 4.4. In the coarse grid setup, the maximum bore depth at the cylinder leading edge reaches around 0.225 m at 3.6 s. In comparison, Arnason et al. [2] reported a maximum bore depth of 0.27 m at 3.5 s. Our computation underestimates the water depth at this coarse grid resolution and is unable to capture the water level rise after the bore impact due to numerical dissipation.

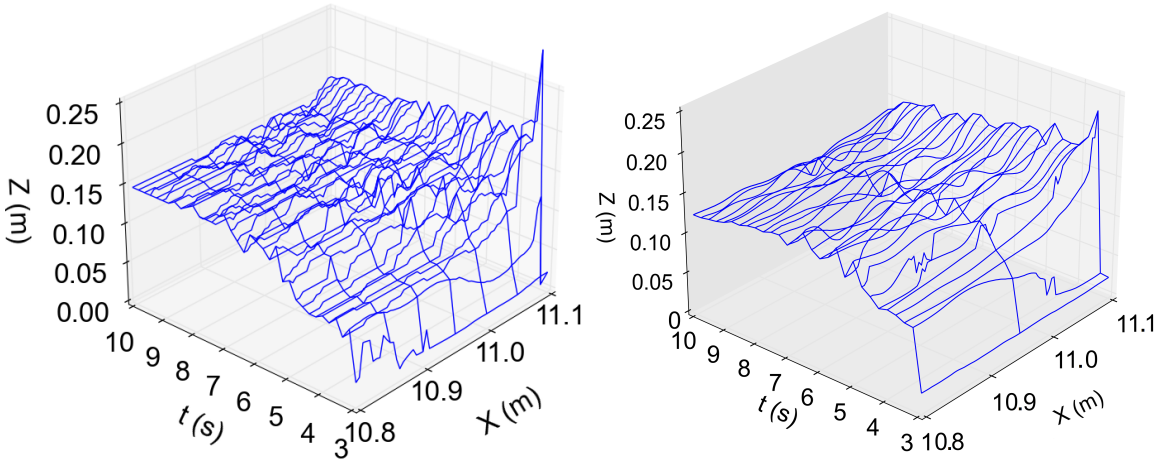

Figure 4.4 Comparison of the evolution of water surface elevation along the streamwise direction from the cylinder leading edge. Left: Fine mesh scheme. Right: Coarse mesh scheme.

In the fine grid resolution setup, the bore hits the cylinder at 3 s, and the water level increases at the cylinder leading edge due to reflection. The bore reaches a maximum of 0.268 m at 3.5 s, closer to the maximum water level observed in the experimental study than for coarse grid resolution.

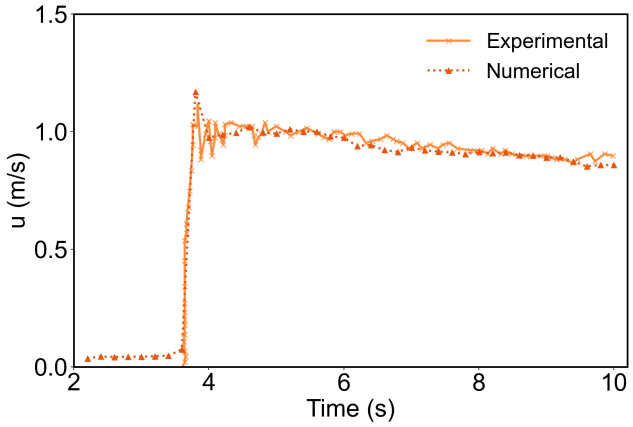

Figure 4.5 Comparison of the time evolution of velocity magnitude at $X = 11.1\,\mathrm{m}$.

Arnason et al. [2] also conducted an experimental analysis without the cylinder and recorded the depth-averaged velocity at $X = 11.1\,\mathrm{m}$. We simulate the flow without the cylinder for the fine grid size of $0.0075\,\mathrm{m}$ as shown in Table 4.1. We then compare the time evolution of depth-averaged velocity against the experimental data. Figure 4.5 shows the comparison between the numerical and experimental data. Before the bore arrival ($t = 2 - 3.7\,\mathrm{s}$) at $X = 11.1\,\mathrm{m}$, a negligible discrepancy of velocity exists between numerical analysis and laboratory experiment. The free-surface evolution is more error-prone because of the drastic change in flow velocity during column collapse. Once the bore reaches the cylinder upstream of the wall, the numerical result approaches the average position of the velocity-time curve of the experiment.

4.2 Numerical Experiments

We carry out numerical experiments for different vegetation parameters such as elastic moduli, diameters, and stem spacing to identify how the presence of tree trunks alters the energy fluxes. The details of the numerical flume setup, non-dimensional parameters, and energy balance calculations are described in the following sections.

Table 4.1 Comparison of Maximum Water Surface Elevation at Cylinder Upstream Edge of Numerical Study Against the Laboratory Data

Method	*Number of elements*	*Grid size (m)*	h_{max} *(m)*
Experiment	-	-	0.27
Numerical: Coarse grid resolution	2×10^6	0.025	0.22
Numerical: Fine grid resolution	12×10^6	0.0075	0.268

4.2.1 Size of the numerical flume

We modify our numerical setup used to validate our simulations against the experimental results by Arnason et al. [2] to accommodate multiple cylinders in the domain along the spanwise direction. The modified testing flume is 20.6 m long, 0.8 m wide, and 0.45 m deep. The dam depth at the upstream reservoir is 0.18 m, and in the downstream region, the initial water depth is 0.02 m water depth. We increase the streamwise length of the domain to avoid wave reflection at the end wall and the domain width to minimize the blockage effect between the lateral walls and cylinders. We use the same grid setup as summarized in Table 4.1 to carry out the simulations for multi-cylinder configurations. The sketch of the numerical testing flume is shown in Figure 4.6.

4.2.2 Boundary conditions

The lateral, left, right, and top walls are assigned a no-flux boundary condition with free slip. We apply a no-slip boundary condition at the cylinder wall and at the bottom surface through the wall-modeled LES approach described in Section 3.4.2.

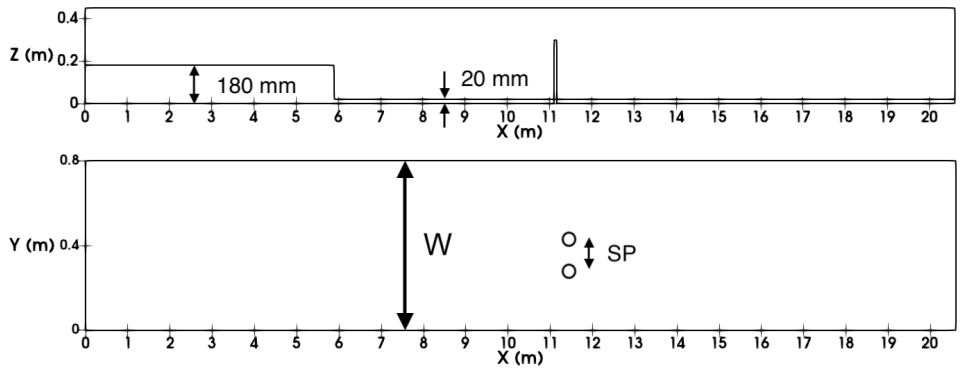

Figure 4.6 Schematic illustration of numerical testing flume used for multiple cylinder configurations with cylindrical columns. Top: XZ plane (front view) of the flume showing the dam depth at the upstream and downstream regions. Bottom: XY plane (top view) of the flume and SP corresponds to the center-to-center distance between the cylinders, and W is the width of the domain.

4.2.3 Scaled parameters of tsunami bore generation

The onshore height of a tsunami bore can vary from 2 m to 15 m based on the tsunami intensity scale [e.g., 78–80, 82, 83]. In this study, we only consider small to intermediate wave heights to reduce the computational cost. Since the grid size of the numerical model needs to be sufficiently small to capture the small-scale eddies, the computational cost increases dramatically with the scale difference between eddies and tsunami height. To simulate tsunami propagation, we scale down the computational model using the scale factor $SF = 1 : 60$. A tsunami bore height of 4.5 m, inferred for the Indian Ocean tsunami by Lavigne et al. [114], then corresponds to span-averaged bore height h_{avg} of 0.075 m in the scaled simulations. Following the method presented by Arnason et al. [2], we estimate the initial dam depth as 0.18 m based on the onshore tsunami depth in the scaled simulations.

Table 4.2 Scaled Tsunami Parameters in the Simulations

Tsunami parameters	*Real scale parameters*	*Scaled model parameters*
Onshore bore depth: h_{avg} (m)	4.5	0.075
Onshore bore velocity: u_{avg} (m/s)	7.9	1.02
Vegetation diameter: D (m)	$0.4 - 1$	$0.035 - 0.14$
Vegetation Height: H (m)	15	0.4
Modulus of elasticity: E (Pa)	$10^8 - 10^{10}$	$10^4 - 10^6$
Non-dimensional modulus of elasticity: $E^* = E/\rho_f u_{avg}^2$	$3 \times 10^3 - 3 \times 10^5$	$20 - 2 \times 10^3$
Froude Number: $Fr = u_{avg}/\sqrt{gh_{avg}}$	1.2	1.2
Reynolds Number: $Re_h = \frac{u_{avg} h_{avg}}{\nu}$	26×10^6	5.6×10^4

Our approach to scaling ensures that the Froude number is approximately the same in a field setting as in our scaled simulations. We also define the Reynolds number, Re_h, and both non-dimensional parameters, Fr and Re_h, are calculated based on the characteristic length h_{avg} to ensure consistency in our scaling used, defined as follows.

$$Fr = u_{avg}/\sqrt{gh_{avg}}, \quad Re_h = \frac{u_{avg}h_{avg}}{\nu},$$

where h_{avg} and v_{avg} are the span-averaged bore depth, and velocity, respectively, and ν corresponds to the kinematic viscosity of water, which is $10^{-6}\,\mathrm{m}^2/\mathrm{s}$. When the bore reaches $X = 11.1\,\mathrm{m}$ at $t = 4\,\mathrm{s}$. This location corresponds to the cylinder location when the cylinders are present, but we evaluate h_{avg} and v_{avg} for the case without cylinders to compute Fr and Re_h. The reason is that we do not see significant changes in average bore depth along the streamwise direction when no cylinder is present. The quantities h_{avg} and v_{avg} describe the bore as it propagates on a flat surface. Our non-dimensional numbers hence target the scales characterizing the incoming bore before it interacts with the cylinders.

We prioritize scale similarity in the Froude number because it is an important parameter for onshore tsunami propagation and other free-surface flows, particularly where hydraulic jumps occur [28, 63]. A tsunami generally flows inland as a super-critical flow characterized by $Fr > 1$. Different studies proposed different ranges of Froude numbers. For example, Kawata et al. [93] suggested a range of $0.7 - 2$ for the Froude number based on field surveys conducted for past tsunamis. Similarly, a study by Foytong et al. [48] found Froude numbers between 1 and 1.5. Informed by these estimates, we use $Fr = 1.2$ for all simulations, calculated based on the tsunami inflow condition before impact on the cylinders. We keep the inflow condition the same for all simulations, implying that Fr is the same for all cases (see Table 4.2).

The main drawback of ensuring scale-similarity in the Froude number is that the Reynolds number in our simulations is lower than it would typically be in the field. The Re_h is 5.6×10^4 for scaled model as compared to $> 10^6$ on the field. The difference is certainly significant, but Re can vary enormously in the field and changes during the inundation as the flow loses energy. In the scaled simulation, the initial bore depth is the same for all configurations, resulting in the same value of Re_h for all configurations. We present the vegetation parameters such as vegetation diameter, height, and modulus of elasticity for scaled and non-scaled simulations in Table 4.2. The choice of those parameters is described in detail in Section 4.2.4.

Table 4.3 List of Non-dimensional Parameters

Non-dimensional parameters	*Values considered*
Vegetation flow parameter: $VFP = \frac{E^* IBD}{\rho_r h_{avg} H^3 SP^2}$	$90 - 225$
Roughness density: $\lambda_f = aH$	$0.28 - 2$
Vegetal parameter: $VP = \frac{BD}{SP^2}$	$1.4 - 5.7$
Solid volume fraction: $\phi = \frac{\pi}{4} aD$	$0.2 - 0.35$

4.2.4 Different parameters of multiple cylinder configurations

We model trees as cylinders following Nepf [160], who also approximated emergent plants with rounded stems as circular base cylinders. To incorporate the tree parameters into the cylinders, we choose the properties of hardwoods such as pine, oak, and maple trees. The diameters of trees in the coastal forest can vary depending on the canopy height and age. Based on the study by Bingham and Sawyer [17], and Tanaka [207], we choose a range of diameters between $0.4-1$ m and a trunk height, H, of 15 m. Since we intend to study the effect of different trunk diameters on the energy budget, we keep the trunk height constant for all the scenarios. According to the field

investigation conducted by Pasha et al. [170], Rodríguez et al. [185] coastal forests can be dense, intermediate, and sparse based on the SP/D ratio (SP is the gap between the trees along a cross-stream direction and D is the diameter), which can vary from $1.1 - 5$. In this study, we mainly use dense and intermediate arrangements where SP/D is 1.5 and 2. To study how trunk's stiffness affects the energy balance, we choose Young's modulus E, which is approximately $10^8 - 10^{10}$ Pa [59] for hardwoods.

Since we scale down the tsunami flow parameters, the tree parameters must be scaled down as well. The main challenge is to scale the modulus of elasticity so that the deflection of cylinders will be correctly captured. Scaling the modulus of elasticity using the scale factor $SF = 1 : 60$ may not be correct because, apart from the modulus of elasticity, rigidity also depends on the moment of inertia. Since we are using the multi-cylinder configuration for different diameters and once the diameter increases, rigidity also increases, instead of scaling the modulus of elasticity directly, we scale down the flexural rigidity EI. A similar approach was implemented by Lakshmanan et al. [110], where rigidity was scaled using a non-dimensional vegetation flow parameter VFP expressed as

$$VFP \equiv \left(\frac{E^* IWD}{\rho_r h_{avg} H^3 SP^2} \right), \tag{4.2}$$

where H is the tree height, $I = \pi D^4/4$ is the moment of inertia, W is the bed width, SP is the center to center distance between the cylinders, $E^* = E/\rho_f u_{avg}^2$ is the non-dimensional modulus of elasticity, $\rho_r = \rho_s/\rho_f$, ρ_s is the tree trunk density which is $500\,\mathrm{kg/m^3}$ and ρ_f is the fluid density ($1000\,\mathrm{kg/m^3}$).

We choose hardwood trees such as pine as a reference point for our scaling. First, we calculate VFP based on the field parameters reported in Table 4.2 with the range of VFP shown in Table 4.3. Then, the scaled dimensional modulus of elasticity of the model can be calculated as

Table 4.4 Configuration Details of Cylinder Parameters in Scaled Simulations

Vegetation configurations	*One cylinder*	*Two-cylinder*		*Four-cylinder*	
		$SP/D = 1.5$	$SP/D = 2$	$SP/D = 1.5$	$SP/D = 2$
Diameter (D) (m)	0.14	0.07		0.035	
SP (m)	-	0.105	0.14	0.0525	0.07
ϕ	-	0.35	0.14	0.35	0.07
λ	-	1	0.2	2	0.2
$A_b = n\pi D^2/4\,(\mathrm{m}^2)$	0.0154	0.00384		0.0019	
Scaled modulus of elasticity (Pa)	$1 \times 10^5, 5 \times 10^4, 1 \times 10^4$	$5 \times 10^5, 1 \times 10^5, 5 \times 10^4$		$5 \times 10^6, 1 \times 10^6, 5 \times 10^5$	
Maximum deflection (m)	0.01	0.02		0.05	

$$E_s = \frac{h_{s_{avg}} H_s^3 u_{s_{avg}}^2 SP_s^2}{I_s W_s D_s} VFP_{real-scale}\,, \tag{4.3}$$

where subscript s refers to the scaled parameters. According to Equation (4.3), the modulus of elasticity is then in the range of $0.01 - 1\,\text{GPa}$ and the diameters are in the range of $0.035 - 0.1\,\text{m}$ for the three different configurations in Table 4.4.

We choose three different sets of diameters and vary the number of cylinders in such a way that the cumulative diameter of all cylinders remains the same. We set the diameter of a single diameter to 0.14m and reduce the trunk diameter for multiple cylinders by cylinder number. For example, the trunk diameter for four cylinders is $0.14/4 = 0.035\,\text{m}$ (see Table 4.4). However, the flow blockage area, which is defined as $A_b = n\pi D^2/4$ where n is the number of cylinders, is different for each cylinder configuration. We vary the gap between the cylinders to investigate how the spacing between the cylinders will affect the energy reflection and dissipation. We use three different moduli of elasticity for each cylinder configuration. We choose the scaled modules of elasticity based on the range of VFP parameter mentioned in Table 4.3

In addition to VFP, we also have to scale the forest density, as reviewed by Nepf [160].Assuming fully emergent vegetation, the non-dimensional measure of the forest density is the solid volume fraction [see 237].

$$\phi = \frac{\pi}{4} aD,$$

where $a = D/SP^2$ is the frontal area per canopy volume for a given diameter D, and SP is the average distance between two consecutive stems. The parameters a and ϕ vary as a function of the tree diameter and spacing between the trunks. We vary the gap between the cylinders to investigate how the spacing between the cylinders will affect the energy reflection and dissipation. We use two cases of different cylinder gaps, $SP/D = 1.5$ and $SP/D = 2$, which gives a range of ϕ presented in

Table 4.3. If we consider the tree height instead of the diameter, the non-dimensional canopy density is represented by the roughness density, which is defined as $\lambda_f = aH$, where H is the canopy height. The range of both parameters is shown in Table 4.3. For each set of cylinder gaps, the solid volume fraction is constant in multi-cylinder configurations, whereas the roughness density varies as the diameter of the cylinders changes. Table 4.4 shows the solid volume fraction and roughness density for each configuration. As reported by Mazda et al. [153], ϕ can reach up to 0.45 for dense mangrove forests. In the current configurations, since we are using pine forests as reference tree parameters, the value of ϕ should be lower than for mangrove forests. In our study, the solid volume fraction ranges from 0.2 to 0.35.

4.3 Energy Flux

The energy flux at a particular location gives information about how much energy is available for mixing and transport [133]. To quantify the protective benefits of tsunami mitigation, we calculate the energy flux at different streamwise locations [128, 229]. We take the dot product of $\mathbf{u}$ with the momentum equation and multiply the continuity equation by gz, and sum them up as described in Venayagamoorthy and Fringer [228]. The kinetic and the potential component of the flux are then given by

$$\mathbf{k_f} = \mathbf{u}q, \quad \mathbf{p_f} = \mathbf{u}gz, \tag{4.4}$$

where $q = \mathbf{u} \cdot \mathbf{u}/2$ is the kinetic energy per unit mass. We only consider the kinetic and potential components because we do not observe noticeable differences in energy flux from the pressure term. Since we aim to investigate the energy budget along the flow or streamwise direction, we calculate the depth-integrated energy flux and then again integrate along the spanwise direction.

We then normalize the depth and the span-integrated energy flux by the width of the domain so that the energy flux will only vary along the horizontal direction. We write:

$$\mathbf{F_k} = \frac{\int_0^Y \int_0^H \mathbf{k_f}\, dy\, dz}{W}, \quad \mathbf{F_p} = \frac{\int_0^Y \int_0^H \mathbf{p_f}\, dy\, dz}{W}, \tag{4.5}$$

where H is the water depth, W is the width of the domain (see Figure 4.6), and F_K and F_p are, respectively, the depth and span-integrated kinetic and potential energy flux. Since the depth and span-integrated energy fluxes vary along the horizontal direction, we refer to them more simply as "horizontal energy fluxes". As the flow is transient, we calculate the cumulative time-integrated fluxes as shown below.

$$\begin{aligned} \mathbf{F_{k_t}} = \int_0^t \mathbf{F_k}\, dt, \quad \mathbf{F_{p_t}} = \int_0^t \mathbf{F_p}\, dt, \\ \mathbf{F_t} = \mathbf{F_{k_t}} + \mathbf{F_{p_t}}, \end{aligned} \tag{4.6}$$

where $\mathbf{F_t}$ is cumulative time-integrated total energy flux.

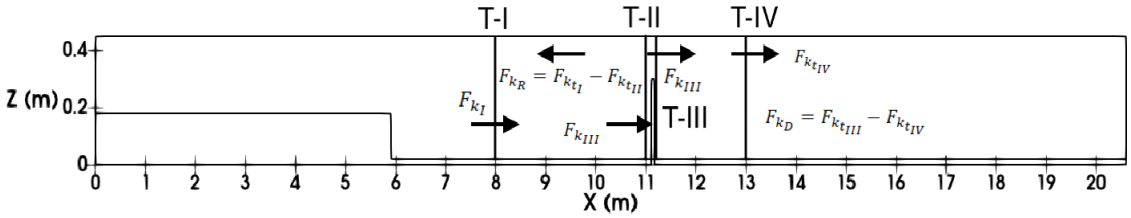

Figure 4.7 Location of transects at different streamwise locations for calculation of energy flux.

We take two transects in the streamwise direction to calculate the reflected horizontal energy flux. Transect T-I is taken at $X = 8\,\mathrm{m}$ whereas another transect T-II is closer to the cylinder leading edge at $X = 11\,\mathrm{m}$ (see Figure 4.7). If there is any reflection, the energy flux will be reduced at T-I due to the reflected wave arrival. We integrate the horizontal energy flux over the flow period (see Equation (4.6)) at T-I and T-II to identify reflection, where the flow period corresponds to the time interval between the bore arrival at the transect and end wall. Finally, we calculate

the reflected cumulative horizontal energy flux by taking the difference between the cumulative horizontal energy flux at T-I and T-II.

$$\mathbf{F}^{\mathbf{k}}_{\mathbf{R}} = \mathbf{F}_{\mathbf{k}_{\mathbf{t_I}}} - \mathbf{F}_{\mathbf{k}_{\mathbf{t_{II}}}}, \quad \mathbf{F}^{\mathbf{p}}_{\mathbf{R}} = \mathbf{F}_{\mathbf{p}_{\mathbf{t_I}}} - \mathbf{F}_{\mathbf{p}_{\mathbf{t_{II}}}}, \tag{4.7}$$

where $\mathbf{F}^{\mathbf{k}}_{\mathbf{R}}$ and $\mathbf{F}^{\mathbf{p}}_{\mathbf{R}}$ are the reflected cumulative horizontal kinetic and potential energy flux, respectively. To compare how much energy is lost due to reflection with respect to the incoming energy flux, we obtain the reflected energy flux coefficient by normalizing kinetic and potential energy flux by the cumulative time-integrated total horizontal energy flux at T-I, which is calculated as:

$$\phi^{\mathbf{k}}_{\mathbf{R}} = \frac{\mathbf{F}^{\mathbf{k}}_{\mathbf{R}}}{\mathbf{F}_{t_I}}, \quad \phi^{\mathbf{p}}_{\mathbf{R}} = \frac{\mathbf{F}^{\mathbf{p}}_{\mathbf{R}}}{\mathbf{F}_{t_I}}, \tag{4.8}$$

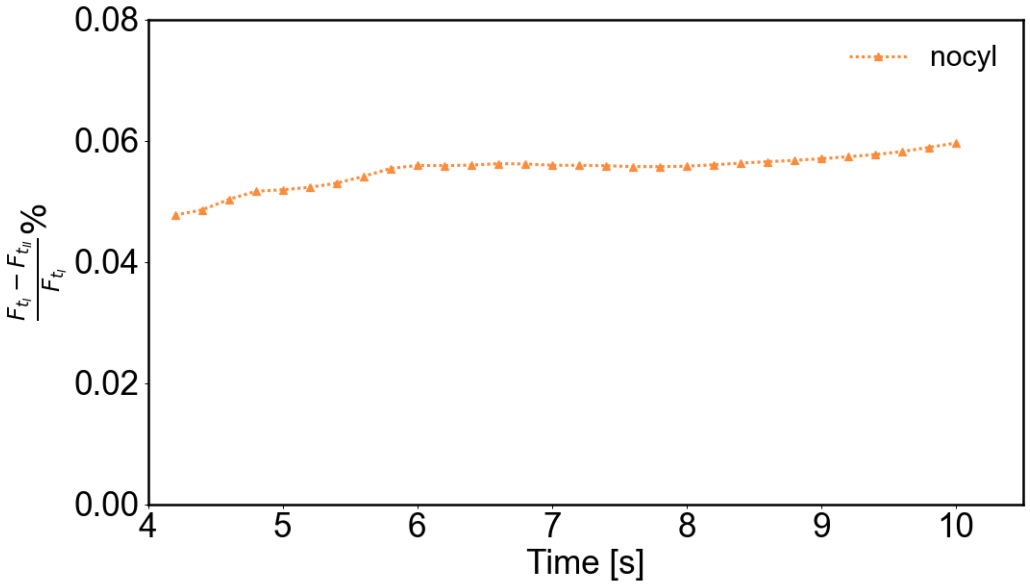

Figure 4.8 The percentage of energy lost between T-I and T-II for "without cylinder."

NOTE: While traveling from section I to section II, the bore loses its energy due to dissipation. To check whether the energy lost due to dissipation has a significant effect on energy reflection, we first conduct our simulation without the cylinder to compute how much energy is dissipated between sections I and II (see Figure 4.8). As

we can see from figure 4.8, the amount of energy flux lost due to dissipation is very small. Only 0.06% of energy is dissipated between section I and section II. Therefore, energy dissipation has a negligible effect on energy flux reflection calculation.

For energy flux dissipation, we calculate the cumulative horizontal energy flux at T-III, which is located behind the cylinder trailing edge, and at T-IV, located at 2 m from the cylinder trailing edge (see Figure 4.7). To calculate the dissipation, we choose a separate transect T-III because once the bore hits the cylinder and the reflected wave passes through T-II, the energy lost between T-II and T-IV will not identify the energy lost due to dissipation only. We thus choose a separate section at the cylinder trailing edge (T-III) to identify the dissipation. We then calculate the dissipated cumulative horizontal energy flux by subtracting the cumulative energy flux at the T-III and T-IV, as shown below.

$$\mathbf{F_D^k} = \mathbf{F_{k_{t_{III}}}} - \mathbf{F_{k_{t_{IV}}}}, \quad \mathbf{F_D^p} = \mathbf{F_{p_{t_{III}}}} - \mathbf{F_{p_{t_{IV}}}}, \tag{4.9}$$

where $\mathbf{F^{k_D}}$ and $\mathbf{F^{k_D}}$ are the cumulative dissipated kinetic and potential energy flux, respectively. Similarly, we define the energy flux dissipation coefficient as:

$$\phi_{\mathbf{D}}^{\mathbf{k}} = \frac{\mathbf{F_D^k}}{\mathbf{F_{t_{III}}}}, \quad \phi_{\mathbf{D}}^{\mathbf{p}} = \frac{\mathbf{F_D^p}}{\mathbf{F_{t_{III}}}}, \tag{4.10}$$

Since the bore generated in the wet bed reaches the transects (T-I, T-II, T-III, T-IV) located at different streamwise locations at different times, it is important to apply the time shift while calculating the energy flux difference between the transects. In the present simulation, the bore passes through the T-I (located at $X = 8\,\mathrm{m}$) at $t = 3.4\,\mathrm{s}$ and reaches T-II at $t = 4\,\mathrm{s}$. To compare and calculate the cumulative energy flux difference, we apply the time shift to the T-I to synchronize the bore arrival time with T-II. We implement the time shift in T-III and T-IV as well to calculate the

energy dissipation. Table 4.5 summarizes the energy flux parameters calculated in this study.

Table 4.5 List of Different Energy Flux Parameters

Energy flux coefficients	*Reflected and dissipated energy flux*	*Kinetic and potential energy flux*
$\phi_{\mathbf{R}}^{\mathbf{k}} = \frac{\mathbf{F}_{\mathbf{R}}^{\mathbf{k}}}{\mathbf{F}_{t_I}}$	$\mathbf{F}_{\mathbf{R}}^{\mathbf{k}} = \mathbf{F}_{\mathbf{k_{t_I}}} - \mathbf{F}_{\mathbf{k_{t_{II}}}}$	$\mathbf{F}_{\mathbf{k_t}} = \int_0^t \frac{\int_0^Y \int_0^H \mathbf{u} q \, dy \, dz}{W} \, dt$
$\phi_{\mathbf{R}}^{\mathbf{p}} = \frac{\mathbf{F}_{\mathbf{R}}^{\mathbf{p}}}{\mathbf{F}_{t_I}}$	$\mathbf{F}_{\mathbf{R}}^{\mathbf{p}} = \mathbf{F}_{\mathbf{p_{t_I}}} - \mathbf{F}_{\mathbf{p_{t_{II}}}}$	$\mathbf{F}_{\mathbf{p_t}} = \int_0^t \frac{\int_0^Y \int_0^H \mathbf{u} g z \, dy \, dz}{W} \, dt$
$\phi_{\mathbf{D}}^{\mathbf{k}} = \frac{\mathbf{F}_{\mathbf{D}}^{\mathbf{k}}}{\mathbf{F}_{t_{III}}}$	$\mathbf{F}_{\mathbf{D}}^{\mathbf{k}} = \mathbf{F}_{\mathbf{k_{t_{III}}}} - \mathbf{F}_{\mathbf{k_{t_{IV}}}}$	$\mathbf{F}_{\mathbf{k_t}} = \int_0^t \frac{\int_0^Y \int_0^H \mathbf{u} q \, dy \, dz}{W} \, dt$
$\phi_{\mathbf{R}}^{\mathbf{p}} = \frac{\mathbf{F}_{\mathbf{R}}^{\mathbf{p}}}{\mathbf{F}_{t_I}}$	$\mathbf{F}_{\mathbf{R}}^{\mathbf{p}} = \mathbf{F}_{\mathbf{p_{t_I}}} - \mathbf{F}_{\mathbf{p_{t_{II}}}}$	$\mathbf{F}_{\mathbf{p_t}} = \int_0^t \frac{\int_0^Y \int_0^H \mathbf{u} g z \, dy \, dz}{W} \, dt$
$\phi_{\mathbf{D}}^{\mathbf{p}} = \frac{\mathbf{F}_{\mathbf{D}}^{\mathbf{p}}}{\mathbf{F}_{t_{III}}}$	$\mathbf{F}_{\mathbf{D}}^{\mathbf{p}} = \mathbf{F}_{\mathbf{p_{t_{III}}}} - \mathbf{F}_{\mathbf{p_{t_{IV}}}}$	$\mathbf{F}_{\mathbf{p_t}} = \int_0^t \frac{\int_0^Y \int_0^H \mathbf{u} g z \, dy \, dz}{\int_0^Y dy} \, dt$

CHAPTER 5

RESULTS

In this chapter, we present our findings in terms of energy flux reflection and dissipation coefficient as described in Section 4.3 for different cylinder parameters. Section 5.1 and 5.2 describe the effect of rigidity in energy reflection for single and multi-cylinder configurations. We also show the water surface profile evolution at the cylinder upstream edge to compare the wave reflection for different cylinder gaps in section 5.3. Section 5.4 and 5.5 describe the effect of bendability and multi-cylinder configuration in energy flux dissipation and turbulent kinetic energy reduction.

5.1 Rigidity Enhances Energy Reflection for a Single Cylinder

Energy reflection is one of the primary means of attenuating tsunami waves [128]. When the bore hits the cylinder, part of its energy is reflected. To identify the reflection, we show the free surface profile at different flow times for one cylinder in Figure 5.1. At $t = 4\,\mathrm{s}$, the bore front reaches the cylinder upstream face with a bore depth of approximately $0.075\,\mathrm{m}$. As the bore continues to propagate, the bore depth at the cylinder's upstream face continues to increase due to flow blockage and reaches a maximum of $0.14\,\mathrm{m}$ before reflection begins. At the downstream side, the split flow joins and begins to form a turbulent wake, whereas the reflected wave flattens out towards the sides of the flume and continues to propagate back upstream (see Figure 5.1b).

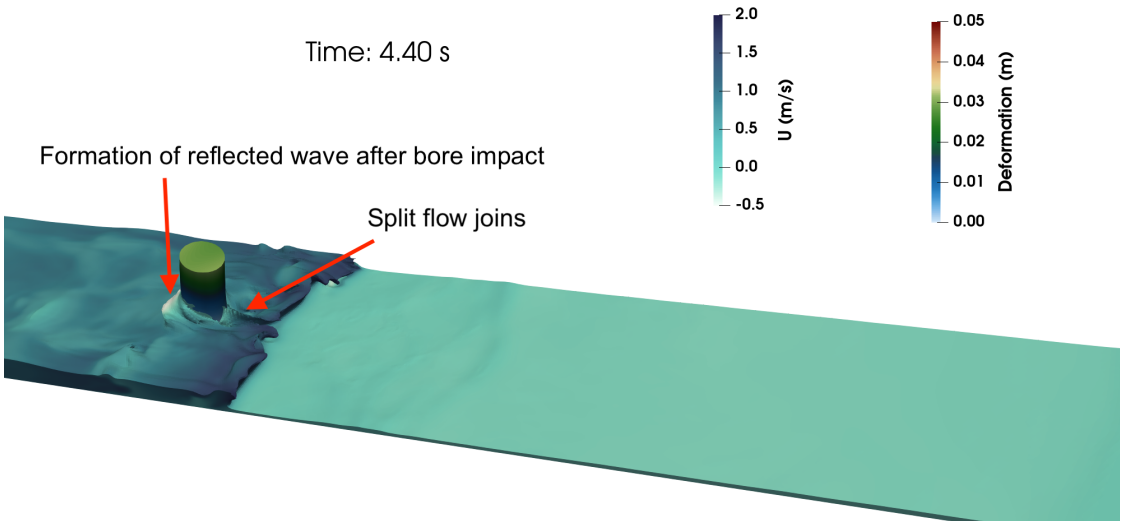

(a) One cylinder: $D = 0.14\,\mathrm{m}$, $E = 1 \times 10^4\,\mathrm{Pa}$

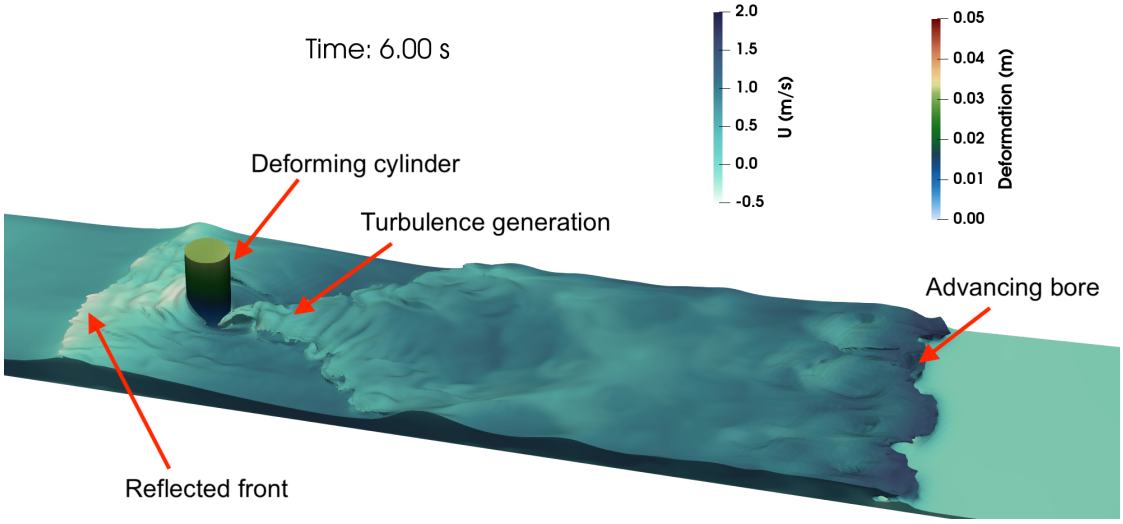

(b) One cylinder: $D = 0.14\,\mathrm{m}$, $E = 1 \times 10^4\,\mathrm{Pa}$

Figure 5.1 Velocity profile and cylinder displacement of one-cylinder configuration for $E = 1 \times 10^4\,\mathrm{Pa}$ at different flow time. (a) The flow structures when the cylinders show the maximum deflection. (b) The velocity profile and cylinder displacement when the bore wave flows further downstream.

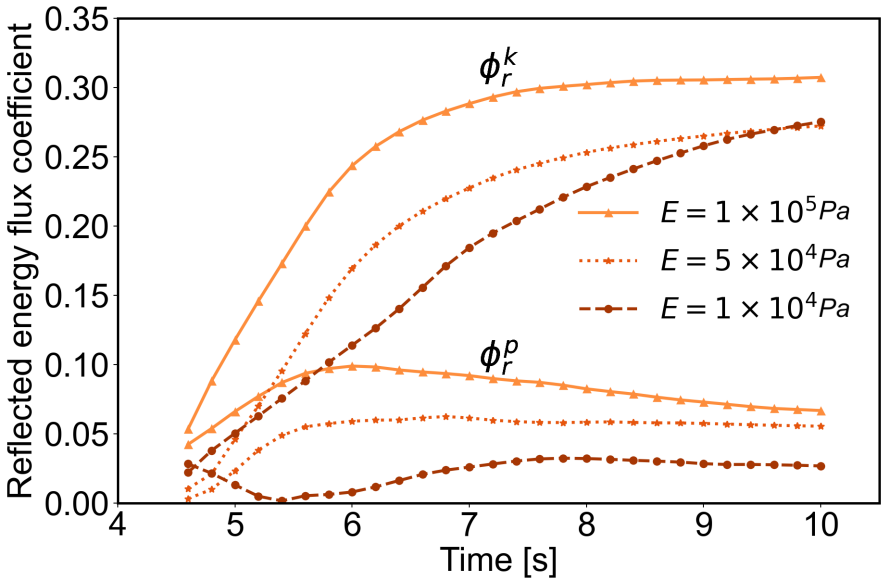

Figure 5.2 The time evolution of energy reflection flux coefficient of one cylinder for different elastic moduli and constant $Re_h = 2.8 \times 10^4$. ϕ_R^k: Reflected kinetic energy flux coefficient. ϕ_R^p: Reflected potential energy flux coefficient.

To quantify energy reflection, we calculate the energy flux reflection coefficients as described in Section 4.3. To study how reflection varies with vegetation properties, we compute the reflected energy flux coefficients for different elastic moduli. Figure 5.2 shows the comparison of the reflected energy flux coefficient of cylinders with three different moduli of elasticity defined in Section 4.2.4. Notice that deformation increases for decreasing values of the elasticity modulus. As shown in Figure 5.2, the energy reflection flux coefficient increases sharply after the bore impact ($t = 4.4 - 7\,\mathrm{s}$). During the later stages of bore propagation ($t = 8 - 10\,\mathrm{s}$), the reflection flux coefficient becomes almost constant. For all three moduli of elasticity, the reflected potential energy flux is 4 to 5 times smaller than the reflected kinetic energy flux, indicating that the reflection of kinetic energy mainly contributes to the total energy reflection.

As stated in Section 4.3, the reflected energy flux coefficient is calculated based on the cumulative time-integrated reflected energy flux, which means that the slope of the reflected energy flux coefficient shown in Figures 5.2 indicates the rate of change of reflected energy over the flow period. During the initial bore impact and

propagation ($t = 4.4 - 7\,\mathrm{s}$), the slope of the curve of reflected kinetic energy flux coefficient becomes steeper for the cylinder with the highest modulus of elasticity than with the lowest modulus of elasticity, indicating that the amount of reflected energy increases as rigidity increases. As the bore propagates further downstream, the gradient of reflected kinetic energy flux coefficient becomes constant at higher rigidity. However, at the lowest modulus of elasticity, the gradient still increases (see Figure 5.2) for $t = 8 - 10\,\mathrm{s}$. Since the rigid cylinder deforms less after the bore impact but also rebounds less with a negligible deflection after the passage of the bore front, the reflected energy is higher during the initial bore impact and becomes constant quickly. On the other hand, flexible cylinder deforms more by the hydrodynamic forces exerted on them and hence reflects less energy. Nevertheless, the flexible cylinder also rebounds more compared to the rigid one, resulting in a continuous increase of reflected energy during the later phase of flow propagation ($t = 8 - 10\,\mathrm{s}$).

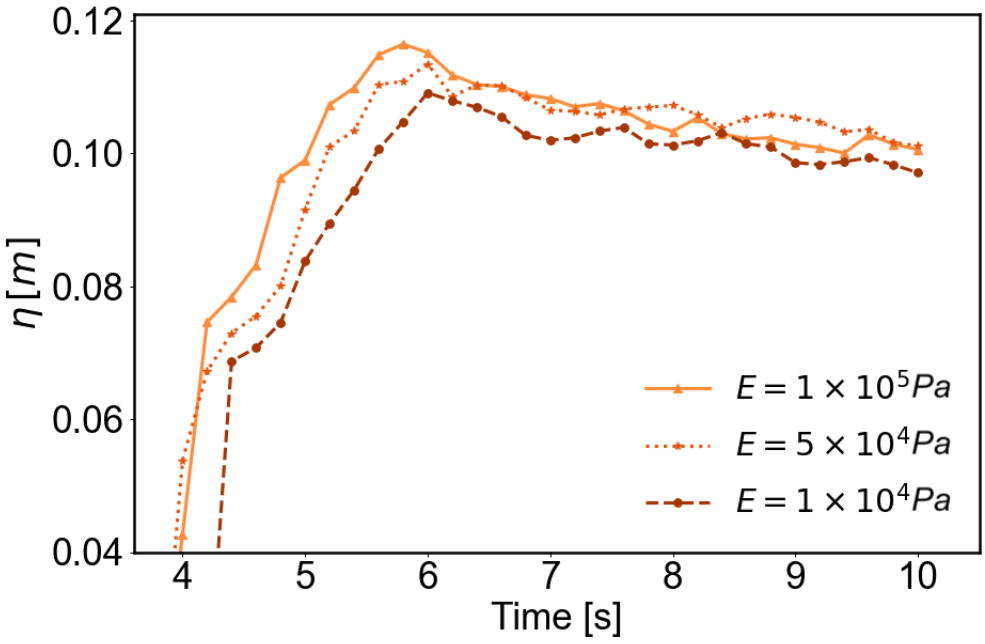

Figure 5.3 The time evolution of water surface at transect II for different elastic moduli in one cylinder.

The reflected potential energy flux coefficient is consistent with the evolution of the reflected kinetic energy flux coefficient. In figure 5.2 we find the gradient of reflected potential energy flux coefficient is steeper at the highest rigidity, but during the later phase of flow, the gradient declines for all cases, although the slope declines more rapidly as the rigidity increases. Since rigidity triggers reflection, the bore depth increases at the upstream face of the cylinder. This finding is supported by the average water surface evolution at the cylinder upstream edge location at different elastic moduli shown in Figure 5.3. Since the potential energy flux depends on the water depth, rigidity-induced water elevation increases the potential energy flux.

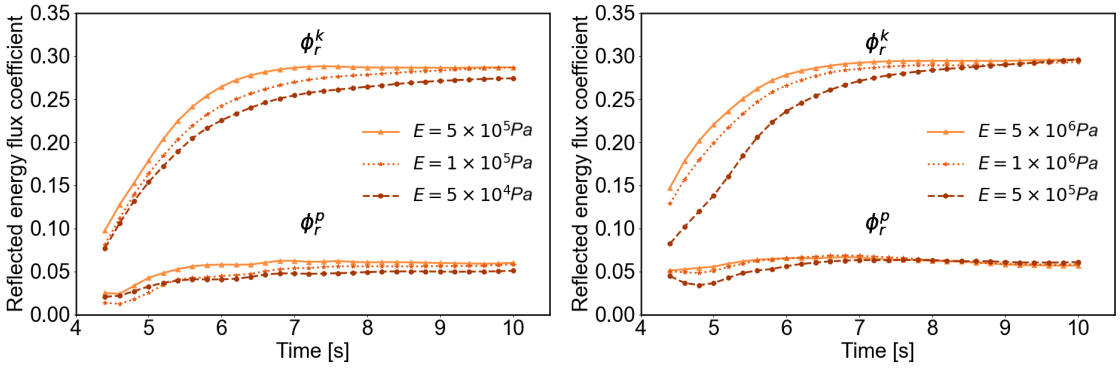

(a) Two cylinders, $SP/D = 1.5$ (b) Four cylinders, $SP/D = 1.5$

Figure 5.4 The time evolution of energy reflection flux coefficient (reflected kinetic and potential energy flux coefficients) of two-cylinder and four-cylinder configuration for different elastic moduli and at $Re_h = 2.8 \times 10^4$.

5.2 Reflective Effect of Rigidity Is Lost for Multiple Cylinders

Rigidity is not the only parameter affecting onshore energy flux; the number of cylinders and the cylinder spacing also alter the flow field sensitively and hence the energy flux. Interestingly, our simulations show that the dependency of reflected energy on the rigidity is most pronounced for the single cylinder shown in Figure 5.2. The equivalent results for multiple cylinders are summarized in Figures 5.4a and 5.4b. In Table 5.1, we compare the percentage of maximum reflected kinetic energy flux during the time period 4 - 8 s for one cylinder to the two and four-cylinder configu-

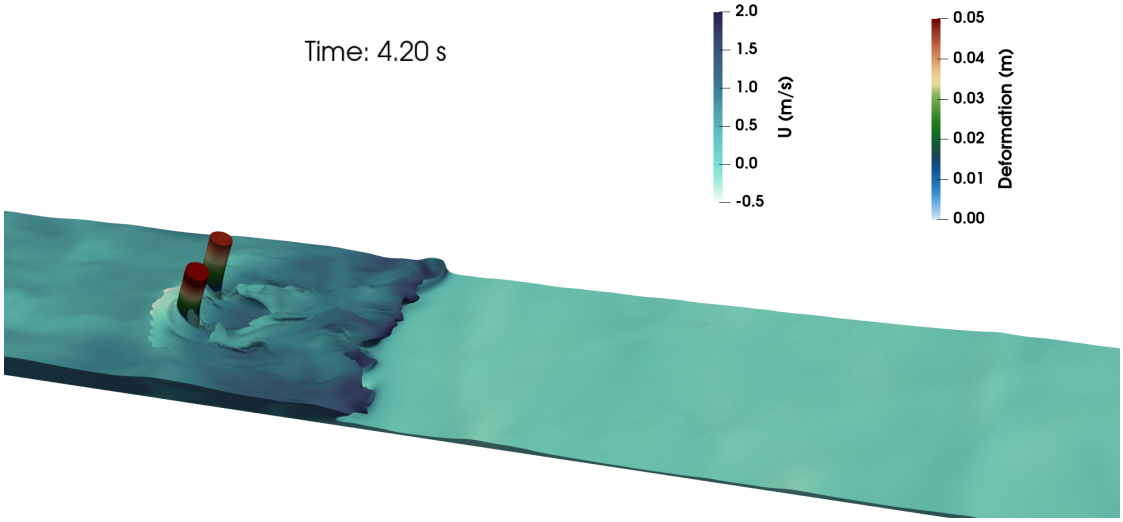

(a) Two cylinders: $D = 0.07\,\text{m}$, $E = 5 \times 10^4\,\text{Pa}$

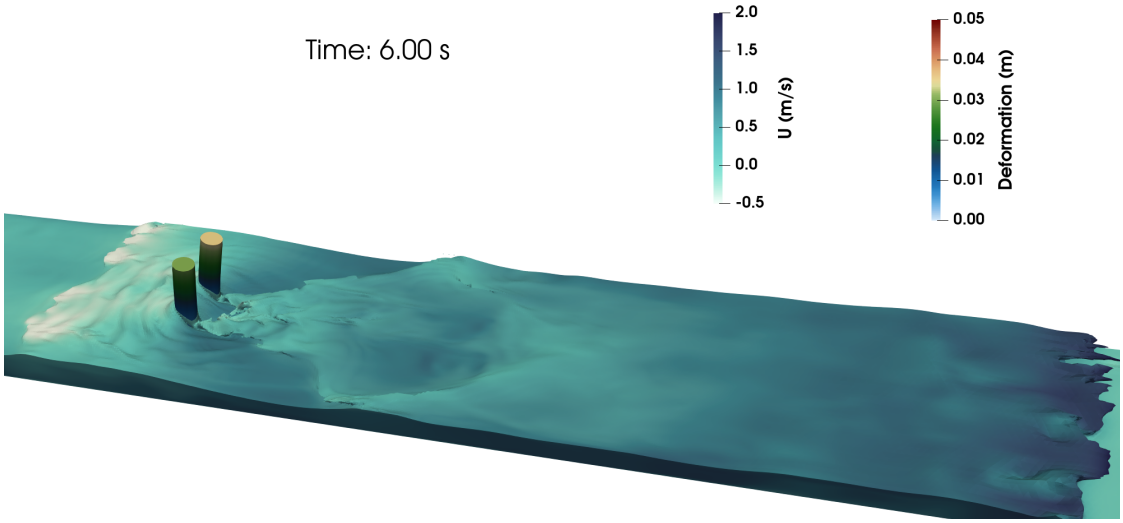

(b) Two cylinders: $D = 0.07\,\text{m}$, $E = 5 \times 10^4\,\text{Pa}$, $SP/D = 2$

Figure 5.5 Velocity profile and cylinder displacement of two-cylinder configuration at $SP/D = 2$ at different flow times.

rations at two different spacings. The maximum difference in reflected kinetic energy flux for single cylinders with different rigidities is around 4.6%. In a two-cylinder arrangement, this difference decreases to 2%. In a four-cylinder arrangement, this difference further decreases to 1%, suggesting that the effect of rigidity on the reflected kinetic energy flux becomes negligible as the number of cylinders increases.

In a multiple-cylinder configuration, the blockage area (see Table 4.4) along the spanwise direction is split into smaller areas. The flow can propagate through the gap between the cylinders, leading to a different flow field with multiple wakes. Figures 5.5 and 5.6 show two snapshots of the flow around two cylinders and four cylinders at the time of maximum deflection and after the passage of the bore front, respectively. At $t = 4.2\,\mathrm{s}$ after bore impact, the increase in water depth at the cylinders' upstream faces is clearly visible for two cylinders. The interactions between the four cylinders are apparent, particularly in Figure 5.6, where the split flow around each one of the cylinders joins into one wake that is reminiscent of the wake behind a single cylinder in Figure 5.1 (b).

For four cylinders, these flow-field interactions become even more pronounced, as shown in Figure 5.6. In this configuration, the cylinders no longer deform in unison because of the dynamic feedback between deflection and flow. In figure 5.6a only the second cylinder from the upper side deflects primarily in the flow direction while the cylinder closest to the lower side of the domain bends partially outwards to accommodate flow in the gap between the cylinders. As a consequence, the reflected wave front in the four-cylinder configuration does not increase in depth but instead flattens out along the spanwise direction. However, the total blockage area of two cylinders is twice of four cylinders, which explains why increasing the number of split regions between the cylinders reduces the energy reflection.

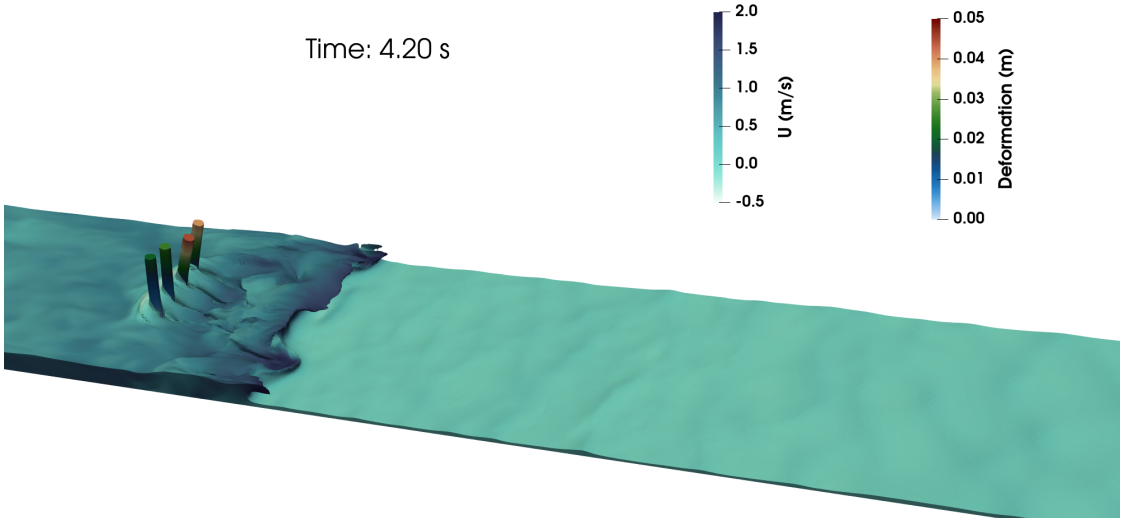

(a) Four cylinders: $D = 0.035\,\text{m}$, $E = 5 \times 10^5\,\text{Pa}$

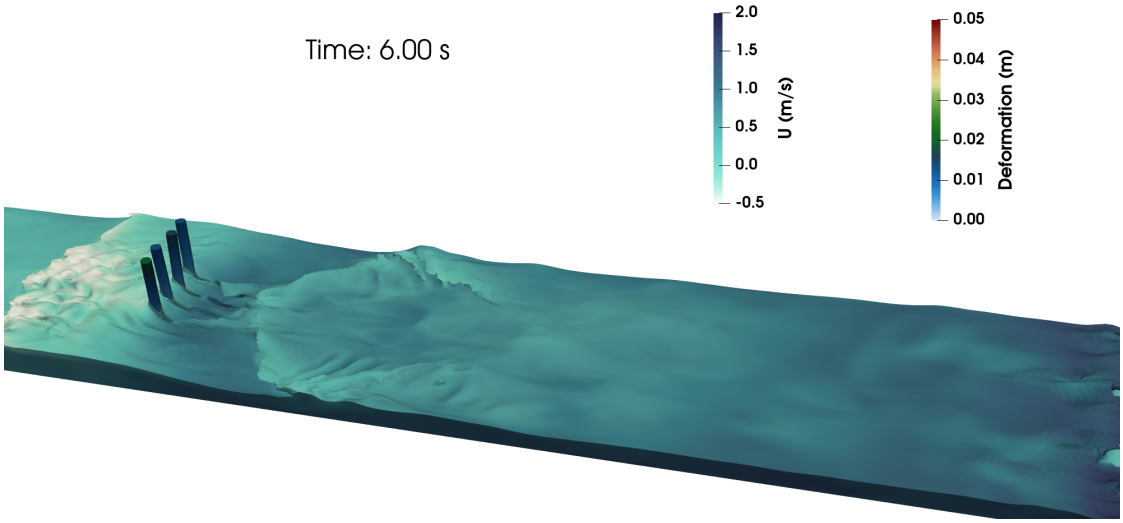

(b) Four cylinders: $D = 0.035\,\text{m}$, $E = 5 \times 10^5\,\text{Pa}$

Figure 5.6 Velocity profile and cylinder displacement of four-cylinder configuration at $SP/D = 2$ at different flow times.

The dynamic feedback between cylinder deformation and flow characteristics induces a complex relationship between cylinder spacing and energy flux reflection. Our simulations demonstrate that the gap between the cylinders alters flow restriction and modifies the energy flux reflection, but the difference between different configurations with the same number of cylinders is relatively small. The blockage area of cylinders is the same at $SP/D = 1.5$ and $SP/D = 2$; as the gaps are widened, the cylinders are shifting towards the sidewall, which explains why increasing the gap does not change significantly the energy reflection. As shown in Table 5.1, the difference between $SP/D = 1.5$ and $SP/D = 2$ in energy flux reflection is 0.3% for two-cylinder and 0.2% for four-cylinder configurations and hence negligible for practical purposes. Since the blockage area of a two-cylinder configuration is two times that of a four-cylinder configuration, the cylinders with a higher blockage area cause slightly higher reflection in closely spaced cylinders.

Table 5.1 Percentage of Maximum Reflected Kinetic Energy Flux for Different Cylinder Configurations

$\phi^k_{R_t\,max}\%$					
Modulus of elasticity (E)	*One cylinder* ($D = 0.14\,\mathrm{m}$)	*Two-cylinder* ($D = 0.07\,\mathrm{m}$)		*Four-cylinder* ($D = 0.035\,\mathrm{m}$)	
		$SP/D = 1.5$	$SP/D = 2$	$SP/D = 1.5$	$SP/D = 2$
$1 \times 10^4\,\mathrm{Pa}$	27.2%	-	-	-	
$5 \times 10^4\,\mathrm{Pa}$	27.6%	27.4%	27%	-	
$1 \times 10^5\,\mathrm{Pa}$	30.8%	28.31%	28.3%	-	
$5 \times 10^5\,\mathrm{Pa}$	-	29.1%	28.8%	28.9%	27.5%
$1 \times 10^6\,\mathrm{Pa}$	-	-	-	28.95%	28.12%
$5 \times 10^6\,\mathrm{Pa}$	-	-	-	29%	28.85%

The percentage of reflected kinetic energy flux lies between $25 - 30\%$ for all configurations, whereas the amount of maximum potential energy flux reflection is $4 - 5$ times smaller than the kinetic energy flux reflection. The reflected potential energy flux shows the same pattern as kinetic energy flux, where the importance of rigidity is lost when the number of cylinders increases. Since potential energy flux depends on the water depth at the cylinder upstream edge (transect II, see Figure 4.7), the comparison of water depth evolution for different elastic moduli is shown for multi-cylinder arrangement in Figure 5.7 to verify our findings. Since the difference in energy flux reflection at $SP/D = 1.5$ and at $SP/D = 2$ is minimal (see Table 5.1), the water surface evolution for different rigidities is shown only at $SP/D = 1.5$. Also, the difference in wave height for different rigidities at the cylinder upstream edge becomes minimal in a two and four-cylinder arrangement, indicating that the increment in wave reflection due to rigidity is negligible in multi-cylinder configurations.

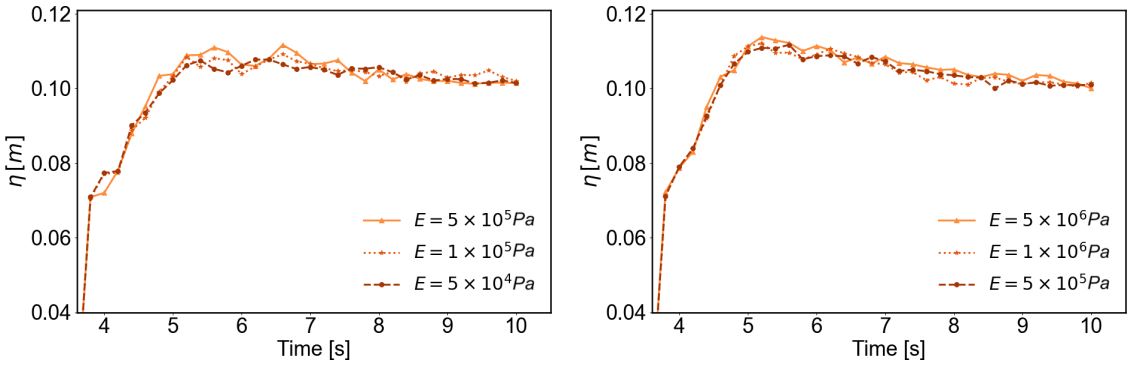

(a) Two cylinders, $SP/D = 1.5$ (b) Four cylinders, $SP/D = 1.5$

Figure 5.7 The time evolution of water surface at transect II for different cylinder arrangements and elastic moduli.

5.3 Flow Blockage Area Enhances Wave Reflection

In this study, we define three different cylinder configurations, each cylinder configuration has a different flow blockage area. The flow blockage area in a one-cylinder is two times higher than in a two-cylinder and four times higher than in a four-cylinder

configuration. As shown in Table 5.1, the one-cylinder with the highest flow blockage causes more flow restriction than multiple cylinders, resulting in the maximum amount of energy reflection. To compare the wave reflection for all cylinder arrangements, the spanwise-averaged free-surface evolution for different cylinder arrangements at transect T-II ($X = 11\,\mathrm{m}$) is shown in Figure 5.8. Without the cylinders, the bore maintains a constant depth over the flow period. The bore depth increases when cylinders are present, indicating the water level rise due to flow blockage, which causes the reflection of the wave. The reflected bore depth is highest in one cylinder with a higher flow blockage area and higher in closely spaced cylinders.

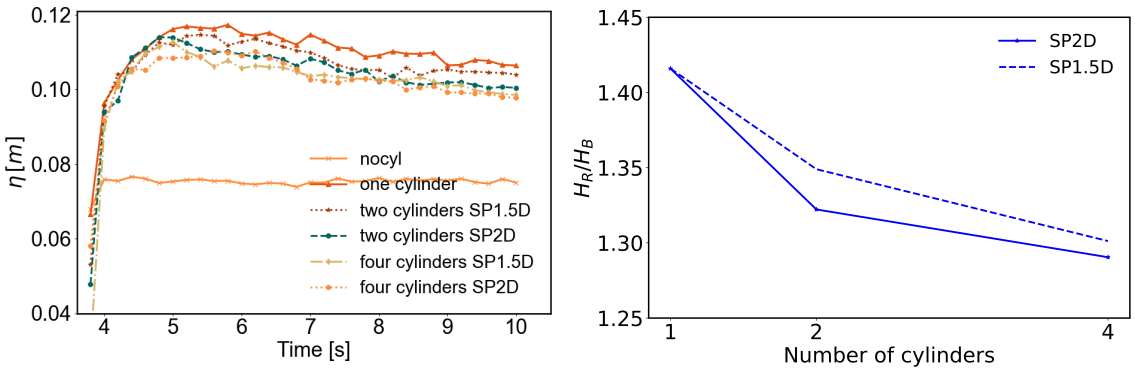

Figure 5.8 Time evolution of water surface profile and reflection index for different cylinder arrangements at $X = 11\,\mathrm{m}$. Left: comparison of water surface profile. Right: Reflection index for different cylinder parameters.

To compare the wave reflection for different cylinder configurations, we measure the maximum reflected bore depth H_R by taking the maximum value of wave height over the flow period. We define the incident bore depth in the absence of cylinders as the maximum bore depth (see Figure 5.8). Finally, we obtain the reflection index by taking the ratio of H_R and H_B and compare it for different cylinder configurations. A similar approach was implemented by Oshnack et al. [166] to calculate the reflection index of tsunami bore to study the influence of different onshore seawalls on tsunami wave attenuation.

From the reflection index shown in Figure 5.8, we conclude that the reflection of the wave follows the same pattern as the energy flux reflection variation in different cylinder arrangements. As expected, the reflection index in one cylinder with a larger diameter is the highest among the other configurations, whereas the four-cylinder with a larger gap at $SP/D = 2$ has the minimum reflection index. The percentage of reflection for different cylinder configurations is also shown in Table 5.2. The smaller gap between the cylinders is beneficial in terms of the reflection because cylinders with a smaller gap produce more flow blockage. Nevertheless, when the number of cylinders is increased to four, the effect of closely spaced cylinders in flow blockage becomes negligible. The percentage of wave reflection for four cylinders with a small gap of $SP/D = 1.5$ is only 1% higher than for four cylinders with a gap of $SP/D = 2$.

Table 5.2 Percentage of Wave Reflection for Different Cylinder Configurations

Percentage of reflection	*one cylinder*	*Two-cylinder* $SP/D = 1.5$	*Two-cylinder* $SP/D = 2$	*Four-cylinder* $SP/D = 1.5$	*Four-cylinder* $SP/D = 2$
$(\frac{H_R - H_B}{H_B})\%$	41.5%	35.5%	32%	31%	30%

5.4 Rigidity Reduces Flow Damping and Turbulent Kinetic Energy in the Downstream Region

So far, our analysis has focused on how the presence of trees may increase energy reflection, but reflection is not the only physical mechanism that contributes to reducing the energy carried onshore by a tsunami. Energy dissipation also reduces the energy flux associated with the tsunami and is an important parameter for assessing the protective benefit afforded by different vegetation configurations in tsunami mitigation. In the wake region, rigidity controls not only the motion of the cylinder body but also the flow structures around it. Since not all cylinders move

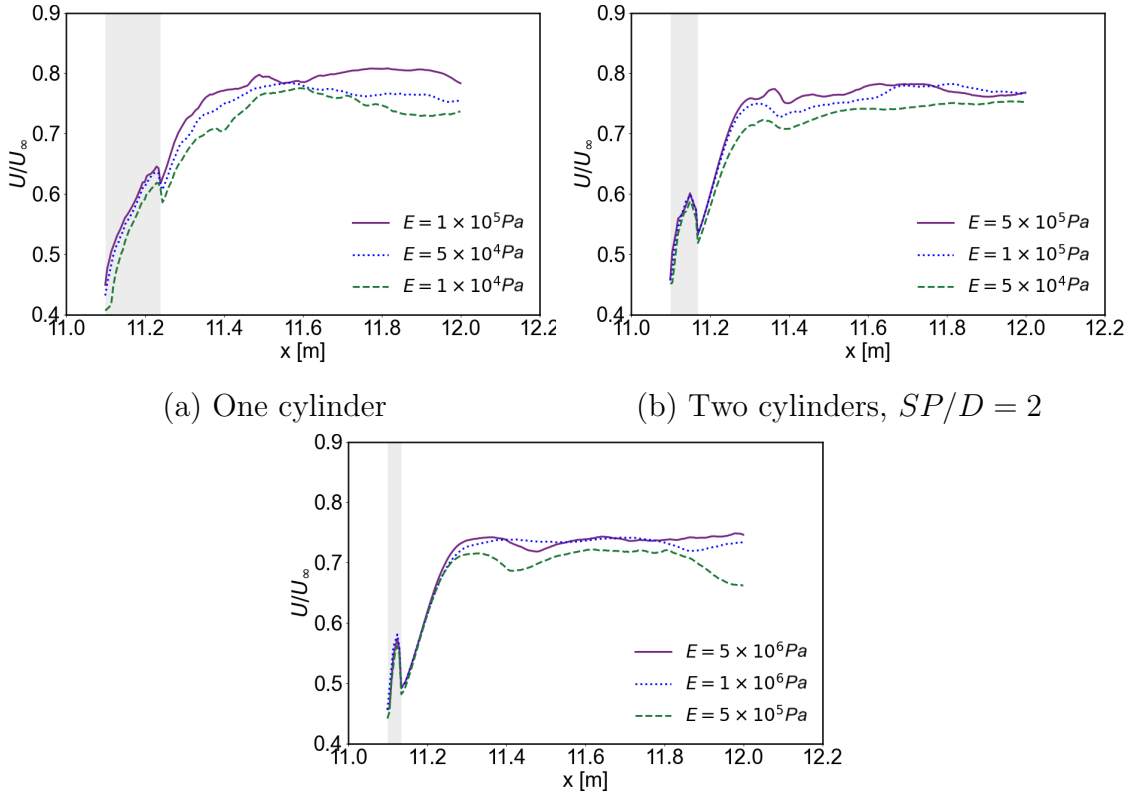

(a) One cylinder

(b) Two cylinders, $SP/D = 2$

(c) Four cylinders, $SP/D = 2$

Figure 5.9 The normalized longitudinal velocity profile along the streamwise direction for multi-cylinder configurations.

uniformly, the dynamic response between the flow and the cylinder bodies makes the flow structure more complex, which affects the flow velocity and hence alters dissipation.

To understand the effect of rigidity in the wake region, we show the longitudinally averaged velocity profile along the streamwise direction in Figure 5.9. The velocity is averaged along the depth and spanwise direction. The field-averaged velocity is then further averaged over the flow period after the bore has reached the downstream region. Here, the flow period is 4 s which is the time interval between the bore arrival at the downstream region and the end wall (see Figures 5.1, 5.5 and 5.6). We normalize the computed velocity by the approach speed U_∞, defined as the velocity of the bore before hitting the cylinders, to compare how the longitudinal velocity changes along the wake region with respect to the approach velocity. As shown in Figure 5.9, the averaged velocity is lower than the approach speed at the upstream edge of the cylinders. Once the bore flows past the cylinders, the flow decelerates, and the flow energy is reduced due to reflection.

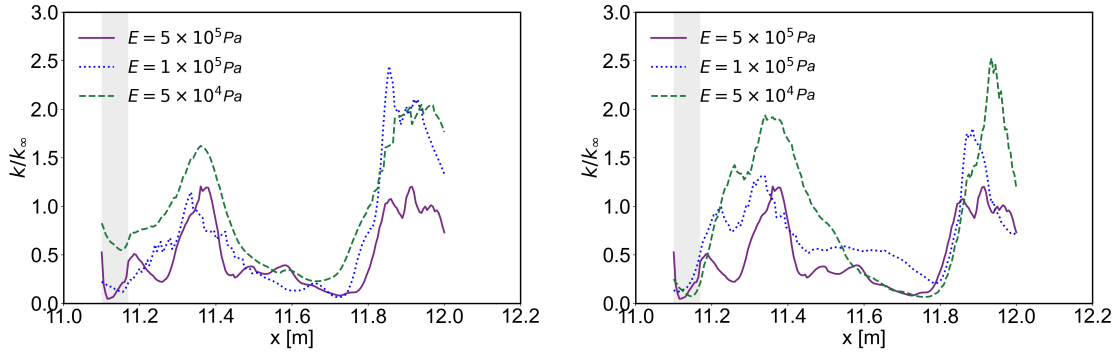

(a) Two cylinders, $SP/D = 1.5$ (b) Two cylinders, $SP/D = 2$

Figure 5.10 The instantaneous longitudinal distributions of normalized turbulent kinetic energy along the streamwise direction for two-cylinder configuration at $t =$ 6 s. The turbulent kinetic energy has two peaks, one behind cylinders due to flow separation and the other at the further downstream region where split flow joins.

In the flow separation region, the normalized velocity steadily increases from 0.42 and maintains a constant value further downstream. Lower rigidity entails more

velocity reduction in the wake region because the cylinders deform more, increasing their interaction with the flow field. The normalized velocity is reduced by 15% at the streamwise location $X = 11.4 - 12\,\mathrm{m}$. At the farthest downstream region ($X = 11.8 - 12\,\mathrm{m}$), the normalized velocity is reduced by around 20% at a modulus of elasticity $E = 5 \times 10^5\,\mathrm{Pa}$ in the four-cylinder arrangement, indicating that cylinder deflection alters the flow structure. As the number of cylinders increases, multiple processes contribute to the change in the flow, reducing the impact on the global effect of individual causes. Figure 5.9 shows the longitudinal velocity profiles at $SP/D = 2$ only because we do not observe any significant changes in normalized velocity as the gap between the cylinders changes.

The longitudinal profiles of instantaneous turbulent kinetic energy (TKE) in Figures 5.10 and 5.11 show the effect of rigidity and gap between cylinders on the reconfiguration of turbulent flow structures in the wake region of cylinders. We calculate the resolved turbulent kinetic energy per unit mass by taking averages in both the spanwise and depth direction over the resolved velocity fluctuation fields:

$$k = \frac{1}{2}(\langle u'^2 \rangle_{s,d} + \langle v'^2 \rangle_{s,d} + \langle w'^2 \rangle_{s,d}), \tag{5.1}$$

where $\langle\rangle_{s,d}$ represents the span and depth average operator. We calculate the resolved velocity fluctuation by averaging the velocity along the spanwise direction only.

$$u' = u - \langle u \rangle_s, \quad v' = v - \langle v \rangle_s, \quad w' = w - \langle w \rangle_s,$$

u', v', w' are the resolved velocity fluctuations and $\langle\rangle_s$ corresponds to the spanwise average operator. Here, we consider only the resolved component of velocity fluctuations to examine turbulent kinetic energy distribution since the subgrid turbulent kinetic energy (TKE) is one order of magnitude lower than the resolved TKE. A similar observation is made by Kim et al. [105], who studied turbulent statistics of dam break-driven flow and concluded that the resolved fluctuations mainly contribute

to producing the turbulent energy. Since LES is capable of resolving more than 1 order of magnitude of turbulent energy cascade, we do not consider the effect that unresolved fluctuations may have on TKE. Once TKE is calculated, we normalize it by k_∞ measured at $X = 11.1\,\mathrm{m}$, which is the location of the upstream cylinder edge. For all the investigated flows, we extract the normalized instantaneous field-averaged turbulent kinetic energy profile ($k/k_\infty = 1$) at $t = 6\,\mathrm{s}$, representing the scenario when the dam front wave has reached the downstream region (see Figures 5.6 and 5.5).

Figures 5.10 and 5.11 show two peaks of turbulent kinetic energy: the first peak is located behind the cylinders and is a consequence of flow separation. The second peak occurs further downstream, where the split flow joins, and a hydraulic jump occurs. For both the two-cylinder and the four-cylinder arrangements, the first peak of normalized TKE tends to become higher as the elastic modulus decreases, but the spatial variability in TKE is also high. We detect the highest first peak at $SP/D = 2$, where the normalized TKE increases by 30% at the lowest modulus of elasticity. After the first peak, a region of reduced TKE extends up to $X = 11.8\,\mathrm{m}$ for all scenarios. Between $X = 11.8\,\mathrm{m}$ and $X = 12\,\mathrm{m}$, a second peak forms, initiating a von Kaŕmań vortex street. The highest second peak arises at $SP/D = 2$ for both two and four-cylinder arrangements at the lowest modulus of elasticity. For four cylinders, the difference between TKE at $E = 5 \times 10^5\,\mathrm{Pa}$ and $E = 1 \times 10^6\,\mathrm{Pa}$ is higher at $SP/D = 2$ than at $SP/D = 1.5$. A similar pattern emerges in the two-cylinder arrangement. The reconfiguration of the cylinders alters the flow field and enhances the turbulence generation in the downstream region. Also, deflection alters the turbulent structures in the wake of cylinders, particularly at $SP/D = 2$.

5.5 Rigidity Reduces Kinetic Energy Dissipation for All Configurations

To summarize the energy dissipation afforded by the presence of cylinders in different configurations, we compute the dissipated energy flux coefficient as defined in Section

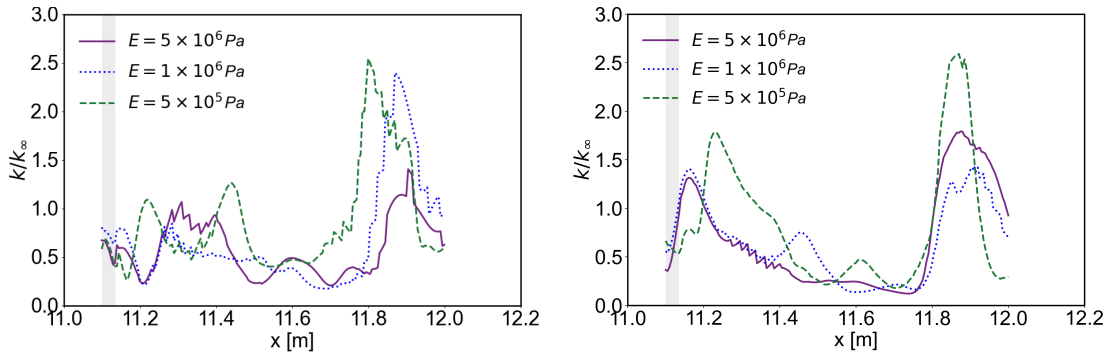

(a) Four cylinders, $SP/D = 1.5$ (b) Four cylinders, $SP/D = 2$

Figure 5.11 The longitudinal distributions of turbulent kinetic energy along the streamwise direction for four-cylinder configuration at $t = 6\,\mathrm{s}$.

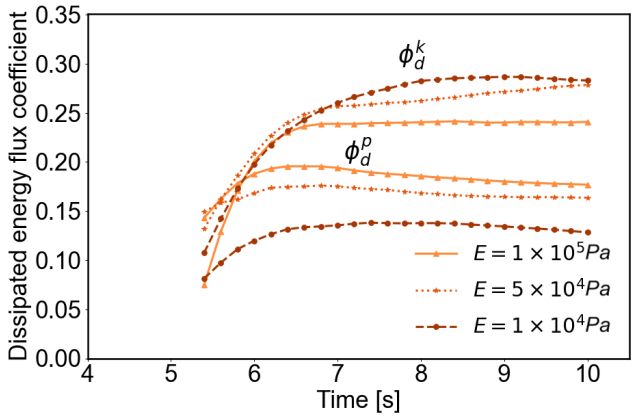

Figure 5.12 Energy dissipation flux coefficient as a function of time of one cylinder for different elastic moduli. ϕ_d^k: Dissipated kinetic energy flux coefficient. ϕ_d^p: Dissipated potential energy flux coefficient.

4.3. Figure 5.12 is the equivalent of Figure 5.2, showing the dissipated rather than the reflected energy flux coefficient for a single cylinder. It demonstrates that increasing rigidity has opposing effects on the dissipation of kinetic and potential energy fluxes: A more rigid cylinder dissipates less kinetic energy but more potential energy. The dissipated potential energy flux is around 80% of the dissipated kinetic energy flux coefficient in the one-cylinder configuration.

The opposing effect of rigidity on reflection as compared to dissipation is the consequence of deflection. Once the bore hits the cylinders, the flexible cylinder deforms more than the rigid cylinder, dissipating more kinetic energy. After the

impact of the bore front, the energy of the incoming flow is not sufficient to cause further deformation of the cylinder. Therefore, the dissipation rate of kinetic energy becomes almost constant at the later phase of the flow period ($t = 8 - 10\,\mathrm{s}$) in Figure 5.12. The rigid cylinder dissipates more potential energy flux than the flexible cylinder because the deflection of the flexible cylinder reduces build-up of the free surface and hence dissipates less potential energy flux. As a consequence, the joint effect of rigidity on the total dissipation, including both the kinetic and the potential components, is small.

Figure 5.13 shows the dissipated energy flux coefficients for both potential and kinetic energy for the configurations with multiple cylinders. The tendency of rigidity to increase the dissipation of potential energy flux remains noticeable for two-cylinders in Figures 5.13a and 5.13b, but disappears in the four-cylinder configuration (Figures 5.13c, 5.13d). In comparison, the effect of rigidity on the dissipation of kinetic energy flux remains largely robust in both the two-cylinder (Figures 5.13a and 5.13b) and the four-cylinder configurations (Figures 5.13c, 5.13d). For two cylinders, the dissipated potential energy flux decreases by 5% as rigidity decreases for two cylinders. In the four-cylinder configuration, the changes of potential energy flux are less than 1% since the changes in the depth of the transmitted wave are negligible as rigidity changes.

The reason for the reduced effect of rigidity on the dissipation of potential energy flux is that the build-up of the free surface is more sensitively affected by the presence of other cylinders than the longitudinally averaged flow velocity. In the limit of four cylinders, we find less build-up of the wave surface around the cylinders, and as a consequence, the variability of wave depth along the downstream region remains small in this limit. In addition to losing a clear relationship with rigidity, the magnitude of dissipation of potential energy flux diminishes in the presence of multiple cylinders. In the two-cylinder configuration, the dissipated potential energy

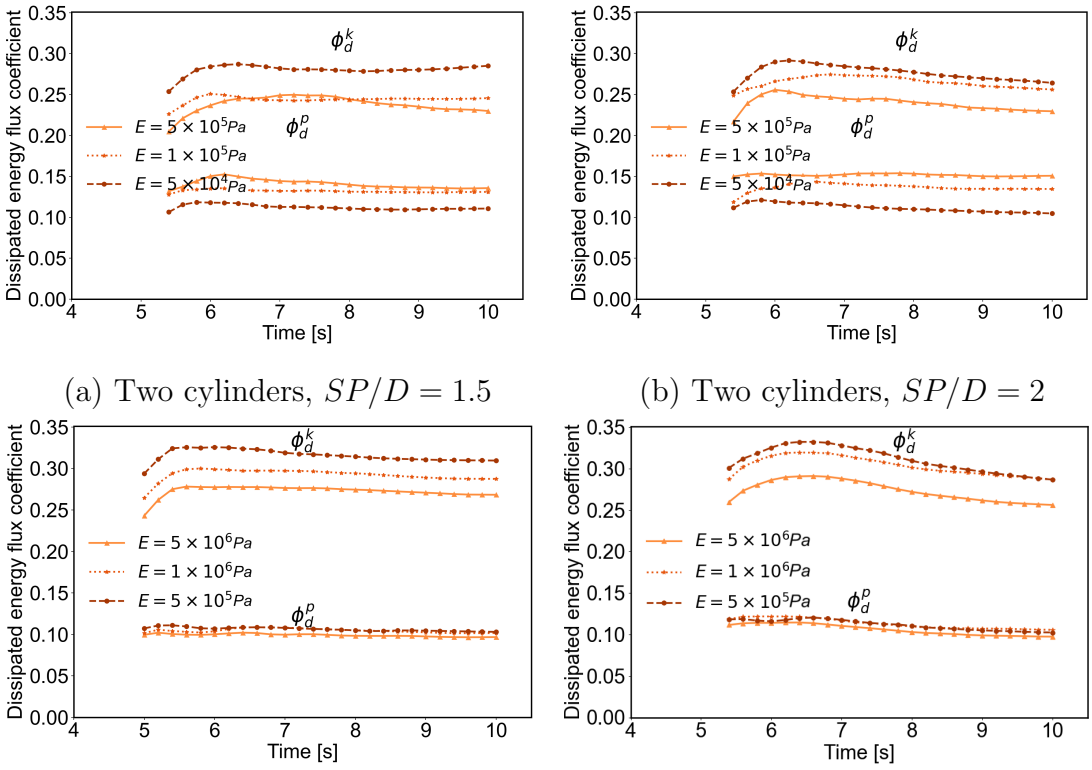

(a) Two cylinders, $SP/D = 1.5$

(b) Two cylinders, $SP/D = 2$

(c) Four cylinders, $SP/D = 1.5$

(d) Four cylinders, $SP/D = 2$

Figure 5.13 The energy dissipation flux coefficient as a function of time of two-cylinder and four-cylinder arrangement for different elastic moduli and cylinder gaps. Top row: Dissipated kinetic and potential energy flux coefficients for two-cylinder configuration. Bottom row: Dissipated kinetic and potential energy flux coefficients for four-cylinder arrangement.

flux is approximately 50% of the dissipated kinetic energy flux. When increasing the number of cylinders to four, the dissipated potential energy flux is further reduced to roughly 30% of the kinetic energy flux.

Table 5.3 Percentage of Maximum Dissipated Kinetic Energy Flux for Different Cylinder Configurations

$\phi^k_{D_t\,max}\%$					
Modulus of elasticity (E)	*One* cylinder ($D = 0.14\,\mathrm{m}$)	*Two-cylinder* ($D = 0.07\,\mathrm{m}$)		*Four-cylinder* ($D = 0.035\,\mathrm{m}$)	
		$SP/D = 1.5$	$SP/D = 2$	$SP/D = 1.5$	$SP/D = 2$
$1 \times 10^4\,\mathrm{Pa}$	28.7%	-	-	-	
$5 \times 10^4\,\mathrm{Pa}$	27.9%	28.7%	29.2%	-	
$1 \times 10^5\,\mathrm{Pa}$	24.1%	25.1%	27.5%	-	
$5 \times 10^5\,\mathrm{Pa}$	-	25%	25.6%	31%	33.2%
$1 \times 10^6\,\mathrm{Pa}$	-	-	-	28.4%	32%
$5 \times 10^6\,\mathrm{Pa}$	-	-	-	26.2%	29%

We report the percentage of maximum dissipated kinetic energy flux for different cylinder parameters in Table 5.3. For one cylinder, the percentage of the maximum dissipated kinetic energy flux coefficient is around 24% at an elastic modulus of $1 \times 10^5\,\mathrm{Pa}$, and the dissipated kinetic energy increases by 4% as the structure becomes more flexible. In the two-cylinder and four-cylinder configurations, the percentage of dissipated kinetic energy flux coefficient for the lowest modulus of elasticity steadily goes up to 33%. For both scenarios, lower rigidity induces more energy dissipation. Moreover, the difference in kinetic energy flux dissipation increases as the number of cylinders increases. In a two-cylinder configuration, the difference is 4%, whereas, in a four-cylinder, the difference becomes 5%.

This finding is also supported by the turbulent kinetic energy shown in Figures 5.10 and 5.11, which quantifies how cylinder deflection enhances the turbulent kinetic energy. The comparison shows that the energy dissipation increases with

an increasing number of cylinders. This increase is expected because increasing the number of cylinders increases the interfacial area where flow and structures are interacting and where turbulent boundary layers form. Taken together, the total energy flux dissipation tends to be highest in the four-cylinder configuration, but the difference in total dissipated energy flux is not very significant, at least not for the relatively small number of cylinders considered here.

Apart from rigidity, the gap between the cylinders also modifies energy dissipation, but minimally so. The difference in kinetic energy dissipation is $2\% - 3\%$ for all configurations. At the highest modulus of elasticity, where cylinders are almost rigid, the maximum energy dissipation obtained is approximately 2.2% higher in the four-cylinder at $SP/D = 2$ than at $SP/D = 1.5$. For most other cylinder arrangements, the difference is smaller, often less than one percent, and probably insignificant for practical purposes.

CHAPTER 6

DISCUSSION

The notion of protecting the shoreline with the help of concrete sea walls comes at a staggering price, not only in terms of the construction costs but also in terms of a detrimental effect on coastal ecosystems [e.g., 21, 42, 172] and shoreline stability [36, 106]. Less obvious than the drawbacks of lining the coast with concrete, often meter-high sea walls are the alternative, particularly along high-impact coasts like Japan or Indonesia, where tsunamis are frequent and destructive. The idea that vegetation may act as a bioshield against flooding was first proposed in the context of marshlands attenuating storm surges in southern Louisiana [e.g., 47, 227], but the wrath of a tsunami differs fundamentally from the comparatively mild tidal or seasonal flows for which vegetation is thought to be an effective bioshield [194].

An important aspect of tsunami runup is its profound dependence on both off-shore bathymetry and onshore topography [e.g., 39, 68, 116, 147, 192, 219]. While off-shore bathymetry is difficult to modify, onshore topography could be altered in a way that reduces tsunami impacts, essentially combining nature-based elements and traditional engineering elements into a hybrid approach to mitigating tsunami risk. An example of this approach is a vegetated coastal mitigation park: A landscape unit on the shoreline built specifically to protect communities or critical infrastructure and provide vertical evacuation space while strategically integrating trees or other vegetated elements to enhance protective benefit.

Prior work by Lunghino et al. [128] has characterized the protective benefit of the onshore topography created by the hillscape of coastal mitigation parks but did not explicitly consider the role of vegetation. As communities across the world increasingly consider or adopt coastal mitigation parks, it remains an open question whether the presence of forests of large trees, such as the maritime pines of Japan,

could be used to enhance the protective benefits of coastal mitigation parks and, if so, whether some species of vegetation might be more effective than others. The latter question has immediate relevance for ongoing international efforts to mitigate tsunami risks. For example, field assessments of damage associated with the 2004 Indian Ocean earthquake and tsunami have posited that Casuarina forests mitigated tsunami impacts more effectively than native ecosystems like sand dunes [145]. As a consequence, natural sand-dune ecosystems along the Coromandel Coast, India, were destroyed and replaced with *Casuarina Equisetifolia*, an exotic timber with potentially adverse ecological effects [16].

Several field assessments have argued that different species vary significantly in the protective benefits they provide, as reviewed in Cochard et al. [32]. However, many of these assessments are based on observed correlations between tsunami damage and the presence of different ecosystems [e.g., 7, 30, 34, 35, 86, 91, 165, 206, 208, 209] and stop short of identifying a possible causal relationship between vegetation and tsunami damage. A key challenge in comparing the effect of different ecosystems is that they thrive in different environments. For example, after the Indian Ocean tsunami, Chatenoux and Peduzzi [30] found that tsunami damage was reduced behind seagrass beds but increased behind coral reefs. As pointed out by the authors, an important confounding factor is a difference in the morphological settings where these ecosystems are located, with seagrass meadows growing primarily on shallow, gently-sloping continental shelves and barrier reefs lining a break in the continental slope.

In our study, we intentionally do not consider the complexities associated with the geomorphological setting and adopt a highly simplified flat topography to isolate the effect of vegetation properties. Since our objective of the study is to assess the role of onshore vegetation in tsunami risk reduction, our interest lies specifically in studying the effect of coastal forest density and the rigidity of tree trunks in tsunami energy attenuation. In Section 5.1, we show that rigidity enhances energy reflection

for a single cylinder, but the case of a single cylinder is primarily of abstract value since tree trunks rarely grow in isolation. In the practically more relevant case of multiple cylinders in Section 5.2, the difference created by variable rigidity all but disappears. Moreover, in Section 5.3, we observe that the gap between the cylinders has less effect on energy reflection as the number of cylinders increases. The additional complexity introduced into the flow field by the presence of multiple cylinders dominates over the rigidity effect, even in the idealized setup of our numerical experiments. There would be significantly more noise in an actual field setting, potentially further reducing the difference in response.

Taken together, our simulations from Sections 5.1 and 5.2 suggest that the rigidity of tree trunks is less relevant than the arrangement and density of the tree trunks within the coastal forest. An additional factor that reduces the role of rigidity is that rigidity reduces the dissipation of kinetic energy flux afforded by the presence of trees. At least for a single cylinder, rigidity hence affects the reflection and the dissipation of the onshore energy flux in opposite ways. Compared to the effect of rigidity on the reflection of kinetic energy flux, the reduction in dissipation of kinetic energy appears less sensitive to the presence of other tree trunks, as demonstrated in Section 5.4. However, the effect itself is on the order of a few percent and may hence not generalize to a field setting where many other factors confound flow behavior.

An interesting aspect of our findings in Sections 5.1 - 5.5 is that tree trunks reduce the onshore energy flux to a comparable degree through both reflection and dissipation. In contrast, the protective benefit of coastal mitigation parks lies primarily in the reflection of incoming wave energy [128]. This finding suggests that the protective benefit of tree trunks and hillscapes could complement the protective benefit of coastal mitigation parks by augmenting reflection and adding dissipation. An important caveat to this interpretation is that we only consider reversible, elastic deformation of the tree trunks and do not include tree breakage or uprooting, which

tend to be the main cause for trees increasing damage in the field [e.g., 159, 210, 222]. The breaking patterns of trees do tend to vary among different species [207, 212, 217] and also depend on trunk diameter [77, 221]. Particularly the dependence on diameter highlights the value of working with existing, native vegetation and potentially integrating it into mitigation parks rather than planting a mono-culture of trees of a particular species from scratch.

We emphasize that our work adopts a highly idealized view and does not capture sedimentation and erosion as recently reviewed in Sugawara et al. [200] that could alter the energy flux onshore [51] and affect the stability of tree trunks. Neither do we consider the role of the canopy or other vegetation that would undoubtedly grow around trees. Models exist to capture the limit of dense vegetation rather than individual tree trunks through an effective porous media approach [see 154]. Here, we reduce trees to cylinders with a constant elastic modulus, thereby neglecting possible species-specific differences in the breaking pattern of the trunk, the branching structure emerging from the trunk, or the root structure [e.g., 207, 210, 212, 217]. Our work is hence merely a small step towards improving our understanding of the intricate interactions between onshore vegetation and tsunami impacts. Further work would be needed to assess the protective benefit of vegetation with an inherently three-dimensional structure like mangroves that can not be meaningfully reduced to a single trunk or stem.

Another limitation of our work is the Froude similarity law we use to scale down the model. This choice implies that the Froude number in our simulations is comparable to field values estimated by Foytong et al. [48], Kawata et al. [93], but the Reynolds number characterizing our simulations is two orders of magnitude lower than existing estimates for the Indian Ocean tsunami [114]. While this difference is undoubtedly large, tsunamis in the field vary enormously in their Reynolds number, implying that there is no right number. One consequence of our scaling is that the

drag; and hence the energy dissipation may differ between the simulation and the field. Many experimental and analytical studies proposed an energy-dissipation relation based on the drag force, which varies with the Reynolds number [109, 127, 155]. According to Anderson Jr [1], the drag remains constant when the Reynolds number exceeds 10^6, but our simulations fall below this range. Other factors will undoubtedly contribute to a difference in drag, such as the roughness of tree bark. We hence emphasize that our simulations are not intended as a high-fidelity representation of realistic tree trunks and tsunami flows but present an attempt to better understand the basic fundamental physical processes through which coastal forests reduce tsunami impacts onshore.

CHAPTER 7

CONCLUSIONS AND FUTURE WORK

7.1 Summary

In this dissertation, we aim to analyze the importance of different tree parameters in tsunami energy attenuation. To achieve our goal, we quantify how the reflection and dissipation of onshore tsunami flow depend on the rigidity and arrangement of trees in a coastal forest. We use a three-dimensional LES turbulent model to study the effect of varying rigidity, tree spacing, and the number of trees on tsunami energy attenuation. To represent the dynamic interplay between the tsunami bore and the trees, we employ a two-way FSI model to capture the coupling between fluid and solid body interaction. We compute the energy flux at different streamwise locations to quantify the energy reflection and dissipation for three sets of moduli of elasticity and different cylinder configurations. Our simulations suggest that the rigidity of tree trunks only increases the reflection of kinetic energy flux in the somewhat abstract case of a single cylinder. Even small deflections of the tree trunk alter the flow structures downstream, impacting flow velocity and enhancing turbulent kinetic energy. This variability in velocity distribution and turbulent kinetic energy is more pronounced when the number of cylinders increases, highlighting that rigidity is less important than the number and arrangement of the trees. An important caveat to this conclusion is that we did not capture shear-driven erosion, sediment transport, or tree breakage, all of which could limit the ability of the tree trunks to withstand tsunami impact.

7.2 Future Work

The limitations of our studies are presented in Chapter 6 and Section 7.1, and from this research, future work can be explored as shown below.

Implementation of hybrid scheme

In tsunami mitigation park design, a hybrid scheme is preferred where green elements such as trees are combined with engineered elements such as hills. Hills are the preferred choice due to being capable of reflecting a large amount of tsunami energy. However, they are typically made of erodible material, and their shape could be rapidly changed by tsunami induced scour. On the other hand, forests can provide better support in terms of energy dissipation and the prevention of erosion. Therefore, our study can be extended to conduct the energy balance by combining the hills with trees to understand the tsunami-hydrodynamics so that the hybrid system can be implemented strategically. As per the author's knowledge, there have not been any studies conducted so far where hills are combined with the forest to capture energy balance for different hills and tree parameters. There are some studies [208, 211] where embankments or dunes are combined with trees, and these artificial structures are considered as a proxy of hills. Nevertheless, those studies did not consider tsunami induced scour and energy dissipation.

Effect of tsunami induced scour

In our study, we did not consider the effect of shear-driven erosion and sediment transport. Since trees can hold the soil together and prevent shear-driven erosion, future studies can be conducted to understand how different tree parameters can affect scour. Although tsunami induced scour has been studied, the effect of the bendability of trees on erosion prevention has not been explored yet. Therefore, complex analysis can be made by implementing the Lagrangian particle model within the fluid-structure interaction.

REFERENCES

[1] J. D. Anderson Jr. *Fundamentals of Aerodynamics*. New York, NY: McGraw-Hill, 1991.

[2] H. Arnason, C. Petroff, and H. Yeh. Tsunami bore impingement onto a vertical column. *Journal of Disaster Research*, 4(6):391–403, 2009.

[3] O. Bafkar, J. C. Cajas, H. Calmet, G. Houzeaux, G. Rosengarten, D. Lester, V. Nguyen, S. Gulizia, and I. S. Cole. Impact of sleeping position, gravitational force & effective tissue stiffness on obstructive sleep apnoea. *Journal of Biomechanics*, 104:109715, 2020.

[4] R. Balin, K. E Jansen, and P. R Spalart. Wall-modeled LES of flow over a gaussian bump with strong pressure gradients and separation. In *American Institute of Aeronautics and Astronautics Journal Aviation 2020 Forum*, page 3012, 2020.

[5] A. M. Baptista, G. R. Priest, and T. S. Murty. Field survey of the 1992 Nicaragua tsunami. *Marine Geodesy*, 16(2):169–203, 1993.

[6] M. Bathe and R. D. Kamm. A fluid-structure interaction finite element analysis of pulsatile blood flow through a compliant stenotic artery. *Journal of Biomechanical Engineering*, 121(4):361–369, 1999.

[7] J. C. L. Bayas, C. Marohn, G. Dercon, S. Dewi, H. P. Piepho, L. Joshi, V. M. Noordwijk, and G. Cadisch. Influence of coastal vegetation on the 2004 tsunami wave impact in west Aceh. *Proceedings of the National Academy of Sciences*, 108(46):18612–18617, 2011.

[8] Y. Bazilevs, K. Takizawa, and T. E. Tezduyar. *Computational fluid-structure interaction: Methods and applications*. New York, NY: John Wiley & Sons, 2013.

[9] A. Bechmann and N. N. Sørensen. Hybrid RANS/LES method for wind flow over complex terrain. *Wind Energy: An International Journal for Progress and Applications in Wind Power Conversion Technology*, 13(1): 36–50, 2010.

[10] J. Behrens and F. Dias. New computational methods in tsunami science. *Philosophical Transactions of the Royal Society A*, 373:20140382, 2015.

[11] J. Behrens, F. Løvholt, F. Jalayer, S. Lorito, M. A. Salgado-Gálvez, M. Sørensen, S. Abadie, I. Aguirre-Ayerbe, I. Aniel-Quiroga, A. Babeyko, M. Baiguera, R. Basili, S. Belliazzi, A. Grezio, K. Johnson, S. Murphy, R. Paris, I. Rafliana, R. De Risi, T. Rossetto, J. Selva, M. Taroni, M. Del Zoppo, A. Armigliato, V. Bureš, P. Cech, C. Cecioni, P. Christodoulides, G. Davies, F. Dias, H. B. Bayraktar, M. González, M. Gritsevich, S. Guillas, C. B. Harbitz, U. Kânoğlu, J. Macías, G. A. Papadopoulos, J. Polet, F. Romano, A. Salamon, A. Scala, M. Stepinac, D. R. Tappin, H. K. Thio, R. Tonini, I. Triantafyllou, T. Ulrich, E. Varini, M. Volpe, and E. Vyhmeister. Probabilistic tsunami hazard and risk analysis: A review of research gaps. *Frontiers in Earth Science*, 9, 2021.

[12] T. Belytschko, W. K. Liu, B. Moran, and K. Elkhodary. *Nonlinear finite elements for continua and structures*. New York, NY: John Wiley & Sons, 2014.

[13] A. Ben-Menahem and M. Rosenman. Amplitude patterns of tsunami waves from submarine earthquakes. *Journal of Geophysical Research*, 77(17): 3097–3128, 1972.

[14] M. J. Berger, D. L. George, R. J. LeVeque, and K. T. Mandli. The GeoClaw software for depth-averaged flows with adaptive refinement. *Advances in Water Resources*, 34(9):1195–1206, 2011.

[15] E. N. Bernard, H. O. Mofjeld, V. Titov, C. E. Synolakis, and F. I. González. Tsunami: Scientific frontiers, mitigation, forecasting and policy implications. *Philosophical Transactions of the Royal Society A: Mathematical, Physical and Engineering Sciences*, 364(1845):1989–2007, 2006.

[16] R. S. Bhalla. Do bio-shields affect tsunami inundation? *Current Science*, pages 831–833, 2007.

[17] B. B. Bingham and J. O. Sawyer. Canopy structure and tree condition of young, mature, and old-growth Douglas-fir/hardwood forests. In *Proceedings of the Symposium on Biodiversity of Northwestern California; 1991 October 28-30, Santa Rosa, CA. Berkeley, CA: University of California, Wildland Resources Center Report No. 29*, pages 141–149, 1992.

[18] J. C. Borrero, C. E. Synolakis, and H. Fritz. Northern Sumatra field survey after the December 2004 great Sumatra earthquake and Indian Ocean tsunami. *Earthquake Spectra*, 22(3_suppl):93–104, 2006.

[19] S. T. Bose and G. I. Park. Wall-modeled large-eddy simulation for complex turbulent flows. *Annual Review of Fluid Mechanics*, 50:535, 2018.

[20] R. D. Braddock, P. Van Den Driessche, and G. W. Peady. Tsunami generation. *Journal of Fluid Mechanics*, 59(4):817–828, 1973.

[21] F. Bulleri and M. G. Chapman. The introduction of coastal infrastructure as a driver of change in marine environments. *Journal of Applied Ecology*, 47, 2010.

[22] H. J. Bungartz, M. Mehl, and M. Schäfer. *Fluid Structure Interaction II: Modelling, Simulation, Optimization*, volume 73. Springer Science & Business Media, 2010.

[23] J. C. Cajas, G. Houzeaux, M. Vazquez, M. García, E. Casoni, H. Calmet, A. Artigues, R. Borrell, O. Lehmkuhl, D. Pastrana, et al. Fluid-structure interaction based on HPC multicode coupling. *SIAM Journal on Scientific Computing*, 40(6):C677–C703, 2018.

[24] H. Calmet, A. Santiago, J. C. Cajas, C. Langdon, B. Eguzkitza, and G. Houzeaux. Fluid–structure interaction of human nasal valves under sniff conditions and transport of inhaled aerosols: A numerical study. *Journal of Aerosol Science*, 165:106040, 2022.

[25] G. F. Carrier and H. P. Greenspan. Water waves of finite amplitude on a sloping beach. *Journal of Fluid Mechanics*, 4(1):97–109, 1958.

[26] E. Casoni, A. Jérusalem, C. Samaniego, B. Eguzkitza, P. Lafortune, D. D. Tjahjanto, X. Sáez, G. Houzeaux, and M. Vázquez. Alya: Computational solid mechanics for supercomputers. *Archives of Computational Methods in Engineering*, 22(4):557–576, 2015.

[27] Y. C. Chang, T. Y. Hou, B. Merriman, and S. Osher. A level set formulation of eulerian interface capturing methods for incompressible fluid flows. *Journal of Computational Physics*, 124(2):449–464, 1996.

[28] H. Chanson. *Hydraulics of stepped chutes and spillways*. CRC Press, 2002.

[29] I. Charvet, I. Eames, and T. Rossetto. New tsunami runup relationships based on long wave experiments. *Ocean Modeling*, 69:79–92, 2013.

[30] B. Chatenoux and P. Peduzzi. Impacts from the 2004 Indian Ocean tsunami: analysing the potential protecting role of environmental features. *Natural Hazards*, 40(2):289–304, 2007.

[31] E. Christensen. Large eddy simulation of spilling and plunging breakers. *Coastal Engineering*, 53:463–485, 2006.

[32] R. Cochard, S. L. Ranamukhaarachchi, G. P. Shivakoti, O. V. Shipin, P. J. Edwards, and K. T. Seeland. The 2004 tsunami in Aceh and Southern Thailand: a review on coastal ecosystems, wave hazards and vulnerability. *Perspectives in Plant Ecology, Evolution and Systematics*, 10(1):3–40, 2008.

[33] R. Codina. A stabilized finite element method for generalized stationary incompressible flows. *Computer Methods in Applied Mechanics and Engineering*, 190(20-21):2681–2706, 2001.

[34] F. Dahdouh-Guebas, L. P. Jayatissa, D. D. Nitto, J. O. Bosire, D. L. Seen, and N. Koedam. How effective were mangroves as a defence against the recent tsunami? 15(12):R443–R447, 2005.

[35] F. Danielsen, M. K. Sørensen, M. F. Olwig, V. Selvam, F. Parish, N. D. Burgess, T. Hiraishi, V. M. Karunagaran, M. S. Rasmussen, L. B. Hansen, et al. The Asian tsunami: A protective role for coastal vegetation. *Science*, 310(5748): 643, 2005.

[36] R. G. Dean and R. A. Dalrymple. *Coastal processes with engineering applications*. Cambridge: Cambridge University Press, 2002.

[37] L. Dengler and J. Preuss. Mitigation lessons from the July 17, 1998 Papua New Guinea tsunami. In *Landslide Tsunamis: Recent Findings and Research Directions*, pages 2001–2031. Springer, 2003.

[38] W. Dettmer and D. Perić. A computational framework for fluid–structure interaction: finite element formulation and applications. *Computer Methods in Applied Mechanics and Engineering*, 195(41-43):5754–5779, 2006.

[39] D. I. Dilmen, G. H. Roe, Y. Wei, and V. V. Titov. The role of near-shore bathymetry during tsunami inundation in a reef island setting: A case study of Tutuila Island. *Pure and Applied Geophysics*, 175(4):1239–1256, 2018.

[40] U. Drähne, N. Goseberg, S. Vater, N. Beisiegel, and J. Behrens. An experimental and numerical study of long wave run-up on a plane beach. *Journal of Marine Science and Engineering*, 4(1):1, 2015.

[41] W. C. Dudley. *Tsunami!* University of Hawaii Press, 1998.

[42] J. E. Dugan and D. M. Hubbard. Ecological effects of coastal armoring: A summary of recent results for exposed sandy beaches in Southern California. In *Proceedings of a State of the Science Workshop (Richland, Washington)*, pages 187–194, 2010.

[43] D. Dutykh, R. Poncet, and F. Dias. The VOLNA code for the numerical modeling of tsunami waves: generation, propagation and inundation. *European Journal of Mechanics-B/Fluids*, 30:598–615, 2011.

[44] C. Farhat and M. Lesoinne. Two efficient staggered algorithms for the serial and parallel solution of three-dimensional nonlinear transient aeroelastic problems. *Computer Methods in Applied Mechanics and Engineering*, 182 (3-4):499–515, 2000.

[45] C. A. Felippa, K. C. Park, and C. Farhat. Partitioned analysis of coupled mechanical systems. *Computer Methods in Applied Mechanics and Engineering*, 190(24-25):3247–3270, 2001.

[46] B. E. Flammang, S. Marras, E. J. Anderson, O. Lehmkuhl, A. Mukherjee, D. E. Cade, M. Beckert, J. H. Nadler, G. Houzeaux, M. Vázquez, et al. Remoras pick where they stick on blue whales. *Journal of Experimental Biology*, 223 (20):226654, 2020.

[47] F. R. Fosberg and V. J. Chapman. Mangroves v. tidal waves. *Biological Conservation*, 4(1):38–39, 1971.

[48] P. Foytong, A. Ruangrassamee, G. Shoji, Y. Hiraki, and Y. Ezura. Analysis of tsunami flow velocities during the March 2011 Tohoku, Japan, tsunami. *Earthquake Spectra*, 29(1_suppl):161–181, 2013.

[49] D. R. Fuhrman and P. A. Madsen. Tsunami generation, propagation, and run-up with a high-order Boussinesq model. *Coastal Engineering*, 56(7): 47–758, 2009.

[50] A. Gailler, H. Hbert, A. Loevenbruck, and B. Hernandez. Simulation systems for tsunami wave propagation forecasting within the French tsunami warning system. *Natural Hazards and Earth System Sciences*, 13:2465–2482, 2013.

[51] G. Gelfenbaum, D. Vatvani, B. Jaffe, and F. Dekker. Tsunami inundation and sediment transport in vicinity of coastal mangrove forest. In *Coastal Sediments' 07*, pages 1117–1128. 2007.

[52] M. Germano, U. Piomelli, P. Moin, and W. H. Cabot. A dynamic subgrid-scale eddy viscosity model. *Physics of Fluids A: Fluid Dynamics*, 3(7): 1760–1765, 1991.

[53] J. J. Gerth, R. K. Garcia, D. J. Hoese, S. S Lindstrom, and T. J Schmit. SIFTing through satellite imagery with the satellite information familiarization tool. 2020.

[54] U. Ghani, N. Anjum, G. A. Pasha, and M. Ahmad. Numerical investigation of the flow characteristics through discontinuous and layered vegetation patches of finite width in an open channel. *Environmental Fluid Mechanics*, 19(6):1469–1495, 2019.

[55] D. A. Gieseking, J. Choi, J. R. Edwards, and H. A. Hassan. Compressible-flow simulations using a new large-eddy simulation/Reynolds-averaged Navier-Stokes model. *American Institute of Aeronautics and Astronautics Journal*, 49(10):2194–2209, 2011.

[56] F. X. Giraldo and M. Restelli. A conservative discontinuous Galerkin semi-implicit formulation for the Navier-Stokes Equations in nonhydrostatic mesoscale modeling. *SIAM Journal on Scientific Computing*, 31:2231–2257, 2009.

[57] F. I. Gonzalez, H. M. Milburn, E. N. Bernard, and J. C. Newman. Deep-ocean assessment and reporting of tsunamis (DART): Brief overview and status report. In *Proceedings of the International Workshop on Tsunami Disaster Mitigation*, volume 19, page 2. National Oceanic and Atmospheric Administration, Tokyo, Japan, 1998.

[58] N. Goseberg, A. Wurpts, and T. Schlurmann. Laboratory-scale generation of tsunami and long waves. *Coastal Engineering*, 79:57–74, 2013.

[59] D. W. Green, E. W. Jerrold, and E. K. David. Mechanical properties of wood. *Journal of Wood Handbook: US Department of Agriculture, Forest Service, Products Laboratory*, pages 4–1, 1999.

[60] G. Green et al. On the motion of waves in a variable canal of small depth and width. *Transactions of the Cambridge Philosophical Society*, 6:457, 1838.

[61] C. J. Greenshields and H. G. Weller. A unified formulation for continuum mechanics applied to fluid–structure interaction in flexible tubes. *International Journal for Numerical Methods in Engineering*, 64(12): 1575–1593, 2005.

[62] J. Grue, E. N. Pelinovsky, D. Fructus, T. Talipova, and C. Kharif. Formation of undular bores and solitary waves in the Strait of Malacca caused by the 26 December 2004 Indian Ocean tsunami. *Journal of Geophysical Research: Oceans*, 113(C5), 2008.

[63] W. H. Hager. B-jump in sloping channel. *Journal of Hydraulic Research*, 26(5): 539–558, 1988.

[64] J. L. Hammack and H. Segur. The Korteweg-de Vries equation and water waves. Part 2. Comparison with experiments. *Journal of Fluid Mechanics*, 65(2): 289–314, 1974.

[65] J. L. Hammack and H. Segur. The Korteweg-de Vries equation and water waves. Part 3. Oscillatory waves. *Journal of Fluid Mechanics*, 84(2):337–358, 1978.

[66] S. Harig, X. Chaeroni, W. S. Pranowo, and J. Behrens. Tsunami simulations on several scales: Comparison of approaches with unstructured meshes and nested grids. *Ocean Dynamics*, 58:429–440, 2008.

[67] M. Heil. An efficient solver for the fully coupled solution of large-displacement fluid–structure interaction problems. *Computer Methods in Applied Mechanics and Engineering*, 193(1-2):1–23, 2004.

[68] C. Hentry, N. Chandrasekar, S. Saravanan, and J. D. Sahayam. Influence of geomorphology and bathymetry on the effects of the 2004 tsunami at Colachel, South India. *Bulletin of Engineering Geology and the Environment*, 69(3):431–442, 2010.

[69] R. Hirota. Exact solution of the Korteweg-de Vries equation for multiple collisions of solitons. *Physical Review Letters*, 27(18):1192, 1971.

[70] J. Horrillo, A. Wood, G. B. Kim, and A. Parambath. A simplified 3-D Navier–Stokes numerical model for landslide tsunami: Application to the Gulf of Mexico. *Journal of Geophysical Research: Oceans*, 118:6934–6950, 2013.

[71] G. Houzeaux, M. Vázquez, R. Aubry, and J. Cela. A massively parallel fractional step solver for incompressible flows. *Journal of Computational Physics*, 228(17):6316–6332, 2009.

[72] G. Houzeaux, R. Aubry, and M. Vázquez. Extension of fractional step techniques for incompressible flows: The preconditioned Orthomin (1) for the pressure Schur complement. *Computers & Fluids*, 44(1):297–313, 2011.

[73] S. Hsiao, P. L. F Liu, and Y. Chen. Nonlinear water waves propagating over a permeable bed. *Proceedings of the Royal Society of London. Series A: Mathematical, Physical and Engineering Sciences*, 458(2022):1291–1322, 2002.

[74] Z. Huang, Y. Yao, S. Y. Sim, and Y. Yao. Interaction of solitary waves with emergent stationary vegetation. *Ocean Engineering*, 38:1080–1088, 2011.

[75] Science Learning Hub. Tsunami shoaling, Retrieved October 30, 2022. URL https://www.sciencelearn.org.nz/resources/596-tsunami-shoaling.

[76] B. Hübner, E. Walhorn, and D. Dinkler. A monolithic approach to fluid–structure interaction using space–time finite elements. *Computer Methods in Applied Mechanics and Engineering*, 193(23-26):2087–2104, 2004.

[77] Y. Igarashi, N. Tanaka, H. Sato, and H. Torita. Tsunami mitigation effect and tree breaking situation of Dahurian larch coastal forest at six growth stages under thinning management of trees. In *Proceedings of the 38th IAHR World Congress, Panama City, Panama*, 2019.

[78] K. Iida. Earthquakes accompanied by tsunamis occurring under the sea off the islands of Japan. *Journal of Earth Science*, 4(1):1–43, 1956.

[79] K. Iida. The generation of tsunamis and the focal mechanism of earthquakes. *Tsunamis in the Pacific Ocean*, pages 3–18, 1970.

[80] K. Iida, D. C. Cox, and G. Pararas-Carayannis. Preliminary catalog of tsunamis occurring in the Pacific Ocean. Technical report, Hawaii Institute of Geophysics, Honolulu, Hawaii, 1967.

[81] K. Iimura and N. Tanaka. Numerical simulation estimating effects of tree density distribution in coastal forest on tsunami mitigation. *Ocean Engineering*, 54:223–232, 2012.

[82] A. Imamura. History of Japanese tsunamis. *Kayo-No-Kagaku: Oceanography*, 2(2):74–80, 1942.

[83] A. Imamura. List of tsunamis in Japan. *Journal of the Seismological Society of Japan*, 2:23–28, 1949.

[84] F. Imamura, A. C. Yalciner, and G. Ozyurt. Tsunami modelling manual. *Intergovernmental Oceanographic Commission: International Training Course on Tsunami Numerical Modelling*, 2006.

[85] J. L. Irish, R. Weiss, Y. Yang, Y. K. Song, A. Zainali, and R. Marivela-Colmenarejo. Laboratory experiments of tsunami run-up and withdrawal in patchy coastal forest on a steep beach. *Natural Hazards*, 74(3):1933–1949, 2014.

[86] L. R. Iverson and A. M. Prasad. Using landscape analysis to assess and model tsunami damage in Aceh province, Sumatra. *Landscape Ecology*, 22(3): 323–331, 2007.

[87] P. S. Iyer and M. R. Malik. Wall-modeled LES of the NASA juncture flow experiment. In *AIAA Scitech 2020 Forum*, page 1307, 2020.

[88] N. G. Jacobsen, D. R. Fuhrman, and J. Fredsoe. A wave generation toolbox for the open-source CFD library: OpenFOAM (R). *International Journal for Numerical Methods in Fluids*, 70:1073–1088, 2012.

[89] C. Jiang, J. Chen, Y. Yao, J. Liu, and Y. Deng. Study on threshold motion of sediment and bedload transport by tsunami waves. *Ocean Engineering*, 100:97–106, 2015.

[90] K. Kajiura. The leading wave of a tsunami. *Bulletin of the Earthquake Research Institute, University of Tokyo*, 41(3):535–571, 1963.

[91] K. Kathiresan and N. Rajendran. Coastal mangrove forests mitigated tsunami. *Estuarine, Coastal and Shelf Science*, 65(3):601–606, 2005.

[92] S. Kawai and J. Larsson. Wall-modeling in large eddy simulation: Length scales, grid resolution, and accuracy. *Physics of Fluids*, 24(1):015105, 2012.

[93] Y. Kawata, B. C. Benson, J. C. Borrero, J. L. Borrero, H. L. Davies, W. P. de Lange, F. Imamura, H. Letz, J. Nott, and C. E. Synolakis. Tsunami in Papua New Guinea was as intense as first thought. *Eos, Transactions American Geophysical Union*, 80(9):101–105, 1999.

[94] J. B. Keller and H. B. Keller. Water wave run-up on a beach. Technical report, Service Bureau Corporation, New York, NY, 1964.

[95] A. B. Kennedy, Q. Chen, J. T. Kirby, and R. A. Dalrymple. Boussinesq modeling of wave transformation, breaking and runup, part I: 1D. *Journal of Waterway, Port, Coastal, and Ocean Engineering*, 126:39–47, 2000.

[96] A. M. Kerr and A. H. Baird. Natural barriers to natural disasters. *BioScience*, 57(2):102–103, 2007.

[97] A. M. Kerr, A. H. Baird, and S. J. Campbell. Comments on "Coastal mangrove forests mitigated tsunami" by K. Kathiresan and N. Rajendran [estuarine, coastal and shelf science,65:601–606,2005]. *Estuarine, Coastal and Shelf Science*, 67:539–541, 2006.

[98] A. M. Kerr, A. H. Baird, R. S. Bhalla, and V. Srinivas. Reply to "Using remote sensing to assess the protective role of coastal woody vegetation against tsunami waves". *International Journal of Remote Sensing*, 30(14): 3817–3820, 2009.

[99] G. Khakimzyanov, D. Dutykh, and O. Gusev. Dispersive shallow water wave modelling. Part IV: numerical simulation on a globally spherical geometry. *arXiv preprint arXiv:1707.02552*, 2017.

[100] A. Khamayseh and A. Kuprat. Deterministic point inclusion methods for computational applications with complex geometry. *Computational Science & Discovery*, 1(1):015004, 2008.

[101] N. Kihara, T. Arikawa, T. Asai, M. Hasebe, T. Ikeya, S. Inoue, H. Kaida, H. Matsutomi, Y. Nakano, Y. Okuda, et al. A physical model of tsunami inundation and wave pressures for an idealized coastal industrial site. *Coastal Engineering*, 169:103970, 2021.

[102] D. H. Kim and P. J. Lynett. Dispersive and nonhydrostatic pressure effects at the front of surge. *Journal of Hydraulic Engineering*, 137(7):754–765, 2010.

[103] D. H. Kim and P. J. Lynett. Turbulent mixing and passive scalar transport in shallow flows. *Physics of Fluids*, 23:016603, 2011.

[104] J. Kim, P. Moin, and R. Moser. Turbulence statistics in fully developed channel flow at low Reynolds number. *Journal of Fluid Mechanics*, 177:133–166, 1987.

[105] Y. Kim, Z. Zhou, T. J Hsu, and J. A Puleo. Large eddy simulation of dam-break-driven swash on a rough-planar beach. *Journal of Geophysical Research: Oceans*, 122(2):1274–1296, 2017.

[106] P. Komar. *Beach processes and sedimentation*. Hoboken, NJ: Prantice Hall, 1998.

[107] P. Kundu, V. Kumar, Y. Hoarau, and I. M. Mishra. Numerical simulation and analysis of fluid flow hydrodynamics through a structured array of circular cylinders forming porous medium. *Applied Mathematical Modelling*, 40 (23-24):9848–9871, 2016.

[108] U. Küttler and W. A. Wall. Fixed-point fluid–structure interaction solvers with dynamic relaxation. *Computational Mechanics*, 43(1):61–72, 2008.

[109] A. P. Kyprioti, A. A. Taflanidis, and A. B. Kennedy. Dissipation effects of coastal vegetation on nearshore structures under wave runup loading. *Journal of Structural Engineering*, 147(3), 2021.

[110] N. Lakshmanan, M. Kantharaj, and V. Sundar. The effects of flexible vegetation on forces with a Keulegan-Carpenter number in relation to structures due to long waves. *Journal of Marine Science and Application*, 11(1):24–33, 2012.

[111] B. E. Larsen and D. R. Fuhrman. Full-scale CFD simulation of tsunamis. Part 1: Model validation and run-up. *Coastal Engineering*, 151:22–41, 2019.

[112] B. E. Larsen and D. R. Fuhrman. Full-scale CFD simulation of tsunamis. Part 2: Boundary layers and bed shear stresses. *Coastal Engineering*, 151:42–57, 2019.

[113] J. Larsson, S. Kawai, J. Bodart, and I. Bermejo-Moreno. Large eddy simulation with modeled wall-stress: Recent progress and future directions. *Mechanical Engineering Reviews*, 3(1):15–00418, 2016.

[114] F. Lavigne, R. Paris, D. Grancher, P. Wassmer, D. Brunstein, F. Vautier, F. Leone, F. Flohic, B. De Coster, T. Gunawan, et al. Reconstruction of tsunami inland propagation on December 26, 2004 in Banda Aceh, Indonesia, through field investigations. *Pure and Applied Geophysics*, 166 (1-2):259–281, 2009.

[115] O. Lehmkuhl, G. Chrysokentis, S. Gomez, and H. Owen. Large eddy simulation for automotive aerodynamics with Alya. *Tenth International Conference on Computational Fluid Dynamics (ICCFD10), Barcelona, Spain*, pages 1–11, 2018.

[116] E. Lekkas, E. Andreadakis, I. Kostaki, and E. Kapourani. Critical factors for run-up and impact of the Tohoku earthquake tsunami. *International Journal of Geosciences*, 2(3):310, 2011.

[117] A. Leonard. Energy cascade in large eddy simulations of turbulent fluid flows. *Advances in Geophysics*, 18:237–248, 1974.

[118] F. Leone, F. Lavigne, R. Paris, J. C. Denain, and F. Vinet. A spatial analysis of the December 26th, 2004 tsunami-induced damages: Lessons learned for a better risk assessment integrating buildings vulnerability. *Applied Geography*, 31(1):363–375, 2011.

[119] Y. Li. *Tsunamis: Non-breaking and breaking solitary wave run-up*. PhD thesis, Pasadena, California, California Institute of Technology, 2000.

[120] Y. Li and F. Raichlen. Solitary wave runup on plane slopes. *Journal of Waterway, Port, Coastal, and Ocean Engineering*, 127(1):33–44, 2001.

[121] Y. Li and F. Raichlen. Non-breaking and breaking solitary wave run-up. *Journal of Fluid Mechanics*, 456:295–318, 2002.

[122] P. Lin and P. Liu. Turbulence transport, vorticity dynamics, and solute mixing under plunging breaking waves in surf zone. *Journal of Geophysical Research: Oceans*, 103 C8, 1998.

[123] P. Lin and P. Liu. A numerical study of breaking waves in the surf zone. *Journal of Fluid Mechanics*, 358:239–264, 1998.

[124] H. Liu, T. Shimozono, T. Takagawa, A. Okayasu, H. M. Fritz, S. Sato, and Y. Tajima. The 11 March 2011 Tohoku tsunami survey in Rikuzentakata and comparison with historical events. *Pure and Applied Geophysics*, 170 (6):1033–1046, 2013.

[125] Y. Liu, J. Mitchell, Y. Chen, W. Yim, W. Chu, and R. C. Wang. Study of the upper airway of obstructive sleep apnea patient using fluid structure interaction. *Respiratory Physiology & Neurobiology*, 249:54–61, 2018.

[126] G. Lodato, P. Castonguay, and A. Jameson. Structural wall-modeled LES using a high-order spectral difference scheme for unstructured meshes. *Flow, Turbulence and Combustion*, 92(1):579–606, 2014.

[127] M. Luhar, S. Coutu, E. Infantes, S. Fox, and H. Nepf. Wave-induced velocities inside a model seagrass bed. *Journal of Geophysical Research: Oceans*, 115 (C12), 2010.

[128] B. Lunghino, A. F. S. Tate, M. Mazereeuw, A. Muhari, F. X Giraldo, S. Marras, and J. Suckale. The protective benefits of tsunami mitigation parks and ramifications for their strategic design. *Proceedings of the National Academy of Sciences*, 117(20):10740–10745, 2020.

[129] P. J. Lynett. Nearshore wave modeling with high-order Boussinesq-type equations. *Journal of Waterway, Port, Coastal, and Ocean Engineering*, 132(5):348–357, 2006.

[130] P. J. Lynett. Effect of a shallow water obstruction on long wave runup and overland flow velocity. *Journal of Waterway, Port, Coastal, and Ocean Engineering*, 133:455–462, 2007.

[131] P. J. Lynett, T. R. Wu, and Liu P. L. F. Modeling wave runup with depth-integrated equations. *Coastal Engineering*, 46:89–107, 2002.

[132] P. J. Lynett, J. C. Borrero, P. L. Liu, and C. E. Synolakis. Field survey and numerical simulations: A review of the 1998 Papua New Guinea tsunami. *Landslide Tsunamis: Recent Findings and Research Directions*, pages 2119–2146, 2003.

[133] J. A. MacKinnon and M. C. Gregg. Mixing on the late-summer New England shelf–Solibores, shear, and stratification. *Journal of Physical Oceanography*, 33(7):1476–1492, 2003.

[134] P. A. Madsen and D. R. Fuhrman. Run-up of tsunamis and long waves in terms of surf-similarity. *Coastal Engineering*, 55(3):209–223, 2008.

[135] P. A. Madsen and H. A. Schaeffer. Analytical solutions for tsunami runup on a plane beach: Single waves, n-waves and transient waves. *Journal of Fluid Mechanics*, 645:27–57, 2010.

[136] P. A. Madsen, R. Murray, and O. R. Sørensen. A new form of the Boussinesq equations with improved linear dispersion characteristics. *Coastal Engineering*, 15(4):371–388, 1991.

[137] P. A. Madsen, H. B. Bingham, and H. Liu. A new Boussinesq method for fully nonlinear waves from shallow to deep water. *Journal of Fluid Mechanics*, 462:1–30, 2002.

[138] P. A. Madsen, D. R. Fuhrman, and H. A. Schäffer. On the solitary wave paradigm for tsunamis. *Journal of Geophysical Research: Oceans*, 113 (C12), 2008.

[139] P. A. Madsen, H. A Schäffer, D. R. Fuhrman, and Y. Toledo. Uniform asymptotic approximations for transient waves due to an initial disturbance. *Journal of Geophysical Research: Oceans*, 121(1):60–84, 2016.

[140] S. Marras and K. T. Mandli. Modeling and simulation of tsunami impact: A short review of recent advances and future challenges. *Geosciences*, 11(1): 5, 2020.

[141] S. Marras, M. Kopera, and F. X. Giraldo. Simulation of shallow water jets with a unified element-based continuous/discontinuous Galerkin model with grid flexibility on the sphere. *Quarterly Journal of the Royal Meteorological Society*, 141(690):1727–1739, 2015.

[142] S. Marras, M. Nazarov, and F. X. Giraldo. Stabilized high-order Galerkin methods based on a parameter free dynamic SGS model for LES. *Journal of Computational Physics*, 301:77–101, 2015.

[143] S. Marras, M. A. Kopera, E. M. Constantinescu, J. Suckale, and F. X. Giraldo. A residual-based shock capturing scheme for the continuous/discontinuous spectral element solution of the 2D shallow water equations. *Advances in Water Resources*, 114:45–63, 2018.

[144] J. C. Martin and W. J. Moyce. Part IV: An experimental study of the collapse of liquid columns on a rigid horizontal plane. *Philosophical Transactions of the Royal Society*, 224:312–325, 1952.

[145] A. Mascarenhas and S. Jayakumar. An environmental perspective of the post-tsunami scenario along the coast of Tamil Nadu, India: Role of sand dunes and forests. *Journal of Environmental Management*, 89(1):24–34, 2008.

[146] A. Masud. Effects of mesh motion on the stability and convergence of ALE based formulations for moving boundary flows. *Computational Mechanics*, 38(4-5):430, 2006.

[147] M. Matsuyama, J. P. Walsh, and H. Yeh. The effect of bathymetry on tsunami characteristics at Sisano Lagoon, Papua New Guinea. *Geophysical Research Letters*, 26(23):3513–3516, 1999.

[148] M. Matsuyama, M. Ikeno, T. Sakakiyama, and T. Takeda. A study of tsunami wave fission in an undistorted experiment. In *Tsunami and its Hazards in the Indian and Pacific Oceans*, pages 617–631. Springer, 2007.

[149] S. A. Mattis, C. N. Dawson, C. E. Kees, and M. W. Farthing. Numerical modeling of drag for flow through vegetated domains and porous structures. *Advances in Water Resources*, 39, 2012.

[150] S. A. Mattis, C. N. Dawson, C. E. Kees, and M. W. Farthing. An immersed structure approach for fluid-vegetation interaction. *Advances in Water Resources*, 80, 2015.

[151] M. Maza, J. L. Lara, and I. J. Losada. A coupled model of submerged vegetation under oscillatory flow using Navier–Stokes equations. *Coastal Engineering*, 80, 2013.

[152] M. Maza, J. L. Lara, and I. J. Losada. Tsunami wave interaction with mangrove forests: A 3-D numerical approach,. *Coastal Engineering*, 98, 2015.

[153] Y. Mazda, E. Wolanski, B. King, A. Sase, D. Ohtsuka, and M. Magi. Drag force due to vegetation in mangrove swamps. *Mangroves and Salt Marshes*, 1 (3):193–199, 1997.

[154] C. C. Mei, I. C. Chan, P. L. F. Liu, Z. Huang, and W. Zhang. Long waves through emergent coastal vegetation. *Journal of Fluid Mechanics*, 687, 2011.

[155] F. J. Mendez and I. J. Losada. An empirical model to estimate the propagation of random breaking and nonbreaking waves over vegetation fields. *Coastal Engineering*, 51(2):103–118, 2004.

[156] N. Mori, T. Takahashi, T. Yasuda, and H. Yanagisawa. Survey of 2011 Tohoku earthquake tsunami inundation and run-up. *Geophysical Research Letters*, 38(7), 2011.

[157] N. Mori, D. T. Cox, T. Yasuda, and H. Mase. Overview of the 2011 Tohoku earthquake tsunami damage and its relation to coastal protection along the sanriku coast. *Earthquake Spectra*, 29(1_suppl):127–143, 2013.

[158] A. Mukherjee, J. C. Cajas, G. Houzeaux, O. Lehmkuhl, M. Vázquez, J. Suckale, and S. Marras. Using fluid-structure interaction to evaluate the energy dissipation of a tsunami run-up through idealized flexible trees. In *Proceedings of the ParCFD 2020 32nd International Conference on Parallel Computational Fluid Dynamics, Nice, France*, pages 11–13, 2020.

[159] K. Nanko, S. Suzuki, H. Noguchi, Y. Ishida, D. F. Levia, A. Ogura, H. Hagino, H. Matsumoto, H. Takimoto, and T. Sakamoto. Mechanical properties of Japanese black pine (Pinus Thunbergii Parl.) planted on coastal sand dunes: Resistance to uprooting and stem breakage by tsunamis. *Wood Science and Technology*, 53(2):469–489, 2019.

[160] H. M. Nepf. Flow and transport in regions with aquatic vegetation. *Annual Review of Fluid Mechanics*, 44:123–142, 2012.

[161] A. Nicolle and I. Eames. Numerical study of flow through and around a circular array of cylinders. *Journal of Fluid Mechanics*, 679:1–31, 2011.

[162] F. C. Nicoud. Flow with variable properties. *Annual Research Briefs*, page 289, 1998.

[163] O. Nwogu. Alternative form of Boussinesq equations for nearshore wave propagation. *Journal of Waterway, Port, Coastal, and Ocean Engineering*, 119 (6):618–638, 1993.

[164] NASA Earth Observatory. Tsunami destroys Lhoknga, Indonesia, Retrieved November 10, 2022. URL `https://earthobservatory.nasa.gov/IOTD/view.php?id=5132`.

[165] M. F. Olwig, M. K. Sørensen, M. S. Rasmussen, F. Danielsen, V. Selvam, L. B. Hansen, L. Nyborg, K. B. Vestergaard, F. Parish, and V. M. Karunagaran. Using remote sensing to assess the protective role of coastal woody vegetation against tsunami waves. *International Journal of Remote Sensing*, 28(13-14):3153–3169, 2007.

[166] M. E. Oshnack, J. V. Lindt, R. Gupta, D. Cox, and F. Aguíñiga. Effectiveness of small onshore seawall in reducing forces induced by tsunami bore: large scale experimental study. *Journal of Disaster Research*, 4(6):382–390, 2009.

[167] H. Owen, G. Chrysokentis, M. Avila, D. Mira, G. Houzeaux, R. Borrell, J. C. Cajas, and O. Lehmkuhl. Wall-modeled large-eddy simulation in a finite element framework. *International Journal for Numerical Methods in Fluids*, 92(1):20–37, 2020.

[168] C. E. Ozdemir, T. J. Hsu, and S. Balachandar. Direct numerical simulations of instability and boundary layer turbulence under a solitary wave. *Journal of Fluid Mechanics*, 731:545–578, 2013.

[169] G. A. Pasha and N. Tanaka. Undular hydraulic jump formation and energy loss in a flow through emergent vegetation of varying thickness and density. *Ocean Engineering*, 141:308–325, 2017.

[170] G. A. Pasha, N. Tanaka, J. Yagisawa, and F. N. Achmad. Tsunami mitigation by combination of coastal vegetation and a backward-facing step. *Coastal Engineering Journal*, 60(1):104–125, 2018.

[171] J. B. Perot. An analysis of the fractional step method. *Journal of Computational Physics*, 108(1):51–58, 1993.

[172] M. S. Peterson and M. R. Lowe. Implications of cumulative impacts to Estuarine and marine habitat quality for fish and invertebrate resources. *Reviews in Fisheries Science*, 17:505–523, 2009.

[173] S. P. Pijl. Free-boundary methods for multi-phase flows. AMA report 02-13. *Delft University of Technology*, 2002.

[174] S. B. Pope. *Turbulent flows*. Cambridge: Cambridge University Press, 2000.

[175] W. S. Pranowo, J. Behrens, J. Schlicht, and C. Ziemer. Adaptive mesh refinement applied to tsunami modeling: TsunaFLASH. In *Proceedings of the International Conference on Tsunami Warning (ICTW). Bali, Indonesia*, volume 6, 2008.

[176] Morino Project. Potential benefit of vegetation, Retrieved October 30, 2022. URL `https://morinoproject.com`.

[177] X. Qin, M. Motley, R. LeVeque, F. Gonzalez, and K. Mueller. A comparison of a two-dimensional depth-averaged flow model and a three-dimensional rans model for predicting tsunami inundation and fluid forces. *Natural Hazards and Earth System Sciences*, 18(9):2489–2506, 2018.

[178] A. Quarteroni, F. Saleri, and A. Veneziani. Factorization methods for the numerical approximation of Navier-Stokes equations. *Computer Methods in Applied Mechanics and Engineering*, 188(1-3):505–526, 2000.

[179] A. Raby, J. Macabuag, A. Pomonis, S. Wilkinson, and T. Rossetto. Implications of the 2011 Great East Japan tsunami on sea defence design. *International Journal of Disaster Risk Reduction*, 14:332–346, 2015.

[180] B. Ramaswamy, M. Kawahara, and T. Nakayama. Lagrangian finite element method for the analysis of two-dimensional sloshing problems. *International Journal for Numerical Methods in Fluids*, 6(9):659–670, 1986.

[181] A. H. M. Rashedunnabi and N. Tanaka. Energy reduction of a tsunami current through a hybrid defense system comprising a sea embankment followed by a coastal forest. *Geosciences*, 9(6):247, 2019.

[182] H. Reichardt. Vollständige darstellung der turbulenten geschwindigkeitsverteilung in glatten leitungen. *ZAMM-Journal of Applied Mathematics and Mechanics/Zeitschrift für Angewandte Mathematik und Mechanik*, 31(7):208–219, 1951.

[183] Z. Ren, B. Wang, T. Fan, and H. Liu. Numerical analysis of impacts of 2011 Japan Tohoku tsunami on China Coast. *Journal of Hydrodynamics*, 25(4): 580–590, 2013.

[184] D. Reymond, H. Okal, E. A. Hébert, and M. Bourdet. Rapid forecast of tsunami wave heights from a database of pre-computed simulations, and application during the 2011 Tohoku tsunami in French Polynesia. *Geophysical Research Letters*, 39:39, 2012.

[185] R. Rodríguez, P. Encina, M. Espinosa, and N. Tanaka. Field study on planted forest structures and their role in protecting communities against tsunamis: experiences along the coast of the Biobío Region, Chile. *Landscape and Ecological Engineering*, 12(1):1–12, 2016.

[186] J. A. Roelvink and G. K. V. Banning. Design and development of DELFT3D and application to coastal morphodynamics. *Oceanographic Literature Review*, 42:925, 1995.

[187] T. Rossetto, W. Allsop, I. Charvet, and D. I. Robinson. Physical modelling of tsunami using a new pneumatic wave generator. *Coastal Engineering*, 58 (6):517–527, 2011.

[188] P. Sagaut. *Large eddy simulation for incompressible flows: An introduction*. Springer Science & Business Media, 2006.

[189] S. Sarjamee, I. Nistor, and A. Mohammadian. Large eddy simulation of extreme hydrodynamic forces on structures with mitigation walls using OpenFOAM. *Natural Hazards*, 85(3):1689–1707, 2017.

[190] R. Scardovelli and S. Zaleski. Direct numerical simulation of free-surface and interfacial flow. *Annual Review of Fluid Mechanics*, 31(1):567–603, 1999.

[191] S. Schimmels, V. Sriram, and I. Didenkulova. Tsunami generation in a large scale experimental facility. *Coastal Engineering*, 110:32–41, 2016.

[192] R. Selvakumar and S. M. Ramasamy. Revealing effect of bathymetry over tsunami run-up through factor analysis. *Arabian Journal of Geosciences*, 6(12):4701–4708, 2013.

[193] J. A. Sethian and P. Smereka. Level set methods for fluid interfaces. *Annual Review of Fluid Mechanics*, 35(1):341–372, 2003.

[194] C. C. Shephard, C. M. Crain, and M. W. Beck. The protective role of coastal marshes: A systematic review and meta-analysis. *PLoS ONE*, 6-e27374, 2012.

[195] F. Shi, J. Kirby, J. Harris, J. Geiman, and S. T. Grilli. A high-order adaptive time-stepping TVD solver for Boussinesq modeling of breaking waves and coastal inundation. *Ocean Modeling*, 43-44:36–51, 2012.

[196] T. Shibayama. 2004 Indian Ocean tsunami. In *Handbook of Coastal Disaster Mitigation for Engineers and Planners*, pages 3–19. Elsevier, 2015.

[197] M. Shur, P. R. Spalart, M. K. Strelets, and A. K. Travin. A hybrid RANS-LES approach with delayed-DES and wall-modelled LES capabilities. *International Journal of Heat and Fluid Flow*, 29:1638–1649, 2008.

[198] J. Smagorinsky. General Circulation Experiments with the Primitive Equations. *Monthly Weather Review*, 91:99, 1963.

[199] V. Sriram, I. Didenkulova, A. Sergeeva, and S. Schimmels. Tsunami evolution and run-up in a large scale experimental facility. *Coastal Engineering*, 111: 1–12, 2016.

[200] D. Sugawara, K. Goto, and B. E. Jaffe. Numerical models of tsunami sediment transport–current understanding and future directions. *Marine Geology*, 352:295–320, 2014.

[201] A. Suppasri, A. Muhari, P. Ranasinghe, E. Mas, N. Shuto, F. Imamura, and S. Koshimura. Damage and reconstruction after the 2004 Indian Ocean tsunami and the 2011 Great East Japan tsunami. *Journal of Natural Disaster Science*, 34(1):19–39, 2012.

[202] M. Sussman, P. Smereka, and S. Osher. A level set approach for computing solutions to incompressible two-phase flow. *Journal of Computational Physics*, 114(1):146–159, 1994.

[203] C. E. Synolakis. The runup of solitary waves. *Journal of Fluid Mechanics*, 185: 523–545, 1987.

[204] C. E. Synolakis and E. N. Bernard. Tsunami science before and beyond Boxing Day 2004. *Philosophical Transactions of the Royal Society A: Mathematical, Physical and Engineering Sciences*, 364(1845):2231–2265, 2006.

[205] C. E. Synolakis and L. Kong. Runup measurements of the December 2004 Indian Ocean tsunami. *Earthquake Spectra*, 22(3_suppl):67–91, 2006.

[206] N. Tanaka. Vegetation bioshields for tsunami mitigation: Review of effectiveness, limitations, construction, and sustainable management. *Landscape and Ecological Engineering*, 5(1):71–79, 2009.

[207] N. Tanaka. Effectiveness and limitations of coastal forest in large tsunami: Conditions of Japanese pine trees on coastal sand dunes in tsunami caused by Great East Japan Earthquake. *Journal of Japan Society of Civil Engineers, Ser. B1 (Hydraulic Engineering)*, 68(4):II_7–II_15, 2012.

[208] N. Tanaka, Y. Sasaki, and M. Mowjood. Effects of sand dune and vegetation in the coastal area of Sri Lanka at the Indian Ocean tsunami. In *Advances in Geosciences: Volume 6: Hydrological Science (HS)*, pages 149–159. World Scientific, 2007.

[209] N. Tanaka, Y. Sasaki, M. Mowjood, K. Jinadasa, and S. Homchuen. Coastal vegetation structures and their functions in tsunami protection: Experience of the recent Indian Ocean tsunami. *Landscape and Ecological Engineering*, 3(1):33–45, 2007.

[210] N. Tanaka, J. Yagisawa, and S. Yasuda. Breaking pattern and critical breaking condition of Japanese pine trees on coastal sand dunes in huge tsunami caused by Great East Japan earthquake. *Natural Hazards*, 65(1):423–442, 2013.

[211] N. Tanaka, S. Yasuda, K. Iimura, and J. Yagisawa. Combined effects of coastal forest and sea embankment on reducing the washout region of houses in the Great East Japan tsunami. *Journal of Hydro-environment Research*, 8:270–280, 2014.

[212] N. Tanaka, H. Sato, Y. Igarashi, Y. Kimiwada, and H. Torita. Effective tree distribution and stand structures in a forest for tsunami mitigation considering the different tree-breaking patterns of tree species. *Journal of Environmental Management*, 223:925–935, 2018.

[213] D. Tang, C. Yang, and D. N. Ku. A 3-D thin-wall model with fluid–structure interactions for blood flow in carotid arteries with symmetric and asymmetric stenoses. *Computers & structures*, 72(1-3):357–377, 1999.

[214] L. Tang, V. V. Titov, E. N. Bernard, Y. Wei, C. D. Chamberlin, J. C. Newman, H. O. Mofjeld, D. Arcas, M. C. Eble, C. Moore, B. Uslu, C. Pells, M. Spillane, L. Wright, and E. Gica. Direct energy estimation of the 2011 Japan tsunami using deep-ocean pressure measurements. *Journal of Geophysical Research: Oceans*, 117(C8), 2012.

[215] F. Tessicini, L. Temmerman, and M. A. Leschziner. Approximate near-wall treatments based on zonal and hybrid RANS–LES methods for LES at high Reynolds numbers. *International Journal of Heat and Fluid Flow*, 27 (5):789–799, 2006.

[216] T. E. Tezduyar. Interface-tracking, interface-capturing and enhanced solution techniques. *Mecánica Computacional*, pages 116–135, 2002.

[217] N. B. Thuy, N. Tanaka, and K. Tanimoto. Tsunami mitigation by coastal vegetation considering the effect of tree breaking. *Journal of Coastal Conservation*, 16(1):111–121, 2012.

[218] V. V. Titov and F. Gonzalez. Implementation and testing of the Method Of Splitting Tsunami (MOST) model. NOAA Technical Memorandum ERL PMEL-112 1927, NOAA, Seattle, WA,USA. Technical report, 1997.

[219] V. V. Titov and C. E. Synolakis. Extreme inundation flows during the Hokkaido-Nansei-Oki tsunami. *Geophysical Research Letters*, 24(11): 1315–1318, 1997.

[220] S. Tonkin, H. Yeh, F. Kato, and S. Sato. Tsunami scour around a cylinder. *Journal of Fluid Mechanics*, 496:165–192, 2003.

[221] H. Torita, K. Masaka, N. Tanaka, K. Iwasaki, S. Hasui, M. Hayamizu, and Y. Nakata. Assessment of the effect of thinning on the resistance of Pinus Thunbergii Parlat. trees in mature coastal forests to tsunami fluid forces. *Journal of Environmental Management*, 284:111969, 2021.

[222] H. Torita, Y. Igarashi, and N. Tanaka. Effective management of Japanese black pine (Pinus thunbergii Parlat.) coastal forests considering tsunami mitigation. *Journal of Environmental Management*, 311:114754, 2022.

[223] G. Tryggvason, B. Bunner, A. Esmaeeli, D. Juric, N. Al-Rawahi, W. Tauber, J. Han, S. Nas, and Y. J. Jan. A front-tracking method for the computations of multiphase flow. *Journal of Computational Physics*, 169(2): 708–759, 2001.

[224] C. P. Tsai, Y. C. Chen, S. T. Octaviani, and C. Lin. Simulations of moving effect of coastal vegetation on tsunami damping. *Natural Hazards and Earth System Sciences*, 17:693–702, 2017.

[225] S. Turek. A comparative study of time-stepping techniques for the incompressible Navier-Stokes equations: From fully implicit non-linear schemes to semi-implicit projection methods. *International Journal for Numerical Methods in Fluids*, 22(10):987–1011, 1996.

[226] S. Turek. *Efficient Solvers for Incompressible Flow Problems: An Algorithmic and Computational Approache*, volume 6. Springer Berlin, Heidelberg: Springer Science & Business Media, 1999.

[227] US Army Corps of Engineers USACE. Interim survey report, Morgan City, Louisiana and Vicinity. Technical Report 63, US Army Engineer District, New Orleans, LA, 1963.

[228] S. K. Venayagamoorthy and O. B. Fringer. Nonhydrostatic and nonlinear contributions to the energy flux budget in nonlinear internal waves. *Geophysical Research Letters*, 32(15), 2005.

[229] S. K. Venayagamoorthy and O. B. Fringer. Numerical simulations of the interaction of internal waves with a shelf break. *Physics of Fluids*, 18(7):076603, 2006.

[230] A. J. Venturato, D. W. Denbo, K. T. McHugh, J. R. Osborne, P. Sorvik, and C. Moore. NOAA tsunami forecasting system: Using numerical modeling tools to assist in tsunami warning guidance. In *23rd Conference on Interactive Information Processing Systems (IIPS) for Meteorology, Oceanography, and Hydrology*, 2007.

[231] A. W. Vreman. The filtering analog of the variational multiscale method in large-eddy simulation. *Physics of Fluids*, 15(8):L61–L64, 2003.

[232] M. Vázquez, G. Houzeaux, S. Koric, A. Artigues, J. Aguado-Sierra, R. Arís, D. Mira, H. Calmet, F. Cucchietti, H. Owen, A. Taha, E. D. Burness, J. M. Cela, and M. Valero. Alya: Multiphysics engineering simulation toward exascale. *Journal of Computational Science*, 14:15–27, 2016.

[233] X. Wang. User manual for COMCOT version 1.7. Technical report, 2009.

[234] M. Watanabe, T. Arikawa, N. Kihara, C. Tsurudome, K. Hosaka, K. Kimura, T. Hashimoto, F. Ishihara, T. Shikata, T. Morikawa, D. Makino, M. Asai, Y. Chida, Y. Ohnishi, S. Marras, A. Mukherjee, J. C. Cajas, G. Houzeaux, B. Di Paolo, J. L. Lara, G. Barajas, I. J. Losada, M. Hasebe, Y. Shigihara, T. Asai, T. Ikeya, S. Inoue, H. Matsutomi, Y. Nakano, Y. Okuda, S. Okuno, T. Ooie, G. Shoji, and T. Tateno. Validation of tsunami numerical simulation models for an idealized coastal industrial site. *Coastal Engineering Journal*, 64(2):302–343, 2022.

[235] Z. Wei, R. A. Dalrympl, A. Hérault, G. Bilotta, E. Rustico, and H. Yeh. SPH modeling of dynamic impact of tsunami bore on bridge pier. *Coastal Engineering*, 104:26–42, 2015.

[236] I. A. Williams and D. R. Fuhrman. Numerical simulation of tsunami-scale wave boundary layers. *Coastal Engineering*, 110:17–31, 2016.

[237] R. A. Wooding, E. F. Bradley, and J. K. Marshall. Drag due to regular arrays of roughness elements of varying geometry. *Boundary-Layer Meteorology*, 5(3):285–308, 1973.

[238] T. R. Wu and P. L. F. Liu. A large eddy simulation model for tsunami and runup generated by landslides. In *Advanced Numerical Models for Simulating Tsunami Waves and Runup*, pages 101–162. World Scientific, 2008.

[239] Y. Yamazaki, Z. Kowalik, and K. F. Cheung. Depth-integrated, non-hydrostatic model for wave breaking and run-up. *International Journal for Numerical Methods in Fluids*, 61:473–497, 2009.

[240] W. Yang, Z. Wen, F. Li, and Q. Li. Study on tsunami force mitigation of the rear house protected by the front house. *Ocean Engineering*, 159:268–279, 2018.

[241] Y. Yang, J. L. Irish, and R. Weiss. Impact of patchy vegetation on tsunami dynamics. *Journal of Waterway, Port, Coastal, and Ocean Engineering*, 143(4):04017005, 2017.

[242] Y. Zhang, F. Ye, E. V. Stanev, and S. Grashorn. Seamless cross-scale modeling with SCHISM, Ocean Model. *Ocean Modeling*, 102:64–81, 2016.

[243] Y. J. Zhang and A. M. Baptista. An efficient and robust tsunami model on unstructured grids. Part I: Inundation benchmarks. *Pure and Applied Geophysics*, 165:2229–2248, 2008.